**Investigation of Kinetic Physics of Magnetic Reconnection under a Finite Guide Field**

by

Xiang Lu

A dissertation submitted to the Graduate Faculty of
Auburn University
in partial fulfillment of the
requirements for the Degree of
Doctor of Philosophy

Auburn, Alabama
December 12, 2011

Keywords: Plasmas, Magnetic reconnection, Particle simulation



Approved by

Yu Lin, Chair, Professor of Physics
Stephen Knowlton, Professor of Physics
Edward Thomas, Jr., Professor of Physics

Abstract

Magnetic reconnection, the process by which the magnetic energy is converted into heat and flow energy, is believed to be a very important process in space and laboratory plasmas. Among various reconnection models, the Petschek model suggests a promising explanation for the fast time scale phenomena caused by the reconnection. For the antiparallel (zero guide field) cases, the Petschek model contains a small diffusion region and four standing slow shocks that bound the outflow region. In contrast to the pure antiparallel case, theoretical and simulation studies show that in general cases with a finite field, the Petschek model is modified with complicated wave structures. Such models, however, only correspond to the two-dimensional (2D) magnetic reconnection with a long, extended X-line. Two remaining issues in the Petschek model are still poorly understood. One is the onset mechanism for the reconnection, and the other is the wave properties in the outflow region of general three-dimensional (3D) reconnection. Tearing mode instabilities are thought to play a fundamental role to trigger the reconnection. In this thesis, we extend the recently-developed gyrokinetic electron and fully kinetic ion (GeFi) simulation model to nonuniform plasmas, and use it to study tearing mode instabilities under a finite guide field. By removing the rapid gyro-motions of electrons in the calculation, the main advantage of the current GeFi model is that the realistic mass ratio between electrons and ions is allowed to be employed in the simulation code. Through an eigenmode analysis, the improved GeFi model is benchmarked against the linear theory of the tearing instability. Furthermore, our simulation results show that the ion kinetics play an important role in the linear growth rate of the tearing mode instability as well as in the nonlinear saturation of tearing modes. For the cases with multiple tearing modes, the

interactions between them lead to the coalescence of neighboring magnetic islands, and form larger saturated magnetic islands, which has been suggested as a necessary condition to trigger a fast reconnection. In order to explore the properties of low frequency waves generated by the reconnection under a finite guide field, a 3D hybrid simulation is carried out for the large-scale structure of the reconnection layer. For the case with an infinitely long X-line, quasi-steady rotational discontinuities are formed behind a leading plasma bugle that propagates away from the reconnection site. Field-aligned structures are also observed in the transition region between the steady layer and the leading bulge. For the cases with a limited extent of X-line with length $< 30d_i$, the perturbations caused by the reconnection propagate along the magnetic field line, and the wavefront of propagation has the properties of kinetic Alfvén wave. There are no evident discontinuities that form to bound the outflow region. Due to the propagation of the waves, a layer of accelerated plasmas is found beyond the extent of the X-line. The simulation indicates that the wave structures in the reconnection are greatly modified from that in the 2D Petschek reconnection model when the X-line has a finite length.

Table of Contents

List of Figures

List of Tables

# Chapter 1

## An Overview of Magnetic Reconnection

Magnetic reconnection is a process that changes the topology of magnetic field lines. It is believed to take place between two plasma regions with antiparallel magnetic field components. During magnetic reconnection, sheared magnetic field lines will be effectively annihilated through magnetic diffusion, and then magnetic energy is transferred into plasma heat and kinetic energy. Magnetic reconnection provides the free energy for phenomena such as solar flares, magnetosphere substorms, the tokamak sawtooth collapse, and the ion heating in reversed-field pinch [*Yamada et al.*, 2010]. Fig.1.1 is a schematic representation of magnetic reconnection. antiparallel magnetic field lines break at the diffusion region and form an X-point at the center. Two magnetic islands are generated and bounded by the separatrix. The inflow plasmas are accelerated and flow out from the diffusion region.

In a plasma characterized by the ideal MHD Ohm's law $\mathbf{E} + \mathbf{V} \times \mathbf{B} = 0$, where $\mathbf{V}$ is the velocity, $\mathbf{E}$ and $\mathbf{B}$ are the vector electric and magnetic fields, magnetic field lines follow the plasma motion as if they were "frozen in" the flow. This property conserves the field line topology, and thus reconnection can never happen. Varieties of mechanisms can lead to a violation the ideal Ohm's law. Resistivity is the most commonly cited dissipation that causes reconnection. Models based on resistivity include the Sweet-Parker model [*Parker*, 1957; *Sweet*, 1958], in which the extent of the dissipation layer in the outflow direction is much bigger than the width of the layer, and the Petschek model [*Petschek*, 1964], in which the dissipation layer is highly localized in both the inflow and outflow direction. Theoretical calculations show the magnetic reconnection rate, a direct measure of the speed of the mixing process, of

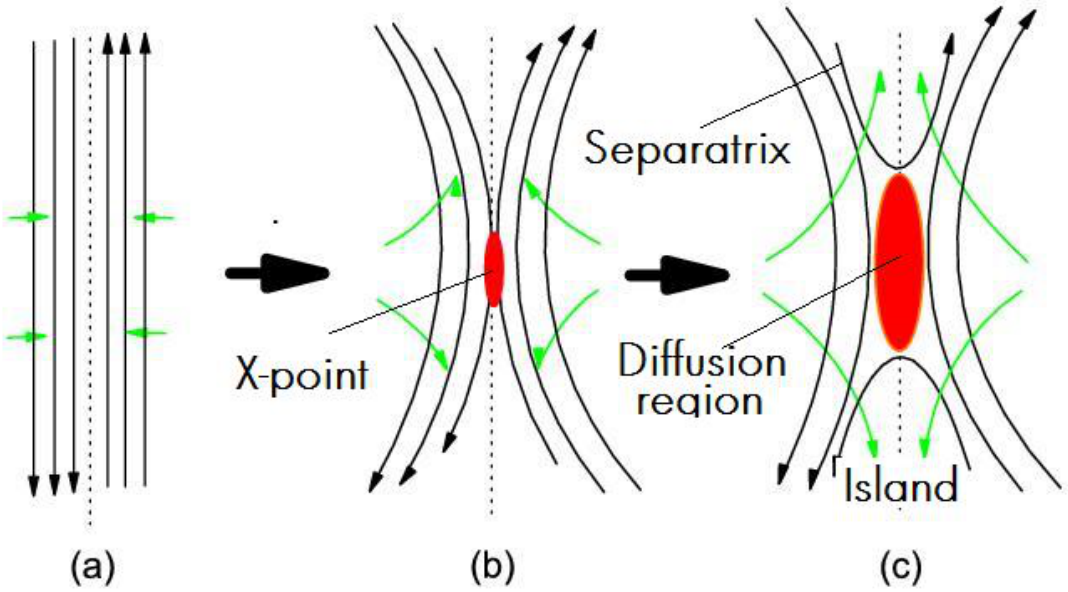


Figure 1.1: A schematic representation of reconnection is shown. Magnetic field lines become reconnected in the diffusion region and form a X-point. Two islands are generated and bounded by the separatrix. Picture is cited from http://www.aldebaran.cz/astrofyzika/plazma/reconnection.html.

the Sweet-Parker model is too slow to explain the energy release processes that are thought to be caused by the magnetic reconnection. The Petschek model contains a set of four MHD discontinuities which in the compressible flow may be identified as slow mode shocks across which the plasma is accelerated into the outgoing flow regions. Instead of dissipating magnetic energy, the diffusion region in the Petschek model mainly plays a role as the perturbation source of slow modes. The Petschek-type reconnection is the first fast reconnection model, in which the reconnection rate is fast enough to explain observed dynamic times of phenomena caused by the reconnection.

To validate the Petschek model, two questions should be answered. One is what is the physics in the dissipation region, i.e., the triggering mechanism of reconnection; the other is what is the structure of outflow region referred as the reconnection layer. The tearing mode instability is one candidate to trigger the magnetic reconnection in

both the resistive MHD regime [*Furth et al.*, 1963, 1973] and the collisionless kinetic regime [*Drake & Lee*, 1977a, 1977b]. On the other hand, theoretical and numerical studies [*Lin and Lee*, 1994a, 1994b] showed that the structure of the reconnection layer is not as simple as predicted by *Petschek* but varies with different parameters.

This thesis is composed of two parts, which addresses the kinetic physics of magnetic reconnection on two different spatial and temporal scales, from the diffusion region to the large-scale reconnection layer. First, we are going to improve the exiting gyrokinetic electron and fully kinetic ion simulation (GeFi) model [*Lin et al.*, 2005a; *Wang et al.*, 2010], and use it to study the tearing mode instability. Second, a three-dimensional (3D) hybrid model [*Lin et al.*, 2005b; *Lin et al.*, 2010] will be used to investigate the electromagnetic waves generated by the reconnection. In the following, we first give a brief review of the steady state reconnection models, the tearing mode instability, and the structure of the reconnection layer, is given. In the end, the results of this thesis are summarized.

## 1.1 Steady State Reconnection Models

### 1.1.1 Sweet-Parker Model

The Sweet-Parker model is sketched in Fig.1.2. Sweet [1957] and Parker [1958] determined the speed $v_i$ with which field lines are carried into a steady diffusion region of length $2L$ and width $2l$. First of all, for a steady state, the convective inflow of the magnetic field is balanced by the outward diffusion, so that

$$v_i = \frac{\eta}{l}, \tag{1.1}$$

where $\eta$ is the magnetic diffusivity.

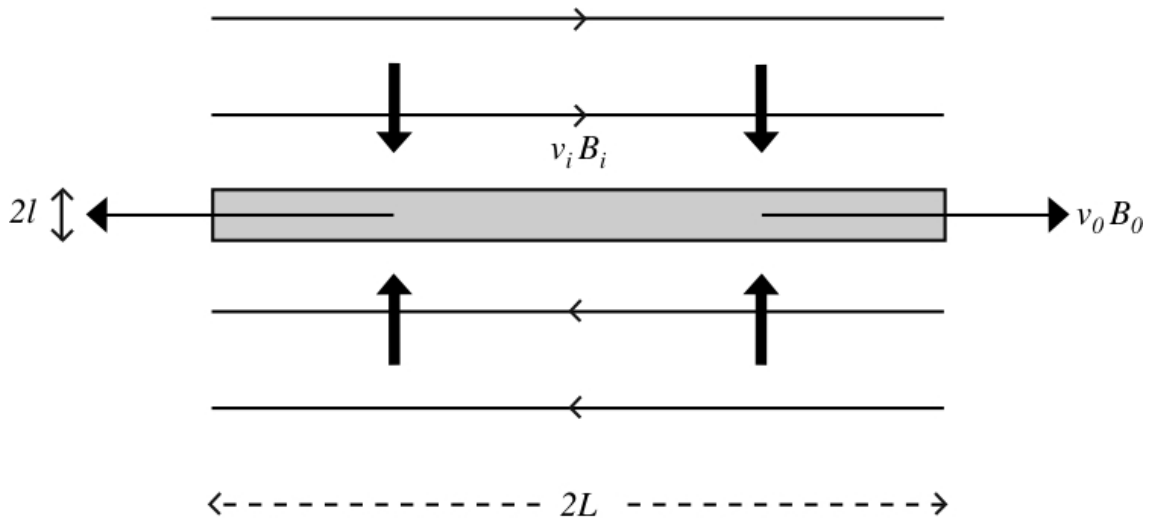


Figure 1.2: Sweet-Parker model of reconnection is shown with a steady diffusion region of length $2L$ and width $2l$. $v_i$ is the inflow speed, and $v_o$ the outflow speed. Picture is cited from http://www.scholarpedia.org/article/reconnection.

Second, the rate $4\rho L v_i$ at which mass is entering the sheet must equal the rate $4\rho l v_o$ at which it is leaving, so that, if the density is uniform,

$$L v_i = l v_o, \tag{1.2}$$

where $v_o$ is the outflow speed. The width $l$ may now be eliminated from Eqs.(1.1) and (1.2) to give the inflow speed as $v_i^2 = \eta v_o / L$. If the plasma is accelerated along the sheet by a Lorentz $\vec{j} \times \vec{B}$ force, the outflow speed $v_o$ is the Alfvén speed at the inflow, namely, $v_o = v_{Ai} = B_i / \sqrt{4\pi\rho}$ and the reconnection rate is

$$v_i = \frac{v_{Ai}}{{R_{mi}}^{1/2}} \tag{1.3}$$

where the magnetic Reynolds number $R_{mi} = L v_{Ai}/\eta$, or in dimensionless form $M_i = R_{mi}^{-1/2}$, with $M_i = v_i / v_{Ai}$ being the inflow Alfvén Mach number.

In the Sweet-Parker mechanism, we identify the sheet length $L$ with the global length and $R_{mi}$ therefore with the global magnetic Reynolds number. Since in practice

$R_{mi} \gg 1$, the reconnection rate is very small: for instance, in the solar corona where $R_{mi}$ lies between $10^6$ and $10^{12}$, the fields reconnect at between $10^{-3}$ and $10^{-6}$ of the Alfvén speed. Note the phenomena caused by the reconnection such as solar flares usually have the Alfvén time scale $\tau_A = 1/v_A$ where $v_A$ is the local Alfvén speed.

Important extra effects are the compressibility, which slows down the outflow when $\rho_o > \rho_i$, and a pressure gradient along the diffusion region, which can also slow the outflow when the outflow pressure $p_o$ is large enough.

### 1.1.2 Petschek Model

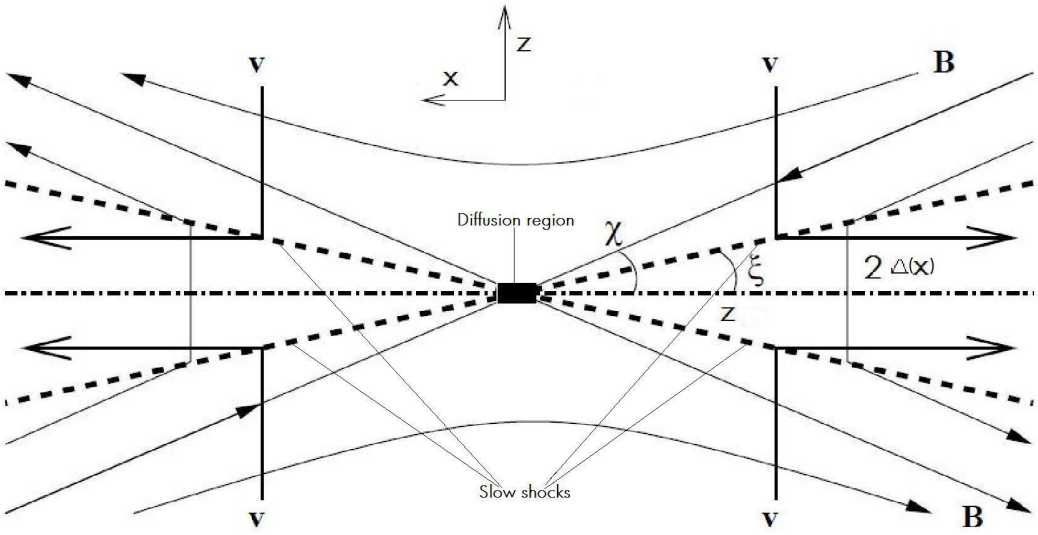


Figure 1.3: Petschek model of reconnection is shown with a small diffusion region. The outflow region is bounded by two pair slow shocks. Picture is cited from http://www.scholarpedia.org/article/reconnection.

The configuration of the Petschek model is sketched in Fig.1.3. Two waves (slow mode shocks) stand in the flow on either side of the outflow region, where the direction of **B** reverses, marking the boundaries of the plasma outflow regions. A small diffusion region still exists, but has much smaller length compared with that in the Sweet-Parker model. The upstream plasma flows into the shock where the

magnetic energy is converted into the energy of outflowing plasma jets; the outward wave propagation velocity in the $\pm z$ direction balances the plasma inflow velocity in a steady state. The reconnection rate should be equal to the shock propagation velocity which is independent of the plasma resistivity and can be much larger than the Sweet-Parker model. At the same time, the magnetic diffusion is still the dominant mechanism of energy conversion in the diffusion region near the center $z = 0$ of the reconnection site. The match of reconnection rate between the diffusion region and the shock region leads to a very narrow diffusion length.

In the switch-off limit of the slow shock, the inflow speed can be estimated as

$$v_{zi} = v_{phi} = \frac{|B_{zi}|}{\sqrt{4\pi\rho_i}}, \tag{1.4}$$

where $v_{phi}$ is the phase speed of slow shocks, $B_{zi}$ is the z component of magnetic fields in the inflow region and is approximated as the normal field of the shocks. The subscripts "i" and "o" stand for the inflow (upstream) and the outflow (downstream). Note that the switch-off limit corresponds to the strongest slow shock, across which the tangential magnetic fields change to 0. To simplify the calculation, we assume that the plasma is incompressible, i.e., $\rho = constant$. The MHD mass momentum of conservation laws give,

$$v_{zi}x = v_{xo}\triangle(x), \tag{1.5}$$

$$\frac{d}{dx}(\rho v_{xo}^2 \triangle(x)) = \frac{B_{zi}B_i}{4\pi}, \tag{1.6}$$

where $B_i$ is the magnitude of magnetic field in the inflow region. Insert Eq (1.5) into Eq (1.6), and do a little algebra,

$$\frac{d}{dx}(\frac{x^2}{\triangle(x)}) = \frac{1}{M_{Ai}^2}\frac{B_{zi}}{B_i} = \frac{B_{zi}}{B_i}, \tag{1.7}$$

where $M_{Ai}$ the upstream Mach number and $M_{Ai} = 1$ for the switch-off limit of slow shocks. After integrating Eq.1.7, we have

$$\frac{x}{\triangle(x)} = \frac{B_{zi}}{B_i}. \tag{1.8}$$

Since the downstream velocity can be expressed as

$$v_{xo} = v_{Ai}, \tag{1.9}$$

we have $v_{zi} \approx \frac{B_{zi}}{B_i} v_{Ai}$. It has indicated $\frac{B_{zi}}{B_i} \sim 0.1$ by simulations. Therefore the reconnection rate is $\frac{v_{zi}}{v_{Ai}} \approx 0.1$, much faster than in the Sweet-Parker model.

There has been some controversy whether the Petschek model describes the correct physics. It gives a description of reconnection that is only very weakly dependent on the properties of the reconnection region and thus on the resistivity. Numerical simulations [*Biskamp*, 1986], however, showed that with a spatially constant resistivity the Petschek-type reconnection does not occur. In order to have the Petschek-type reconnection, the resistivity should be enhanced in the diffusion region [*Lottermoser et al.*, 1997]. For collisionless plasmas as in most of the space environments, the determination of the anomalous $\eta$ in the diffusion region is a hot topic in reconnection research. Current driven instabilities such as the modified two-stream instability [*Wu et al.*, 1983] the low-hybrid drift instability [*Daughton*, 2003; *Ricci et al.*, 2005] may play a key role in the formation of anomalous resistivity.

## 1.2 Tearing Mode Instability

### 1.2.1 Resistive Tearing Mode

In the resistive (i.e., collisional) plasma, a current sheet tends to diffuse at a slow rate with a time-scale of $\tau_d = l^2/\eta$, where $2l$ is the width of the current sheet

and $\eta = \mu\sigma^{-1}$ is the magnetic diffusivity. During the process of magnetic diffusion, magnetic energy is converted into heat at the same slow rate by the Ohm's law. As pointed out in the first section, however, the magnitude of $\tau_d$ is often far too large to explain the time scale of dynamical physical processes.

Furth [1963] first found that the diffusion can drive an instability with a time scale much faster than the diffusion time, referred as the tearing mode instability. Considering the perturbation as the one in Fig.1.4, the tension force of reconnected field lines tends to pull new loops of field up and down away from the X-point, while the magnetic pressure gradient tends to push plasma in from the sides towards the X-point. The field lines at the sides are curved and so possess a restoring magnetic tension force.

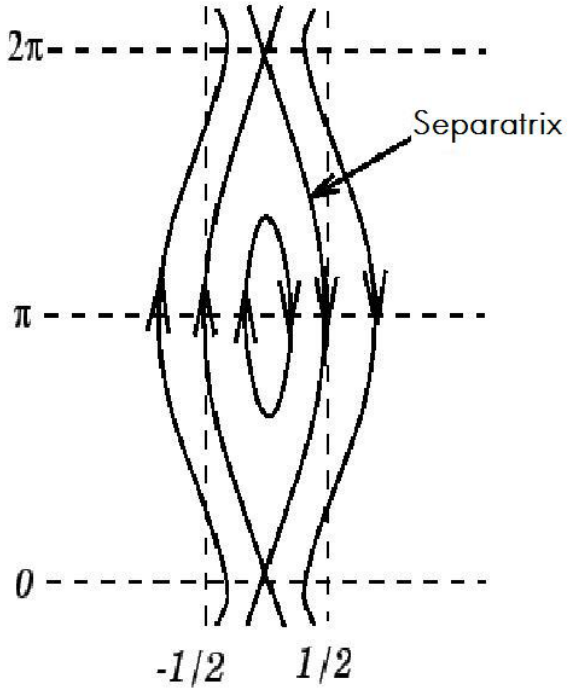


Figure 1.4: Magnetic field-lines in the vicinity of a magnetic island generated by tearing modes is shown. A magnetic island is bounded by separatrix. Picture is cited from http://farside.ph.utexas.edu/teaching/plasma/lectures1.

Detailed theoretical studies showed [*Furth*, 1963; *Wesson*, 1966] that the tearing mode occurs with a wavelength greater than the width of the sheet ($kl < 1$). The smallest allowable wavelength grows in a time $\tau_d^{3/5}\tau_A^{2/5}$, whereas the longest wavelength has the fastest growth rate $\gamma$,

$$\gamma = \frac{1}{\sqrt{\tau_d \tau_A}}. \tag{1.10}$$

The presence of a guiding field does not affect the existence of tearing modes. At any particular location, the maximum growth of tearing modes occurs where the wave vector $\mathbf{k}$ is perpendicular to the equilibrium field $\mathbf{B_0}$, that is,

$$\mathbf{k} \cdot \mathbf{B_0} = \mathbf{0}. \tag{1.11}$$

With the addition of a uniform guiding field, this condition can be satisfied at the center of the current sheet.

One may have noticed that the typical time scale of tearing modes $\tau_t = \sqrt{\tau_d \tau_A}$ is in general much larger than the diffusion time $\tau_d$, but much smaller than the Alfvén time $\tau_A$, or the typical fast reconnection time scale, i.e., $\tau_A << \tau_t << \tau_d$. So the tearing mode is still not fast enough to explain the phenomena that are thought to be caused by the reconnection.

The geospace environment magnetic (GEM) reconnection challenge was to aim to discover the physics of fast reconnection [*Birn et al.*, 2001]. They found that nonlinear evolution of a large magnetic island in a current sheet can lead to a fast reconnection with the rate of the order $\tau_A^{-1}$. The Hall terms in the generalized or kinetic Ohm's law were believed to be important. For high $\beta$ plasmas it was clarified that the whistler wave plays a key role in the fast reconnection physics [*Pritchett*, 2001; *Birn et al.*, 2001]. At lower $\beta$ plasmas in the presence of a guide field, it was

shown that the kinetic Alfvén wave drives the fast reconnection [*Ricci*, 2008; *Rogers*, 2001].

However, the GEM reconnection challenge avoided the issue on the triggering of the fast reconnection, or more precisely on how a magnetic island forms initially with the size comparable to the system's spatial scale. One may argue that the role of tearing modes may present a mechanism that form a large magnetic island. Unfortunately, the tearing mode often saturates at a small level, and the width of the magnetic island is not large enough to trigger the fast reconnection [*Rutherford*, 1973; *Daughton and Karimabadi*, 2005]. However, it is also found that a chain of magnetic islands created by multiple tearing modes can lead to an instability, namely the coalescence [*Finn and Kaw*, 1977; *Pritchett*, 1992]. During the coalescence, neighboring islands attract each other due to the parallel currents inside islands and then form larger magnetic islands [*Karimabadi et al.*, 2005a; *Pritchett*, 2005].

### 1.2.2 Collisionless Tearing Modes

Plasmas in the cosmic and tokamak environments are generally collisionless. So the resistive MHD approach to the tearing mode may be invalid. Drake and Lee [1977a] applied a kinetic theory to the tearing mode instability for a current sheet with a strong guide magnetic field (perpendicular to the antiparallel components of the field). They found a perturbed current produced by the induced electric field around the central layer can drive the tearing mode instability, and thereby cause the magnetic reconnection.

To estimate the growth rate of the collisionless tearing mode, the simple slab current configuration as in Fig.1.5 was studied. First, consider a perturbation with the wave number $k_x$, and the growth rate $\gamma$. The perturbed magnetic field can be

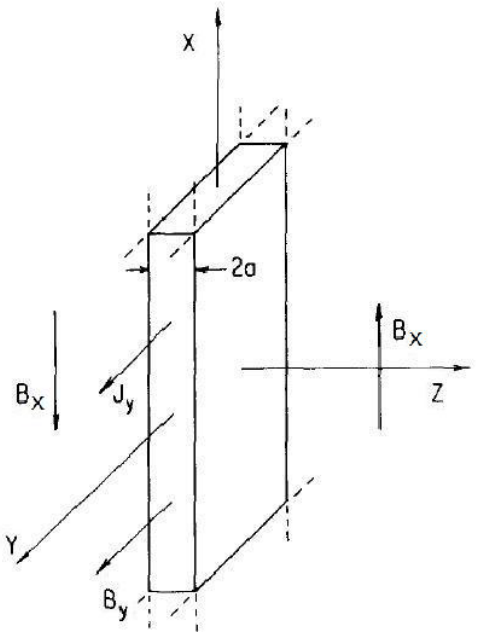


Figure 1.5: A simple slab current sheet is shown with antiparallel magnetic components $B_x$ and a strong guide field $B_y$. Picture is cited from Drake and Lee [1977a].

expressed with the vector potential $A_y$ as

$$B_z = ik_x A_y, \tag{1.12}$$

$$B_x = \frac{\partial A_y}{\partial z}. \tag{1.13}$$

Then the induced electric field can be written as

$$E_y = -\gamma A_y. \tag{1.14}$$

It has a component parallel to the local magnetic field $E_{||} = E_y cos(\theta)$, where $sin(\theta) = B_{0x}/B_0 = k_{||}/k_x$(see Fig.1.6). The parallel electric field will generate a large parallel current at $z = 0$ where

$$\mathbf{k} \cdot \mathbf{B_0} = \mathbf{0}. \tag{1.15}$$

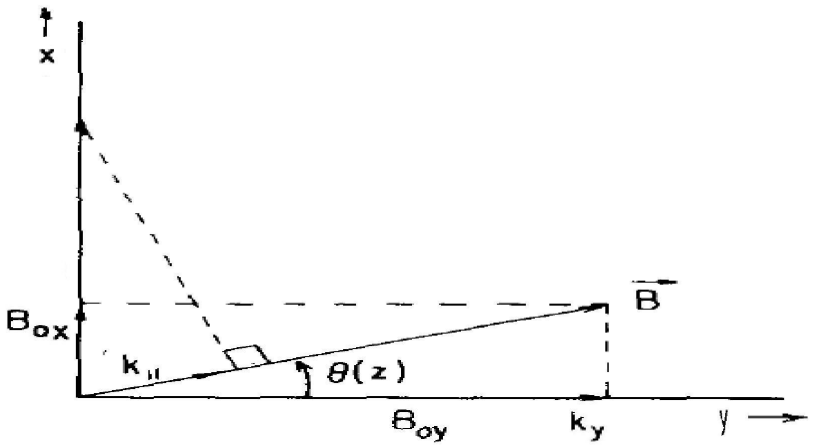


Figure 1.6: Directions of **k** and **B** near the center of the current sheet is shown. Picture is cited from Drake and Lee [1977a].

Note that the induced current is restricted inside a narrow region of $|z| < \Delta$. After integrating the z component of the Ampere's equation, we have

$$[B_x]_{-\Delta}^{\Delta} = \frac{4\pi}{c}\Delta j_y, \tag{1.16}$$

which can be rewritten as

$$[\frac{\partial A_y}{\partial z}]_{-\Delta}^{\Delta} = -\frac{4\pi}{c}\Delta j_y. \tag{1.17}$$

So $\frac{\partial A_y}{\partial z}$ is not continuous across the induced current layer. Outside of the current layer, $E_{||} = 0$, and the ideal MHD equations was used. A simple expression is given as

$$\Delta' = \frac{1}{A_y}[\frac{\partial A_y}{\partial x}]_{-\Delta}^{\Delta}. \tag{1.18}$$

Then combining the above two equations, one has

$$\Delta' A_y = -\frac{4\pi}{c}\Delta j_y. \tag{1.19}$$

The induced current is

$$\mathrm{J}_y = -\frac{n_0 e^2 A_y}{me}. \tag{1.20}$$

According to the cherenkov resonances condition, the growth rate should be

$$\gamma = k_{||} \cdot v_{the} = \frac{k_x v_{the} \Delta}{l_s} \tag{1.21}$$

where $l_s$ is the magnetic field shear length, and $v_{the}$ is the electron thermal velocity. A little algebra gives the growth rate as

$$\gamma = \frac{\Delta^{'} k_x v_{the}}{l_s d_e^2}, \tag{1.22}$$

where $d_e^{-1} = c/\omega_{pe}$ is the electron skin depth.

## 1.3 The Structure of Reconnection Layer

### 1.3.1 Summary of MHD Waves and Discontinuities

Startting from the ideal MHD equations, one can easily deduce the dispersion relationship of the linear MHD waves, which are summarized below [*Landau and Lifshitz.*, 1960].

(a) Fast mode:

$C_F = \frac{1}{2}\sqrt{[(C_s^2 + C_A^2) + \sqrt{(C_s^2 + C_A^2) - 4C_s^2 C_I^2}]}$;

(b) Intermediate mode (Alfvén wave):

$C_I = C_A cos(\theta)$;

(c) Slow mode:

$C_S = \frac{1}{2}\sqrt{[(C_s^2 + C_A^2) - \sqrt{(C_s^2 + C_A^2) - 4C_s^2 C_I^2}]}$;

where $C$ denotes the wave phase speed, and the subscript F denotes the fast mode, I the intermediate mode, and S the slow mode. $C_s = \sqrt{\frac{\Gamma P}{\rho}}$ is the sound speed and $\Gamma$ is the specific heat ratio. $C_A = \frac{B}{\sqrt{4\pi\rho}}$ is the Alfvén speed and $\theta$ is the wave propagation

angle with respect to the background magnetic field. Fig.1.7 shows the dispersion-relation of MHD waves. Phase velocity is the propagation speed of a single-mode wave while group velocity is the envelope speed of the waves, i.e., the propagation speed of a group of single-mode waves. From Fig.1.7, one can tell that the fast mode is isotropic, propagating around all angles with respect to the background magnetic field, while the propagations of the intermediate mode and the slow mode concentrate in the direction parallel to the background magnetic field.

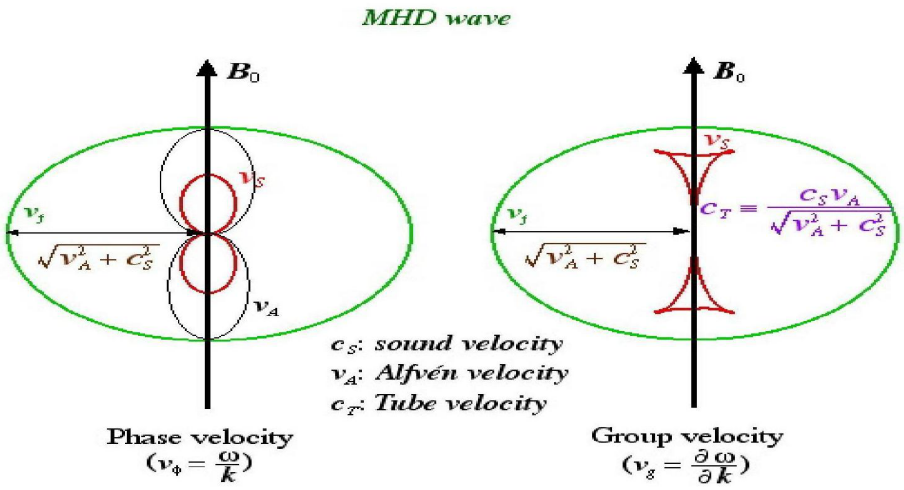


Figure 1.7: Phase velocity and group velocity of MHD waves. Picture is cited from http://solar.physics.montana.edu/magara/Research/Topics/MHDwaves.

An MHD discontinuity can be considered as a thin transition region between two uniform stationary plasma regions across which the magnetic field, plasma density, pressure and flow velocity may have a significant jump. The jump conditions are obtained from the conservation laws of the MHD formulations referred to as the Rankine-Hugoniot (RH) jump conditions. It is well known that four types of MHD discontinuities exist: contact discontinuity, tangential discontinuity, rotational discontinuity and MHD shocks. The jump conditions of different discontinuities are summarized below [*Hans and Poedts*, 2004].

(1) Contact discontinuity:

$v_n = 0$, $B_n \neq 0$, $[B_t] = 0$, $[v_t] = 0$, $[\rho] = 0$, $[P] = 0$.

A contact discontinuity separates two regions with different plasma densities but the pressure, magnetic field, and plasma velocity are continuous. The component of magnetic field normal to the discontinuity front, $B_n$, is not equal to zero. The contact discontinuity is a non-propagating structure.

(2) Tangential discontinuity:

$v_n = 0$, $B_n = 0$, $[B_t] \neq 0$, $[v_t] \neq 0$, $[\rho] \neq 0$, $[P + \frac{B^2}{8\pi}] = 0$.

A tangential discontinuity links two regions with different tangential magnetic fields. The component of magnetic fields normal to the discontinuity front $B_n$ is equal to zero. No flow normal to the discontinuity is allowed. Across the tangential discontinuity the total pressure is balanced , while the plasma densities and tangential plasma flow velocities on the two sides of the discontinuity are different.

(3) Rotational discontinuity:

$v_n = \frac{B_n}{\sqrt{4\pi\rho}}$, $[v_t] = \frac{[B_t]}{\sqrt{4\pi\rho}}$, $[\rho] = 0$, $[P] = 0$.

A rotational discontinuity links two regions with different tangential magnetic field and a finite normal magnetic field component, and the normal flow is allowed. The rotational discontinuity is associated with the propagating nonlinear Alfvén mode structure through which the normal component of the plasma flow velocity relative to the discontinuity is constant and equal to the normal Alfvén speed, which is $v_{An} = \frac{B_n}{\sqrt{4\pi\rho}}$. Across a rotational discontinuity, the plasma density, the pressure, the normal magnetic field and the normal plasma flow velocity remain unchanged.

MHD shocks can be further divided into three types: fast shocks, intermediate shocks, and slow shocks. They are formed by the steepening of MHD fast waves, intermediate waves, and slow waves, respectively. The jump conditions of MHD shocks can be described as the following [*Priest and Forbes*, 2006] :

(1) For a fast shock $v_{n1} > C_{F1}$ and $C_{I2} < V_{n2} < C_{F2}$, the tangential magnetic field does not change direction, and $[\rho] > 0, [P] > 0, [B_t] > 0, [v_n] < 0$. Across the fast shock, the plasma density, the pressure, the magnitude of the tangential magnetic field increase. The normal component of plasma flow velocity decreases.

(2) For an intermediate shock $v_{n1} > C_{I1}$ and $v_{n2} < C_{I2}$, the tangential magnetic field changes the direction by $180^0$, and $[\rho] > 0, [P] > 0, [B_t] \neq 0, [v_n] < 0$. Across an intermediate shock, the plasm density and the pressure increase. The normal component of the plasma flow velocity decreases. The magnitude of the tangential magnetic fields is changed.

(3) For a slow shock with $C_s < v_{n1} < C_{I1}$ and $v_{n2} < C_{s2}$, the tangential magnetic field does not change the direction, and $[\rho] > 0, [P] > 0, [B_t] < 0, [v_n] < 0$. Across a slow shock, the plasma density and pressure increase. The normal component of the plasma flow velocity and the magnitude of the tangential magnetic field decrease.

MHD theory, however, does not give the internal structure of discontinuities. With the particle kinetic effects in a collisionless plasma, the discontinuities discussed above have a finite width on the order of several ion radii [*Swift and Lee*, 1983; *Richter and Sholer*, 1989, 1991]. Moreover, MHD theory fails to explain the dissipation mechanism across MHD shocks in collisionless plasmas. Numerous numerical experiments have confirmed that the dissipation of MHD shocks in collisionless plasmas arise from the self consistent wave-particle interactions inside of shocks [*Sato*, 1979; *Ugai*, 1984; *Lee and Lee*, 1991].

### 1.3.2 Previous Research on the Structure of Reconnection Layer

Based on the ideal MHD formulation, the structure of the reconnection layer was studied by solving the one-dimensional (1D) Riemann problem [*Heyn et al.*, 1988; *Biernat et al.*, 1989; *Lin and Lee*, 1994a]. In this initial value problem, a nonzero normal component of the magnetic field is superposed on a 1D current sheet,

| | $B_y = 0$ | $B_y \neq 0$ |
|---|---|---|
| Symmetric | $SS + SS^{'}$ | $RD + SS + SS^{'} + RD^{'}$ |
| Asymmetric | $RD + SE + CD + SS^{'}$ | $RD + SE + CD + SS^{'} + RD^{'}$ |

Table 1.1: Structure of reconnection layer under various conditions [Lin and Lee, 1994a]. SS: slow shock, SE: slow expansion wave, RD: rotational discontinuity, CD: contact discontinuity, IS: intermediate shock, TIDS: time-dependent intermediate shock.

which breaks the equilibrium of the current sheet. The initial sheet then evolves to a layer with several MHD discontinuities, shocks. The temporal development of this layer is viewed as an approximation of the reconnection layer at increasing distances from the X-line. These studies indicate that five discontinuities and expansion waves may develop in a reconnection layer, including rotational discontinuities, intermediate shocks, slow shocks, slow expansion waves, and a contact discontinuity. The rotational discontinuities and intermediate shocks change the direction of the magnetic field, the slow shocks and slow expansion waves change the magnitude of magnetic field and plasma density, and the central contact discontinuity matches different plasma densities on the two sides. In addition, two fast expansion waves are also present in the solution of the Riemann problem, but they quickly propagate away from the reconnection layer. The results of the Riemann problem are summarized in Table.1.1.

The MHD simulations have been carried out for the resistive structure of reconnection layers. Using a 1D resistive MHD code, Lin et al. [1992], Lin and Lee [1994a], Ugai and Shimizu [1995] have simulated the Reimann problem for the evolution of an initial current system. It is found that the rotational discontinuities are replaced by time-dependent intermediate shocks. To deal with the multi-dimensional reconnection configuration, two-dimensional (2D) MHD simulations have been carried out to study the steady-state reconnection. The MHD discontinuities predicted from the 1D simulations are found to develop in the 2D reconnection layer [*Shi et al.*, 1990; *Sholer*, 1989; *Yan*, 1992]. Slow shocks in the Petschek-type symmetric reconnection

layer and intermediate shocks in the reconnection layer with asymmetric magnetic field and plasma density have been obtained in the cases with $B_y = 0$. In the cases with $B_y \neq 0$, rotational discontinuities are replaced by time-dependent intermediate shocks that have been found.

MHD models and simulations, however, do not account for the particle kinetic effects in collisionless plasmas. In an effort to include the ion kinetic effects, both 1D hybrid simulations and 2D hybrid simulations, in which ions are treated as discrete particles and electrons are treated as a massless fluid, of the reconnection layers have been performed. 1D hybrid simulations [*Lin and Lee*, 1995] indicate that the contact discontinuity disappears because of the mixing of ions along the field lines; the slow shock and slow expansion waves are modified. The kinetic structure of the reconnection layer have also been investigated by 2D large-scale hybrid simulations [*Lin and Swift*, 1996; *Lottermoser et al.*, 1998; *Kruassvarban and Omidi*, 1995]. These hybrid simulations have shown that the structures of MHD discontinuities and shocks are modified in collisionless plasmas..

Note that previous simulations of the reconnection layer are limited to the 1D or 2D geometry. In these cases, the normal direction to the fronts of low-frequency electromagnetic waves are mainly along the direction of the normal magnetic field, which is almost perpendicular to the current sheet. In the real space plasmas, however, magnetic reconnection is frequently observed to have a 3D structure, for which the length of the X-line has a short or finite extent. To further understand the physics of the reconnection, we will address the 3D effects of the reconnection layer in this thesis.

## 1.4 Numerical Models of Magnetic Reconnection

Numerical simulations have proven to be a powerful tool to understand the physics of magnetic reconnection. Simulation codes can be rougthly divided into

four categories: (1) MHD codes, (2) fully-kinetic particle codes, (3) hybrid codes that treat ions as particles and electrons as a massless fluid, and (4) gyrokinetic codes that treat charged particles as gyrokinetic particles.

In the MHD codes, MHD equations are solved numerically with finite difference or finite elements. Since MHD simulations do not contain the individual particle dynamics, they only describe the large-scale dynamics of plasmas. However, the MHD model may still give a correct description of physics on the large-scale bulk dynamics of collisionless plasmas. There are two reasons for that. First, in the presence of a magnetic field particles undergo gyro-motions around the local magnetic field, and thus the motions across field lines are prevented. Second, along the magnetic field direction numerous short-scale wave-particle interactions tend to impede the motion of charged particles. MHD simulations of the magnetic reconnection are mainly focused on the global structure of reconnection. It usually has a much larger spatial scale than $d_i$ or $\rho_i$, and much larger time scale than $1/\omega_{pi}$ or $1/\Omega_i$, where $d_i$ is the ion inertial length, $\rho_i$ is the ion gyroradius, $\omega_{pi}$ is the ion plasma frequency, and $\Omega_i$ is the ion gyrofrequency. To incorporate the local dynamics due to the separation between the electron and ion masses, the so-called Hall MHD codes and two fluid MHD codes have been developed. Nevertheless, kinetic effects are again missing in these models.

Full-particle simulations, in which electrons as well as ions are treated as fully kinetic particles, have been utilized for decades to investigate the kinetic behavior of reconnection [*Terasawa*, 1981; *Leboeuf et al.*, 1982; *Hoshino*, 1987; *Ding and Lee*, 1990; *Mandt et al.*, 1994; *Cai and Lee*, 1997; *Hesse and Winske*, 1998; *Shay and Drake*, 1998; *Shay et al.*, 2001, 2007; *Pritchett*, 2001; *Pritchet and Coroniti*, 2004; *Swisdak et al.*, 2005; *Daughton et al.*, 2006; *Karimabadi et al.*, 2007]. In these codes, the particle-in-cell (PIC) technique is often used in which the simulated "macroparticles" represent many plasma particles. Nevertheless due to large-scale separations both in

time (from electron plasma oscillation to reconnection time) and in space (from the Debye length to the system size), various approximations or compromises have to be used. Most of full-particle simulations have employed unrealistically low ion-to-electron mass ratio $m_i/m_e$, and also limited the domain to a few or ten's of $\rho_i$, and the simulation time much less than the global Alfvén time scale.

Hybrid simulation is another kinetic approach often used in reconnection studies, in which ions are treated as particles, but electrons are treated as a massless resistive fluid. In general, hybrid codes do not resolve the small spatial and time scales associated with the electron mass, and have been used to simulate large-scale structures of reconnection associated with the ion dynamics [*Lin and Swift*, 1996; *Nakamura and Scholer*, 2000; *Petschek*, 1964; *Lin and Lee*, 1994a; *Lin and Wang*, 2006]. Note that the triggering mechanism of collisionless reconnection, due to the electron kinetic effects, is not included in hybrid models.

An alternative particle model, called gyrokinetic model, has been broadly used in the fusion research. For the low frequency physics in strong magnetized plasmas such as a tokamak plasma, the gyromotion can be averaged out. The nonlinear gyrokinetic Vlasov-Maxwell equations have been derived by Fireman and Chen [1982] and first applied in gyrokinetic simulations by Lee [1983]. Since the fast gyromotion of charged particles have been removed, larger spatial and time steps are allowed in gyrokinetic simulations than in traditional particle simulations. In the presence of a guide field, particles are strongly magnetized during the magnetic reconnection. Therefore the gyrokinetic treatment can also be applied to the reconnection research. Tearing mode instabilities have been simulated using the gyrokinetic model. Wan et al. [2007] treated ions as gyrokinetic particles and electrons as drift kinetic particles, while both ions and electrons are gyrokinetic particles in Ricci et al.'s work [2004]. But the gyrokinetic and drift kinetic treatment of ions are not suitable to the reconnection physics since the whistler and lower-hybrid regime is beyond the model capability.

Recently an innovative fully nonlinear new particle simulation model has been developed, in which the electron dynamics is handled by the gyrokinetic (GK) equations and the ions are treated as fully kinetic (FK) particles. In the gyrokinetic electron and fully kinetic ion (GeFi) simulation, the rapid electron cyclotron motion is removed, while finite electron Larmor radii, wave-particle interactions, and off-diagonal components of the electron pressure tensor are retained, as well as the fully kinetic ion physics. This treatment results in a larger time step and allows the realistic mass ratio $m_i/m_e$ in the simulation of magnetic reconnection. The computation efficiency can be significantly improved as compared with that of the full-particle codes. The model is particularly suitable for plasma dynamics with wave frequencies $\Omega <$ electron gyrofrequency $\omega_e$, and for problems in which the wave modes range from Alfvén waves to lower-hybrid/whistler waves. The GeFi scheme has been benchmarked in the uniform plasma [*Lin et al.*, 2005] and important new results have been obtained for current sheet instabilities in the presence of a finite guide field [*Wang et al.*, 2008; *Yoon et al.*, 2008]. The original GeFi model, however, does not include the effects of nonuniformity of the background magnetic field and plasmas. In this thesis, we are going to improve the existing GeFi codes for a current sheet, and study the collisionless tearing mode instability with the realistic mass ratio $m_e/m_i = 1/1836$.

## 1.5 Motivations and Objectives of the Thesis

As described above, full particle simulations includes the kinetic electron dynamics but cannot properly handle the realistic mass ratio and the large spatial and temporal scales associated with the reconnection layers, while hybrid simulations cannot model the triggering physics of reconnection in a self-consistent manner. Our approach:

- We utilize the GeFi simulation model, in which the electron dynamics is handled by the gyrokinetic equations and the ions are treated as fully kinetic particles.

- In the GeFi model, the rapid electron cyclotron motion is removed, while finite electron Larmor radii, wave-particle interactions, and off-diagonal components of the electron pressure tensor (necessary for the reconnection physics) are retained.

- This treatment results in a larger time step and allows us to treat the realistic mass ratio $m_i/m_e$.

- The model is particularly suitable for plasma dynamics with wave frequencies $< \Omega_e$, and wave numbers $k_\parallel << k_\perp$.

Analytical theories on collisionless reconnection are very limited to cases with either a zero guide field or a very large guide field, and neglect many kinetic effect. On the other hand, because of its low frequency properties, the exiting fully particle simulations on tearing modes often employ $m_i/m_e < 100$.

Our approach:

- Although the GeFi model is promising to handle the electron and ion scales with the realistic mass ratio in one code essential for the reconnection research, it needs to be improved to include the effects of the background inhomogeneity because the wavelength of the tearing mode is comparable to the current sheet width. We will modify the GeFi model.

- We derive the eigenmode equations of the tearing modes based on the drift kinetic approximation. By solving them, we benchmark the GeFi model in the nonuniform plasmas.

- Using the GeFi model, various kinetic effects on the linear growth of tearing modes are investigated.

- Nonlinear evolutions of both a single tearing mode and multiple tearing modes are studied by the GeFi simulations.

While the full development of the GeFi model for the nonlinear fast reconnection is still underway, we also address in this thesis the 3D physics of large-scale kinetic structure of reconnection with the hybrid model. In the Petschek model, the reconnection layer is bounded by shocks and discontinuities. Previous simulations show the ion kinetic effect plays an important role on the structure of reconnection layer. But these simulations are limited to 1D or 2D configurations. The large-amplitude wave/discontinuity structures in the general cases with a finite X-line length have not been studied.

Our approach:

- We extend the previous hybrid simulations to 3D and investigate the 3D physics of the reconnection layer.
- Using the 3D hybrid code, the finite length X-line effects on the generation of low frequency electromagnetic waves are studied.

# Chapter 2

# Improved GeFi Model

Magnetic reconnection involves a wide range of spatial and temporal scales, and is usually triggered by micro instabilities. The reconnection changes the topology of magnetic fields on a global scale. Aiming at incorporating multi scale physics of reconnection in one code, the gyrokinetic electron and fully kinetic ion (GeFi) particle simulation scheme has been developed [*Lin et al.*, 2005; *Wang et al.*, 2008]. While the original scheme has been benchmarked for uniform plasmas, further improvement of GeFi is still required for the simulation of magnetic reconnection, in which the interested wavelengths are usually comparable to the scale length of the current sheet nonuniformity. In this chapter, a description of the improved GeFi model is given first. Then I will discuss the algorithm of the GeFi numerical scheme. Finally, the improved model will be validated for uniform plasmas.

## 2.1 Formulations of the GeFi Model

### 2.1.1 Kinetic Equations of Particles

In the GeFi model, ions are treated as fully kinetic particles, and electrons are modeled by gyrokinetic particles. The Vlasov equation is still valid for ions, while for electrons we transform the phase space variables to guiding-center variables. Different from the original GeFi scheme in Lin et al. [2005], both ions and electrons are advanced by the scalar and vector potential $\phi$ and $\mathbf{A}$.

1.Ions

In the limit of collisionless plasmas, the time evolution of ion distribution function is totally determined by the Vlasov equation:

$$\frac{\partial f_i}{\partial t} + \frac{d\mathbf{x}_i}{dt} \cdot \frac{\partial f_i}{\partial \mathbf{x}_i} + \frac{d\mathbf{p}_i}{dt} \cdot \frac{\partial f_i}{\partial \mathbf{p}_i} = 0, \tag{2.1}$$

where $\mathbf{p}_i$ is the ion canonical momentum. For a singe ion, its motion follows

$$\frac{d\mathbf{x}_i}{dt} = \mathbf{v}_i = (\mathbf{p}_i - q\mathbf{A}/c)/m_i, \tag{2.2}$$

$$\frac{d\mathbf{p}_i}{dt} = -q \cdot \nabla(\phi - \mathbf{x}_i \cdot \mathbf{A}/c). \tag{2.3}$$

2. Electrons

The particle phase space variables ($\mathbf{x}$, $\mathbf{v}$, t) can be related to the guiding-center phase space variables ($\mathbf{R}$, $\mu, \epsilon, \alpha$, t) through the following guiding-center transformation

$$\mathbf{R} = \mathbf{x} + \Omega^{-1}\mathbf{v} \times \mathbf{e}_\parallel \tag{2.4}$$

$$\mu = \frac{m{v_\perp}^2}{2\mathbf{B}} \tag{2.5}$$

$$\epsilon = \frac{1}{2}mv^2 + q\phi = \frac{1}{2m}|\mathbf{p} - \frac{e}{c}\mathbf{A}|^2 + q\phi, \tag{2.6}$$

where $\Omega$ is the particle gyrofrequency, $\mu$ is the magnetic moment, $\epsilon$ represents the Hamiltonian particle energy in the electromagnetic field, $\alpha$ is the gyro-angle. $\mathbf{e}_\parallel$ and $\mathbf{e}_\perp$, respectively, are the parallel and perpendicular units vectors relative to the equilibrium magnetic field. The relationship between $\mathbf{R}$ and $\mathbf{x}$ is illustrated in Figure.2.1, where $\rho$=$\mathbf{v}_\perp/\Omega$=$\mathbf{v}\times\mathbf{e}_\parallel/\Omega$ indicates the gyroradius, $\mathbf{v}_\perp$=$v_\perp(\mathbf{e}_1 \sin\alpha$+$\mathbf{e}_2 \cos\alpha)$. The units vectors $\mathbf{e}_1$ and $\mathbf{e}_2$ together with $\mathbf{e}_\parallel$ form an orthogonal system, in which $\mathbf{e}_\parallel = \mathbf{e}_1 \times \mathbf{e}_2$. The set of guiding-center variables ($\mathbf{R}$, $\mu, \epsilon, \alpha$, t) is equivalent to ($\mathbf{R}$, $\mu, \mathbf{v}_\parallel, \alpha$,

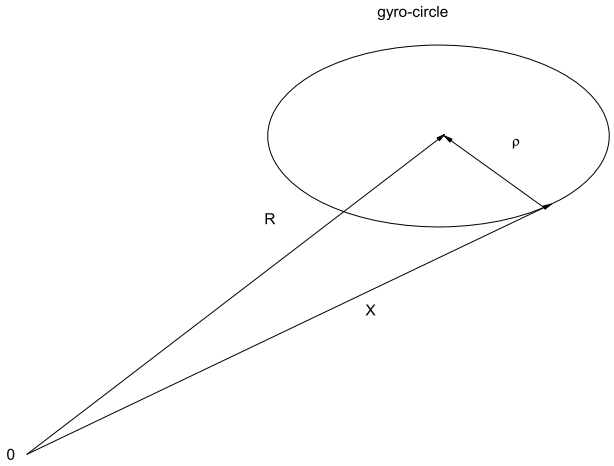


Figure 2.1: Coordinates transformation from particle phase space to guiding-center phase space.

t) , so the Vlasov equation can be expressed as

$$\frac{\partial F}{\partial t} + \frac{d\mathbf{R}}{dt} \cdot \frac{\partial F}{\partial \mathbf{R}} + \frac{d\mu}{dt} \cdot \frac{\partial F}{\partial \mu} + \frac{d\mathbf{v}_{\parallel}}{dt} \cdot \frac{\partial F}{\partial \mathbf{v}_{\parallel}} + \frac{d\alpha}{dt} \cdot \frac{\partial F}{\partial \alpha} = 0. \tag{2.7}$$

In the case that the magnetic field varies slowly in time, the magnetic moment $\mu$ is an adiabatic invariant, thus it can be treated as a constant in the guiding-center phase space. To get the electron guiding-center distribution function $F_{ge}$, one could average $F_{ge}$ around the gyro-motion [*Lee*, 1983; *Frieman and Chen*, 1982]. Noting $F_{ge}$ is independent of the gyro-angle $\alpha$, the Vlasov equation of guiding-centers can be simplified as

$$\frac{\partial F_{ge}}{\partial t} + \frac{d\mathbf{R}_e}{dt} \cdot \frac{\partial F_{ge}}{\partial \mathbf{R}_e} + \frac{d\mathbf{v}_{e\parallel}}{dt} \cdot \frac{\partial F_{ge}}{\partial \mathbf{v}_{e\parallel}} = 0. \tag{2.8}$$

We can rewrite the above equation with the electron generalized momentum $p_{e\parallel}$ as

$$\frac{\partial F_{ge}}{\partial t} + \frac{d\mathbf{R}_e}{dt} \cdot \frac{\partial F_{ge}}{\partial \mathbf{R}_e} + \frac{d\mathbf{p}_{e\parallel}}{dt} \cdot \frac{\partial F_{ge}}{\partial \mathbf{p}_{e\parallel}} = 0. \tag{2.9}$$

To determine a single electron motion, one should take the gyro-averaging of the Lorenz force, and get

$$\frac{d\mathbf{R}_e}{dt} = v_{e\|}\mathbf{b}^* + \frac{c}{q_e B_0}\mathbf{b}_0 \times [q_e < \nabla\phi^* > +\mu\nabla\mathbf{B}_0] \tag{2.10}$$

$$\frac{d\mathbf{p}_{e\|}}{dt} = -\mathbf{b}^* \cdot [q_e < \nabla\phi^* > +\mu\nabla\mathbf{B}_0]. \tag{2.11}$$

where $\mathbf{b}^* = \mathbf{b}_0 + (v_{e\|}/\Omega_e)\mathbf{b}_0 \times (\mathbf{b}_0 \cdot \nabla)\mathbf{b}_0$, $\phi^* = \delta\phi - \mathbf{v}_e \cdot \delta\mathbf{A}/c$, where $\mathbf{b}_0$ is the local background magnetic direction, $\delta\phi$ and $\delta\mathbf{A}$ are the perturbed scalar and vector potentials, respectively [*Frieman and Chen*, 1982; *Lin et al.*, 2005]. The operator $< .. >$ represents the gyro-averaging, which is carried out numerically on a discretized gyro-orbit in real space.

### 2.1.2 Maxwell Equations of GeFi Model

Once the distribution function is given, physical quantities such as the charged particle density and current density are known by integrating the distribution function in the $\mathbf{v}$ space. Then combining with Maxwell's equations, the plasma behavior is self-consistently determined.

Integrating the ion distribution function $f_i$ over the velocity moments, the number density $n_i$ and current density $\mathbf{j}_i$ are

$$n_i = \int f_i d^3\mathbf{p}_i, \tag{2.12}$$

$$\mathbf{j}_i = q_i \int \mathbf{v}_i f_i d^3\mathbf{p}_i = (q_i/m_i) \int \mathbf{p}_i f_i d^3\mathbf{p}_i - q_i^2 n_i \mathbf{A}/m_i c. \tag{2.13}$$

To proceed with the electron distribution, let us introduce the gyrokinetic ordering for electrons

$$\frac{\omega}{\Omega_e} \sim \frac{\rho_e}{L} \sim k_\| \rho_e \sim \frac{\delta\mathbf{B}}{\mathbf{B}} \sim O(\epsilon), \tag{2.14}$$

$$k_\perp \rho_e \sim 1, \tag{2.15}$$

where $\omega$ is the mode frequency of interest, $L$ is the macroscopic system length, and $k_\parallel$ is the component of the wave vector in the parallel direction with respect to the equilibrium magnetic field $\mathbf{B}_0$ [*Rutherford and Frieman*, 1968; *Taylor and Hastie*, 1968]. The total magnetic field $\mathbf{B}$ consists of the equilibrium magnetic field $\mathbf{B}_0$ and the perturbed magnetic field $\delta\mathbf{B}$, $\mathbf{B} = \mathbf{B}_0 + \delta\mathbf{B}$. $\epsilon$ is a small parameter. The interested perpendicular wavelength ranges from the scale of electron Larmor radius to the global scale length. In our GeFi model, the parallel direction is defined as $\mathbf{b}_0 = \mathbf{B}_0/B_0$.

The electron gyro-averaging charge density and current in the guiding-center phase space are

$$< n_e >= \int F_e d^3v, \tag{2.16}$$

$$< j_{e\parallel} >= \int p_{e\parallel} F_e dp, \tag{2.17}$$

To deduce Poisson's equation of the GeFi model, we start from the general form

$$\nabla_\perp^2 \delta\phi = -4\pi(q_i n_i + q_e n_e), \tag{2.18}$$

where we have assumed $\nabla_\perp^2 >> \nabla_\parallel^2$. Note $n_e$ is the electron density rather than the guiding-center density, which can be calculated from the guiding-center distribution by

$$n_e = \frac{q_e}{m_e} \int d^3v (\partial \bar{F_g} e/\partial w)[\delta\phi - < \delta\phi > + \frac{1}{c} < \mathbf{v}_\perp \cdot \delta\mathbf{A} >] + < N_e >, \tag{2.19}$$

where $w = v^2/2$ [*Lin et al.*, 2005]. By taking $|\rho_e \nabla_\perp| < 1$, Poisson's equation becomes

$$\nabla_\perp \cdot [(1 + \frac{\bar{\omega}_{pe}^2}{\bar{\Omega}_e^2}) \nabla_\perp \delta\phi] + \frac{4\pi q_e \bar{n}_e}{\bar{B}} \delta B_\parallel = \delta R_\rho + \delta H_\rho, \tag{2.20}$$

where $\delta R_\rho$ and $\delta H_\rho$ are expressed as

$$\delta R_\rho = -4\pi[q_i \delta n_i + q_e < \delta N_e >] \tag{2.21}$$

$$\delta H_\rho = 4\pi q_e [\frac{4\pi \bar{n}_e}{\bar{B}^2 c}\mathbf{j} \cdot \delta\mathbf{A} - \nabla(\frac{\bar{n}_e}{\bar{B}^2}) \cdot (\delta\mathbf{A} \times \bar{\mathbf{B}})], \tag{2.22}$$

and $\bar{\mathbf{B}}$ is the background magnetic field average over the spatial nd temporal scales of wave perturbations. Compared with equation (6) in Lin et al. [2005], the appearance of $\delta H_\rho$ is due to the usually higher order terms associated with the inhomogeneities in the background magnetic field and density.

To solve Poisson's equation, $\delta B_\parallel$ must be known. In the low frequency limit $\omega << \Omega_e$, the electron force keeps balanced in the perpendicular direction. Using this approximation, $\delta B_\parallel$ can be obtained from the equation below

$$-n_e q_e \nabla_\perp \delta\phi = \delta\mathbf{S}_B + \nabla_\perp [\frac{1}{4\pi}(1+\beta_e^*)\bar{B}\delta B_\parallel] + \delta\mathbf{H}_B^* + \nabla\delta P_\phi, \tag{2.23}$$

where

$$\delta\mathbf{S}_B = \nabla\cdot < \delta\mathbf{P}_{eg} > + \delta[\mathbf{j}_i \times \mathbf{B}/c] \tag{2.24}$$

$$\delta\mathbf{H}_B^* = \frac{1}{4\pi}\nabla[(\nabla\beta_e^*) \cdot (\delta\mathbf{A} \times \bar{\mathbf{B}}) - \beta^* \frac{4\pi\mathbf{j}}{c} \cdot \delta\mathbf{A}] - \delta\mathbf{H}_B \tag{2.25}$$

$$\delta\mathbf{H}_B = \frac{1}{4\pi}\{\delta[(\mathbf{B}\cdot\nabla)\mathbf{B}] - \nabla\delta B^2/2\} \tag{2.26}$$

$$\nabla\delta P_\phi = \nabla[\nabla \cdot (\frac{P_0 c}{B\bar{\Omega}_e}\nabla_\perp\delta\phi)] \tag{2.27}$$

$$\beta_e^* = \bar{\beta}_e/2 \tag{2.28}$$

$$\delta\Psi = \frac{(1+\beta_e^*)\bar{B}}{4\pi}\delta B_\parallel + \frac{mc^2}{4\pi q_e}\nabla_\perp(\beta_e^*\nabla\phi). \tag{2.29}$$

Compared with equation (20) in Lin et al. [2005], the newly added term $\delta\mathbf{H}_B^*$ is again due to the usually higher order contribution from the inhomogeneities in the background magnetic field and density.

In the GeFi model, $\mathbf{A_0}$ is determined by the initial condition, and the perturbation $\delta\mathbf{A}$ is solved at each simulation step. We decompose $\delta\mathbf{A}$ into three components $\delta\mathbf{A} = A_\parallel\bar{\mathbf{b}} + A_2\mathbf{e}_2 + A_z\mathbf{e}_z$, where $\mathbf{e}_2 = \bar{\mathbf{b}} \times \mathbf{e}_z$ and $\bar{\mathbf{b}} = \bar{\mathbf{B}}/\bar{B}$. Then they obey the following equations

$$(\nabla^2 - \frac{\omega_{pe}^2}{c^2} - \frac{\omega_{pi}^2}{c^2} + \bar{\mathbf{b}} \cdot \nabla^2\bar{\mathbf{b}})A_\parallel + (\bar{\mathbf{b}} \cdot \nabla^2\mathbf{e}_2)A_2 =$$
$$-\frac{4\pi}{c}(\delta\mathbf{j}_{i\parallel} + < \delta\mathbf{j}_{e\parallel} >), \tag{2.30}$$
$$(\nabla^2 + \mathbf{e}_2 \cdot \nabla^2\mathbf{e}_2)A_2 + (\mathbf{e}_2 \cdot \nabla^2\bar{\mathbf{b}})A_\parallel = -\frac{4\pi}{c}\delta j_2, \tag{2.31}$$
$$\nabla^2 A_z = -\frac{4\pi}{c}\delta j_z, \tag{2.32}$$

where

$$\delta j_2 = \frac{c}{4\pi}(\nabla \times \delta B_\parallel\bar{\mathbf{b}}) \cdot \mathbf{e}_2 \tag{2.33}$$
$$\delta j_z = \frac{c}{4\pi}(\nabla \times \delta B_\parallel\bar{\mathbf{b}}) \cdot \mathbf{e}_z. \tag{2.34}$$

Compared with the original model [*Lin et al.*, 2005], terms such as $\bar{\mathbf{b}}\cdot\nabla^2\bar{\mathbf{b}}A_\parallel$ are added in the improved model to include the inhomogeneities of the background magnetic field direction.

Different from the original scheme [*Lin et al.*, 2005], the above improved model includes the effects of nonuniformity in the background magnetic field direction $\mathbf{b}$ and density $n_e$. To appreciate the effects of the terms associated with the variation of the background magnetic field direction, in the following we compare the first and the fourth term in the Eq.2.30, $\nabla^2 A_\parallel$ and $\bar{\mathbf{b}} \cdot \nabla^2\bar{\mathbf{b}}A_\parallel$. Considering a the Harris current sheet with a sheet normal in the z direction and the antiparallel field component in the x direction, the magnetic field profile with a spatial coordinate normalized to the

current sheet half-width can be expressed as

$$B_x = B_{x0} \tanh^2(z) \tag{2.35}$$

$$B_y = B_{y0} \tag{2.36}$$

$$B_z = 0. \tag{2.37}$$

In most cases, we can estimate the scale length of $A_\parallel$ as the half current width, and therefore the the first term can be estimated as $\nabla^2 A_\parallel \approx A_\parallel$. The profile of $\bar{\mathbf{b}} \cdot \nabla^2 \bar{\mathbf{b}}$ is shown in Fig.2.2. The peak values $\bar{\mathbf{b}} \cdot \nabla^2 \bar{\mathbf{b}}$ for the cases with $\frac{B_{x0}}{B_{y0}} = 1$ and $\frac{B_{x0}}{B_{y0}} = 0.5$ are located in the center of the current sheet and have values around 1.0 and 0.22 repectively. It is seen that $B_{y0} \sim B_{x0}$, the background nonuniformity cannot be neglected.

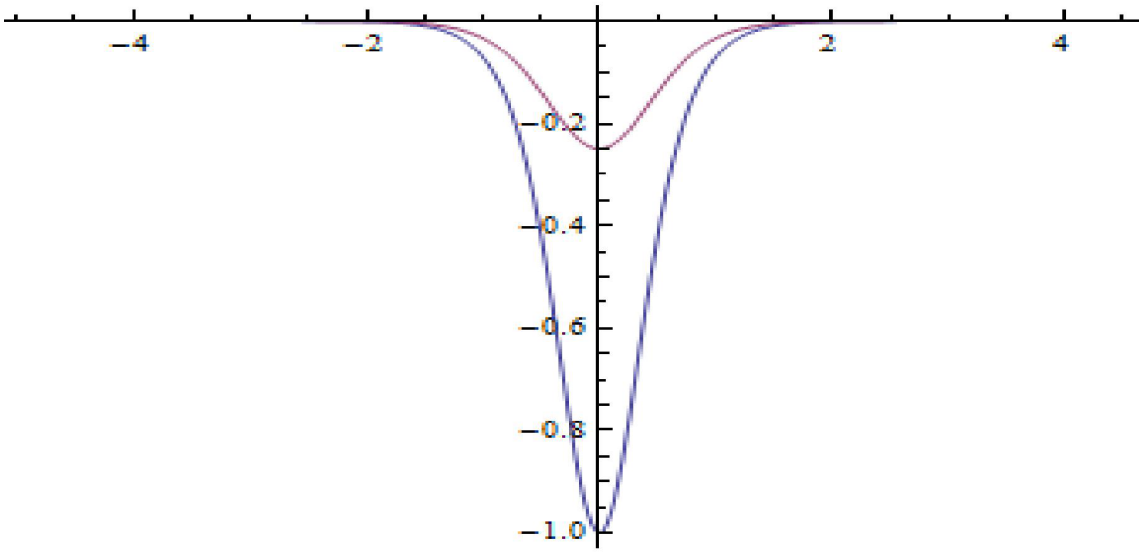


Figure 2.2: $\bar{\mathbf{b}} \cdot \nabla^2 \bar{\mathbf{b}}$ for $\frac{B_{x0}}{B_{y0}} = 1$ (black) and $\frac{B_{x0}}{B_{y0}} = 0.5$ (red). The horizontal line is the normalized z-axis.

## 2.2 Simulation Algorithms

In the GeFi simulation program, full particle method and $\delta f$ method have been used. Full particle method is a standard approach for most particle in cell codes, while $\delta f$ method is a newly developed tech to reduce the computational variations [*Lee*, 1987; *Parker and Lee*, 1993; *Chen and Parker*, 2003].

### 2.2.1 The $\delta f$ Method

The $\delta f$ method is developed to get rid of the background noise caused by the finite number of particles. Since only the perturbed distribution function is evolved in the $\delta f$ scheme, thermal fluctuations associated with the background particles are removed. To illustrate the idea of the $\delta f$ method, we first linearize the ion and electron Vlasov equations. For ions, it is

$$\frac{d\delta f_i}{dt} + \frac{q_i}{m_i}(-\nabla\delta\phi + \mathbf{v}_i \times (\nabla \times \delta\mathbf{A}))\frac{\partial f_{i0}}{\partial t} = 0, \tag{2.38}$$

and for electrons, it is

$$\begin{aligned}&\frac{d\delta F_{ge}}{dt} + [v_{e0\|}\delta\mathbf{b}^* + \delta v_{e\|}\mathbf{b}_0^* + \frac{c\mathbf{b}_0}{q_e B_0} \times (q_e < \nabla\delta\phi^* >)] \cdot \frac{\partial F_{ge0}}{\partial \mathbf{R}} \\ &+[\delta\mathbf{b}^* \cdot (\mu\nabla B_0) + \mathbf{b}_0^* \cdot (q_e < \nabla\delta\phi^* >)] \cdot \frac{\partial F_{ge0}}{\partial p_{e\|}} = 0,\end{aligned} \tag{2.39}$$

where $\delta\mathbf{b}^* = (\delta v_{e\|}/\Omega_{e0})\mathbf{b}_0 \times (\mathbf{b}_0 \cdot \nabla)\mathbf{b}_0 - (v_{e0\|}\delta\Omega_e/\Omega_{e0}^2)\mathbf{b}_0 \times (\mathbf{b}_0 \cdot \nabla)\mathbf{b}_0, \delta v_{e\|} = -q_e\delta A_\|/(m_e c)$. The distribution function $f_e$ and $F_{ge}$, the potentials $\mathbf{A}$ and $\phi$ have been divided into the equilibrium part with subscript 0 and the perturbed part with the notation $\delta$,

$$f = f_0 + \delta f \tag{2.40}$$

$$\phi = \phi_0 + \delta\phi \tag{2.41}$$

$$\mathbf{A} = \mathbf{A}_0 + \delta\mathbf{A}. \tag{2.42}$$

The linearized Vlasov equation above can be simply written in a more general form as

$$\frac{d\delta f}{dt} = -\frac{df_0}{dt}. \tag{2.43}$$

Now define the weight carried by each particle as

$$w = \frac{\delta f}{f}. \tag{2.44}$$

Since $\frac{df}{dt} = 0$, we have

$$\frac{dw}{dt} = \frac{\frac{d\delta f}{dt}}{f}. \tag{2.45}$$

Using $f = f_0 + \delta f$, one can get

$$\frac{1}{f} = \frac{1}{f_0}(1 - \frac{df}{f}) = \frac{1}{f_0}(1 - w). \tag{2.46}$$

Note that in the above approximation, only the first order is kept. It is easy to show that

$$\frac{dw}{dt} = -(1 - w)\frac{1}{f_0}\frac{df_0}{dt}. \tag{2.47}$$

Since $f_0$ is usually given in an analytical form, the time evolution of particle weights can be calculated by Eq.2.47.

### 2.2.2 Advance Particles

To advance particles in the code, we need to numerically integrate the ordinary difference equations with the following form

$$\frac{dZ}{dt} = G[Z, t], \tag{2.48}$$

where $Z$ represents the motion quantities, such as $\mathbf{R}(t), p_{\|}(t)$ and $w(t)$ of particles in the simulation. There are many methods available for the integration of an ODE, both explicit and implicit. Explicit schemes are straight forward, but should satisfy the Courant condition $\omega_{max}\delta t < 1$ in order to assure the numerical stability, where $\omega_{max}$ refers to the highest frequency in the simulation [*Hockney and Eastwood*, 1981]. Implicit schemes are generally stable, but require large computation time to solve linear algebra equations.

In the improved GeFi model, two implicit methods have been employed, the predictor-corrector method and the fourth order Runge-Kutta method [*Burden and Faires*, 2005]. In the predictor-corrector method, we need to know not only the value $Z$ at time n but also the value $Z$ at time n-1, then $Z$ at time n+1 can be calculated in two steps:

$$Predictor : \mathbf{Z}^{(n+1)} = Z^{(n-1)} + 2G^{(n)}[Z^{(n)}]\delta t$$

$$Corrector : Z^{(n+1)} = Z^{(n)} + \frac{1}{2}[\mathbf{G}^{(n+1)}[\mathbf{Z}^{(n+1)}] + G^{(n)}[Z^{(n)}]]\delta t. \tag{2.49}$$

The fourth-order Runge-Kutta method needs the value $Z$ at time n and involves four steps as

$$Z_{n+1} = Z_n + \frac{1}{6}\delta t(k_1 + 2k_2 + 2k_3 + k_4) \tag{2.50}$$

$$k_1 = G(t_n, Z_n) \tag{2.51}$$

$$k_2 = G(t_n + \frac{1}{2}\delta t, Z_n + \frac{1}{2}\delta t k_1) \tag{2.52}$$

$$k_3 = G(t_n + \frac{1}{2}\delta t, Z_n + \frac{1}{2}\delta t k_2) \tag{2.53}$$

$$k_4 = G(t_n + \delta t, Z_n + \delta t k_3). \tag{2.54}$$

Note the predictor-corrector method has the second order accuracy while the Runge-Kutta method above is of the forth order.

### 2.2.3 Operators $< .. >$ and $\bar{..}$

Two operators $< .. >$ and $\bar{..}$ have been seen in the gyrokinetic equations (Eq.2.20, Eq.2.23, Eqs.2.30-32). $< .. >$ means the average around the particle gyro-motion, while $\bar{..}$ stands for the background field averaged over the spatial and temporal scales of perturbations. In this section, I am going to introduce how to realize these operators numerically.

We use the so-called four points gyro-averaging scheme to realize $< .. >$ numerically [*Lee*, 1983; *Lee*, 1987]. The basic idea is to find four points uniformly distributed on the gyro-circle of a guiding-center and then take average of field values at these four points. To find the positions of these four points, one can follow the steps as indicated by Fig.2.3. We let $\mathbf{e}_1 = \mathbf{b} \times \mathbf{e}_z$ where $\mathbf{b}$ is the local magnetic field direction and $\mathbf{e}_z$ is the units vector along the z direction. (If $\mathbf{e_1} = \mathbf{0}$, one can just try $\mathbf{e}_x$ or $\mathbf{e}_y$ instead.) The first point $\mathbf{r}_1$ is located along the direction $\mathbf{e_1}$ at a distance $\rho_e$ from the guiding-center. Since the magnetic moment $\mu$ is conserved in the gyrokinetic model, the gyroradius can be easily calculated as

$$\rho_e = \sqrt{\frac{2\mu m_e}{B}}/q_e. \tag{2.55}$$

In the opposite direction of $\mathbf{e}_1$, another point $\mathbf{r}_2$ can be located. Now make $\mathbf{e}_3 = \mathbf{b} \times \mathbf{e}_1$. Repeating the above procedure, one can find all four points. Then the gyro-averaging field quantities are calculated as

$$< f >= \frac{1}{4}(f(\mathbf{r}_1) + f(\mathbf{r}_2) + f(\mathbf{r}_3) + f(\mathbf{r}_4). \tag{2.56}$$

To realize $\bar{..}$, we should store the data of fields before the current time step. However, how many previous steps should be kept and how to average them is still a

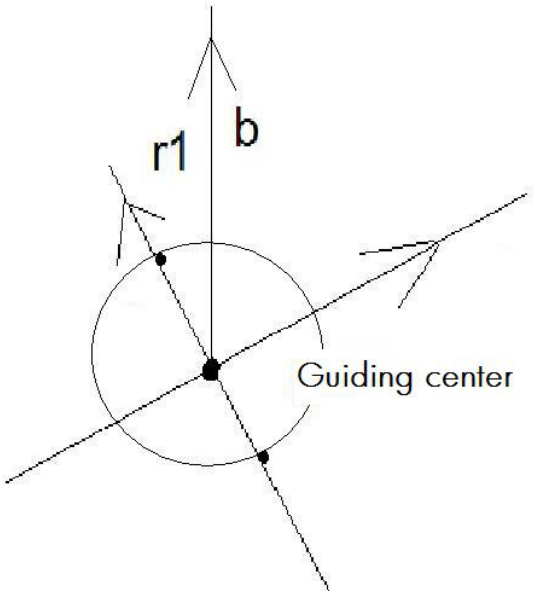


Figure 2.3: The four points gyro-averaging scheme is shown where $\mathbf{b}$ is the local magnetic direction and $\mathbf{r}_1$ is a point on the gyro-circle.

ongoing issue. For the linear simulation or the cases with $\delta B << B$, we can simply treat $\bar{\cdot}$ as the initial value of it.

### 2.2.4 Field Solver

As is seen, Maxwell's equations in the GeFi model are complicated partial difference equations (PDE) and mutually dependent on each other. To solve them, iterations are done simultaneously at each time step to obtain $\delta\phi$, $\delta\mathbf{B}_{\parallel}$, and $\delta\mathbf{A}$.

At each iteration, one has to solve the nonlinear Poison's equation with the following form

$$\nabla^2 f(x,y,z) - g(x,y,z)f(x,y,z) = C(x,y,z) \tag{2.57}$$

Two methods have been employed to handle the above task. The first one is finite differences, which is straight forward, but requires much computational time solving

the linear algebra equations, especially for 2D and 3D cases. The second one is related to our particular boundary conditions. In our simulations, periodic boundaries are adopted in the x and y directions, while conductor boundaries are used in the z direction. If $g(x, y, z)$ is only a function of $z$, i.e., $g(x, y, z) = g(z)$, we are allowed to take the fourier transform on the x and y variables and have

$$\nabla^2 f(k_x, k_y, z) - g(z) f(k_x, k_y, z) = C(k_x, k_y, z). \tag{2.58}$$

Such 1D PDE is solved quickly by finite differences. If $g(x, y, z)$ is not as simple as above, we divide $g(x, y, z)$ into two parts like $g(x, y, z) = g_0(z) + g_1(x, y, z)$. Note $g_0(z)$ is determined by the initial condition that is independent on the y and z coordinates, whereas $g_1(x, y, z)$ is treated as a perturbation. Rewrite Eq.2.57 as

$$\nabla^2 f(x, y, z) - g_0(z) f(x, y, z) = C(x, y, z) + g_1(x, y, z) f(x, y, z) \tag{2.59}$$

Eq.(2.59) is solved by iteration with the same method of Eq.(2.58). Since usually $g_1 << g_0$, it converges very fast.

## 2.3 Benchmark for Uniform Plasmas

In this section, we are going to benchmark the modified GeFi scheme for a one dimensional uniform system [*Lin et al.*, 2011]. The wave vector $\mathbf{k}$ is assumed to be along $\mathbf{x}$. The background magnetic field is in the x-z plane and is allowed to point in various directions relative to $\mathbf{k}$. The top plot of Fig.2.4 presents a comparison between the dispersion relations of $\delta\mathbf{B}_z$ for the fast magnetosonic/whistler branch obtained from the particle-in-cell GeFi simulation, shown as open dots, and the corresponding analytical linear dispersion relation based on the fully kinetic mode, shown as solid lines. Cases with $\beta_e = \beta_i = 0.04$, $m_i/m_e = 1836$, and $k_\parallel/k_\perp = 0.2, 0.06$, and 0 are plotted. The linear fluctuations in the simulation are due to random noises, as

in usual particle simulations. In the case with $k_\parallel = 0$, the electromagnetic mode approaches the quasi electrostatic lower hybrid mode, and the frequency $\omega/\Omega_i = \omega_{LH}/\Omega_i = \sqrt{\Omega_i\Omega_e}/\Omega_i = \sqrt{m_i/m_e} = 42.8$, where $\omega_{LH}$ is the lower-hybrid frequency and $\Omega_i$ is the ion gyrofrequency of the background plasma.

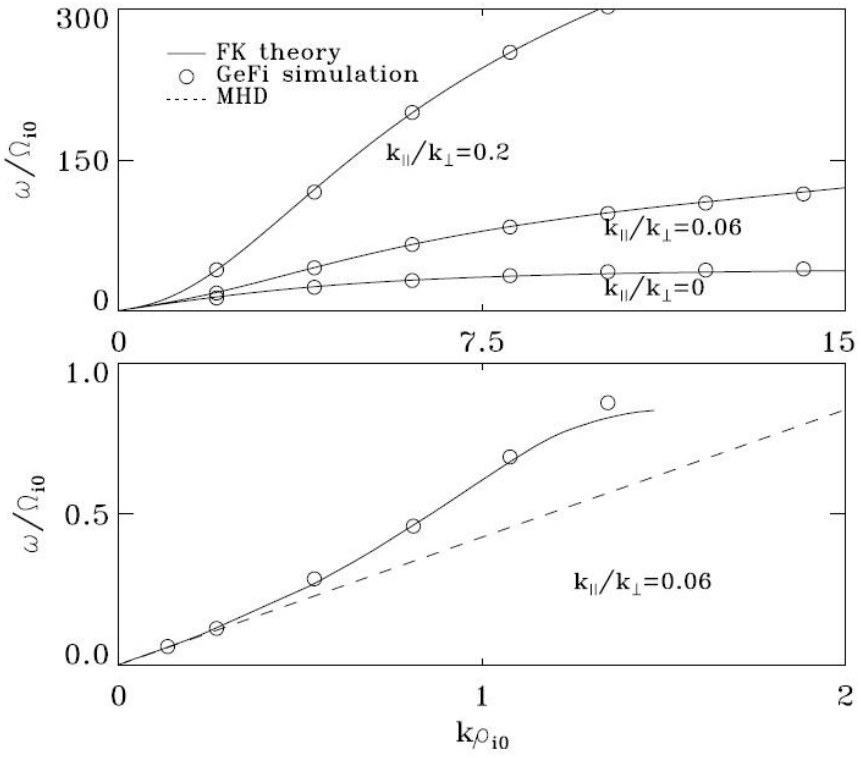


Figure 2.4: The top plot : a comparison between the dispersion relations of $\delta\mathbf{B}_z$ for the fast magnetosonic/whistler branch obtained from the GeFi simulation (open dots), and the corresponding analytical linear dispersion relation based on the fully kinetic mode (solid lines). The bottom plot : a comparison between the dispersion relations of $\delta B_y$ for the shear Alfvén/kinetic Alfvén mode branch obtained from the GeFi simulation and the analytical theory.

The bottom plot of Fig.2.4 shows a comparison between the dispersion relations of $\delta B_y$ for the shear Alfvén/kinetic Alfvén mode branch obtained from the GeFi simulation and the analytical theory for $k_\parallel/k_\perp = 0.06$. The analytical solution of the MHD shear Alfvén mode, $\omega/\Omega_i = k_\parallel v_A/\Omega_i = (k_\parallel/k)\sqrt{2/\beta_i}(k\rho_i) = 0.42$, is also shown as the dashed line.

It is seen that GeFi simulation results are in excellent agreement with the theoretical analysis for $k_{\parallel} << k_{\perp}$. The benchmark has been performed for cases with $\beta_e$ and $\beta_i$ ranging from $O(10^{-2})$ to $O(1)$.

## 2.4 Summary

In summary, our GeFi particle simulation model, in which the electrons are treated as gyrokinetic particles and ions are treated as fully kinetic particles, has been improved and modified to allow the the existence of modes with wavelengths on the same scale of the background nonuniformity. With fast electron gyro-motion and Langmuir oscillations removed from the dynamics, the GeFi model could be a powerful candidate to solve physics with realistic mass ratio $m_i/m_e$ is a global system.

The linearized GeFi scheme is benchmarked for uniform plasmas, and the simulation results using the $\delta f$ method show that the model can accurately resolve the physics ranging from Alfvén waves to lower-hybrid/whister waves, for $k_{\parallel} << k_{\perp}$ and $\omega << \Omega_e$.

Chapter 3

Simulations of Tearing Mode Instabilities under a Finite Guide Field

In this chapter, we use the improved GeFi model to simulate the tearing mode instability. The initial conditions are described in the first section. The asymptotic approximation of the Drake-Lee theory [1977a] and the eigenmode theory are presented next. Simulation results for a current sheet in a simple slab geometry are shown in the third section. The current sheet configuration that we use here has been studied by various people, and can be used to benchmark the GeFi model for the reconnection physics. In the last two sections, linear and nonlinear simulation results of tearing mode instabilities for symmetric the Harris current sheets with various guide fields are presented and discussed, repectively.

## 3.1 Simulation Model

the Harris current sheet is an equilibrium solution of the Maxwell-Vlasov system, which has been extensively used in the magnetic reconnection research [*Harris*, 1962]. The equilibrium magnetic field consists of two components, the uniform guide field $B_{y0}$ and the tanh profile of antiparallel component $B_x$,

$$\mathbf{B} = \hat{\mathbf{x}} B_{x0} \tanh(z/L) + \hat{\mathbf{y}} B_{y0}, \tag{3.1}$$

where $L$ is the half-width of the Harris current sheet. The particle density is described by

$$n = n_H sech^2(z/L) + n_{b0}, \tag{3.2}$$

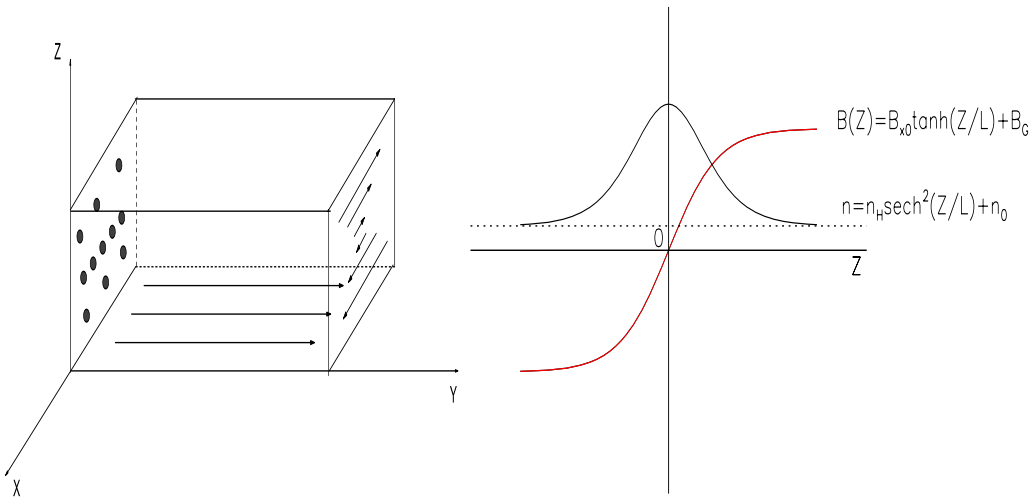


Figure 3.1: The magnetic field (left, and the red solid line on the right) and particle density (black solid line on the right) of the Harris current sheet with a tanh and sech profile along Z direction, respectively. The magnetic field consists of two components, $B_{x0}$ and $B_{y0}$. Particle density is indicated by the black line, where the dotted line means the background particle density.

where $n_{b0}$ is the background density and $n_H$ is the peak density in the current sheet. The peak density is obtained from the total pressure balance

$$n_H(T_i + T_e) = \frac{1}{8\pi} B_{x0}^2, \tag{3.3}$$

Here we have assumed that the temperatures for ions and electrons are constant everywhere. The equilibrium velocity distributions for the background ions and electrons are Maxwellian. The equilibrium velocity distributions for ions and electrons of the Harris current sheet in the GeFi model are given by [*Lin et al.*, 2005; *Wang et al.*, 2008;]

$$f_{Hi} = \frac{n_{h0}}{(2\pi T_i/m_i)^{3/2}} e^{-m_i[v_x^2+(v_y-v_{di})^2+v_z^2]/2T_i} \cdot e^{-v_{di}q_iA_y(z)/T_i} \tag{3.4}$$

$$f_{He} = \frac{n_H sech^2(z/L)}{(2\pi T_e/m_e)^{3/2}} exp(-\frac{B_x^2 m_e v_{de}^2}{B^2 2T_e}) exp(1 - \frac{m_e v_{de}}{T_e \Omega_e} \frac{dB_x}{d_z} \mu)$$

$$\cdot exp\{-\frac{1}{2T_e}[2\mu B + m_e(v_\parallel - \frac{v_{de}B_G}{B})^2]\}. \tag{3.5}$$

We focus on the instabilities in the x-z plane, where the tearing instability is included, while the current driven instabilities such as the kink instability, the lower hybrid instability are excluded. The normalization follows: the magnetic field is in the units of $B_0 = \sqrt{B_{x0}^2 + B_{y0}^2}$, the spatial length is in the units of $\rho_e$, the time step is in the units of $\Omega_e^{-1}$, particle density is in the units of $n_0$, where $n_0$ is calculated from $\beta_0 = n_0 T_e/(B_0^2/8\pi)$ and $\beta_0$ is an input parameter.

To benchmark our GeFi model, we also do the calculations for a different current sheet geometry that has been used in the previous tearing mode studies [*Drake and Lee*, 1977; *Katanuma and Kamimura*, 1980; *Wang et al.*, 2005;]. In this current sheet, the current profile along a strong guide field $B_{y0}$ is given

$$J_{y0}(z) = -en_e u_0(z) = C_1 en_e e^{-\frac{z^2}{L^2}}. \tag{3.6}$$

In addition to the guide field $B_{y0}$, the current $J_{y0}$ generates an antiparallel field

$$B_{x0}(z) = \frac{1}{2} en_e C_1 \mu_0 L\sqrt{\pi} Erf(\frac{z}{L}), \tag{3.7}$$

where the $Erf(z)$ is the error a function. In the following, I refer to this model as "the Drake-Lee current sheet". Different from the Harris current sheet, the Drake-Lee current sheet is not an equilibrium configuration, and ions are initialized without the drift motion. This current sheet is particularly suitable for the laboratory plasmas, in which there is usually a strong guide field.

## 3.2 Eigenmode Analysis

The energy exchange between tearing modes and charged particles takes place effectively in the region where the condition of the Cherenkov resonance is satisfied:

$$\omega = k_{\parallel} v_{the}. \tag{3.8}$$

Since the tearing mode is a low frequency phenomenon, the condition Eq.(3.8) is mainly satisfied in the region where $k_{\parallel} \approx 0$. If the gyroradius of charged particle is much smaller than the current sheet width, the drift kinetic approximation is valid. My benchmark of the tearing instability against the analytical theory will be conducted for this simplified situation [*Hoshino*, 1988; *Wan et al.*, 2005].

The linearized drift kinetic equation is given as

$$\frac{\partial \delta f_j}{\partial t} + v_{\parallel} \frac{B x_0}{B_0} \frac{\partial \delta f_j}{\partial x} + v_{\parallel} \frac{\partial \delta f_j}{\partial y} = [-v_{\parallel} \frac{\delta B_z}{B_0} \frac{1}{n(z)} \frac{dn(z)}{dz} - \frac{dv_{\parallel}}{dt} \frac{2(v_y - V_{dj})}{v_{thj}^2}] f_{0j}, \tag{3.9}$$

where j stands for species of particles and $u_j$ means the drift speed of fluid j [*Hoshino*, 1988; *Wan et al.*, 2005]. Note that in the above equation the electrostatic term has been neglected, since its effect has proven to be small for the tearing mode. We can rewrite $\delta B_z$ and $\frac{dv_{\parallel}}{dt}$ in terms of $\delta A_y$:

$$\delta B_z = \frac{\partial \delta A_y}{\partial x}, \tag{3.10}$$

$$\frac{dv_{\parallel}}{dt} = \frac{q_j}{m_j} \frac{\partial \delta A_y}{\partial t}, \tag{3.11}$$

Writing $\delta A_y$=$\delta A_y(z) e^{i(k_x x - \omega t)}$ and using

$$\frac{\partial}{\partial x} = i k_x, \frac{\partial}{\partial y} = 0, \frac{\partial}{\partial t} = -i\omega. \tag{3.12}$$

Eq.(3.9) becomes

$$\delta f_j = \frac{1}{\omega - \frac{v_\parallel B_{x0} k_x}{B_0}} \times (\frac{v_\parallel k_x}{B_0 n_j(z)} \frac{dn_j(z)}{dz} + \frac{\omega}{m_j} \frac{(v_y - V_{dj})}{v_{thj}^2}) f_{oj} \delta A_y. \tag{3.13}$$

$\delta A_y$ is induced by the perturbed current $\delta J_z$ through Ampere's law,

$$\nabla \delta A_y = -\mu_0 \delta J_z = -\mu_0 \sum_{j=i,e} q_j \int dv_y v_y \delta f_j \tag{3.14}$$

Combining the above two equations, we have a second order ordinary differential equation

$$[\frac{d}{dz}\alpha(z)\frac{d}{dz} - k_x^2 \alpha(z) - \sum_{j=i,e} V_j(z)]\delta A_y = 0, \tag{3.15}$$

where

$$\alpha(z) = 1 + \sum_{j=1,e} \frac{\omega_{Pj}^2 V_{dj}^2}{c^2 \Omega_j^2}, \tag{3.16}$$

$$V_j(z) = -2\frac{\omega_{Pj}^2}{c^2}(\xi^2[1 + \xi z(\xi^{'})] + \xi \frac{V_{dj}}{v_{thj}}(1 + \frac{k_x B_{x0} V_{dj}}{\omega B_0})), \tag{3.17}$$

$$\xi = \frac{\omega B_0}{k_x B_{x0} v_{thj}}, \tag{3.18}$$

$$\xi^{'} = \xi(1 - \frac{k_x B_{x0} V_{dj}}{\omega B_0}), \tag{3.19}$$

and $Z(\xi^{'})$ is the plasma dispersion a function. Eq.(3.15) is solved for eigenfunctions by following the usual shooting method, with the boundary condition $\delta A_y = 0$ at the z-boundaries on both ends. A factor of 2 difference is noticed between the expression $V_{5j}$ in Hoshino's equation(20) and the corresponding expression Eq.(3.15) for $V_j$ in our eigenmode analysis. Following the same procedure, Wan et al. [2005] has conducted the eigenmode analysis for the Drake-Lee current sheet. One should keep in mind that the drift kinetic approach is valid only when $k_\perp \rho_i << 1$.

### 3.3 Benchmark for a Simple Current sheet

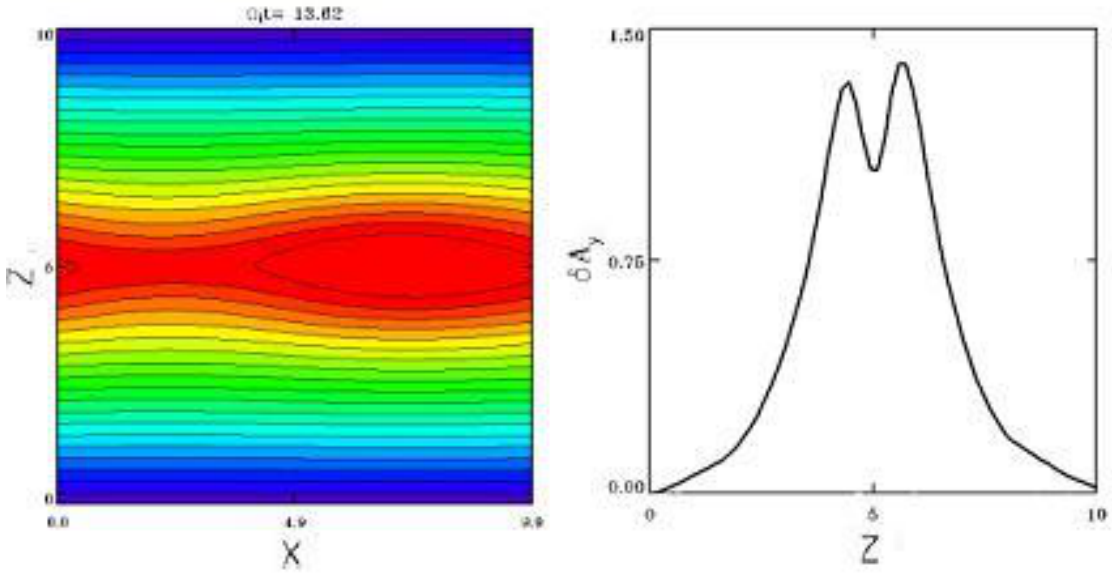


Figure 3.2: Contour of $A_y$ and eigenfunction of $\delta A_y$ with $L_z = 10.0\rho_i$, $L_x = 10.0\rho_i$, $L = 0.5\rho_i$, $B_{y0}/B_{x0} = 10$, $T_i = T_e$, and $C_1 = -0.14 v_{the}$.

Fig.3.2 shows the contour plot of $A_y$ and the corresponding eigenfunction of $\delta A_y$ obtained from the nonlinear simulation with $L_z = 10.0\rho_i$, $L_x = 10.0\rho_i$, $L = 0.5\rho_i$, $B_{y0}/B_{x0} = 10$, $T_i = T_e$, and $C_1 = -0.14 v_{the}$. A magnetic island is generated at the center with an almost symmetric structure, representing a signature of the tearing mode. $\delta A_y$ has a double-peak near the center, which is consistent with the tearing mode unstable condition $\triangle' > 0$. Recall the definition of $\triangle'$

$$\triangle' = \left(\frac{\partial \delta A_y(\Delta)}{\partial z} - \frac{\partial \delta A_y(-\Delta)}{\partial z}\right)/\delta A_y(0) \tag{3.20}$$

where $\Delta$ is the width of the singular layer.

The linear growth rate as a function of $B_{x0}/B_{y0}$ is shown in Fig.3.3 with the same parameter above except for a varying $B_{x0}/B_{y0}$. "Fixed ions" means ions are only advanced by the initial fields, meaning the motion of ions is kept unperturbed.

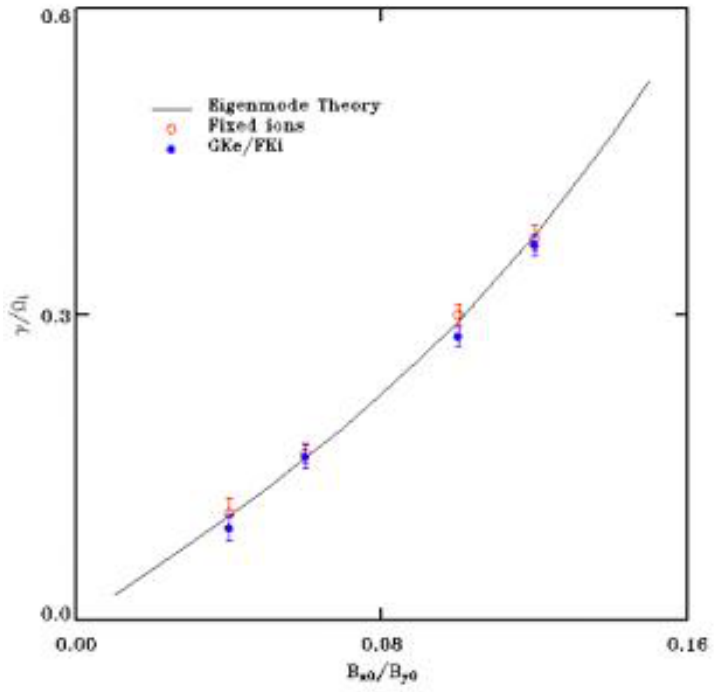


Figure 3.3: Relationship between the linear growth rate and $B_{x0}/B_{y0}$ with $L_z = 10.0\rho_i$, $L_x = 10.0\rho_i$, $L = 0.5\rho_i$, $T_i = T_e$, and $C_1 = -0.14v_{the}$

Again the linear growth rate agrees the eigenmode theory well. Two other conclusions can be reached immediately: the growth rate is increasing with $B_{x0}/B_{y0}$, and the ions contribute little to the growing of tearing modes. According to the linear theory, the linear growth rate is given by

$$\gamma = \frac{\Delta^{'} k_x v_{the}}{l_s d_e^2}, \tag{3.21}$$

where $l_s$ is the magnetic field shear length, $v_{the}$ is the electron thermal velocity. Since $l_s = \frac{B_{y0}}{\partial B_{x0}/\partial z} \propto B_{y0}/B_{x0}$, we have $\gamma \propto B_{x0}/B_{y0}$. Since the current is carried totally by electrons for the Drake-Lee current, ions contribute little to the perturbed current based on $\delta J_y = \sum_{j=i,e}(n_{j0}\delta v_{jy} + v_{j0y}\delta n_{j0})$, where the ratio of the first term between ions and electrons is $n_{i0}\delta v_{iy}/n_{e0}\delta v_{ey} = m_e/m_i$, and the second term of ions is 0.

### 3.4 Linear Simulation of the Tearing Mode in the Harris current Sheet

the Harris current sheet is the first equilibrium model of one-dimensional current sheet, which has been widely used in the investigation of reconnection. Note that since the Drake-Lee current sheet is not in equilibrium, it can only be applied to cases with $B_{y0}/B_{x0} >> 1$. In this section, I show the linear simulation results of tearing modes in the Harris current sheet.

In order to benchmark the GeFi simulation scheme against the existing eigenmode analysis, GeFi simulations with $\phi = 0$, $k_\perp \rho_i \approx 0$, $k_y = 0$ and $\delta B_\parallel = 0$ are carried out. These parameters are consistent with the assumptions of eigenmode analysis, where ions and electrons are both treated as drift kinetic particles requiring $k_\perp \rho_i << 1$. Since the electrostatic, compressible modes are neglected, we have $\phi = 0$, $\delta B_\parallel = 0$. Fig.3.4 shows the linear growth rate as a function of $k_x L$ (top) and $L/\rho_s$ (bottom) with $B_{x0}/B_{y0} = 0.075$, $T_i/T_e = 0.01$, $L/\rho_s = 0.75$ (top), and $k_x L = 0.41$ (bottom), where $\rho_s$ is defined as $\rho_s = \sqrt{m_i/m_e}\rho_e$ which is the ion gyroradius when $T_i/T_e = 1$. Again the simulation results agree with the eigenmode analysis well. In

the top figure, we can see the growth rate is maximized around $k_xL = 0.4$ and tends to be 0 for $k_xL > 1$, both of which represent the characteristics of tearing modes. The bottom figure depicts that the growth rate is decreasing with the current width with a relationship $\gamma \sim L^{-2.4}$.

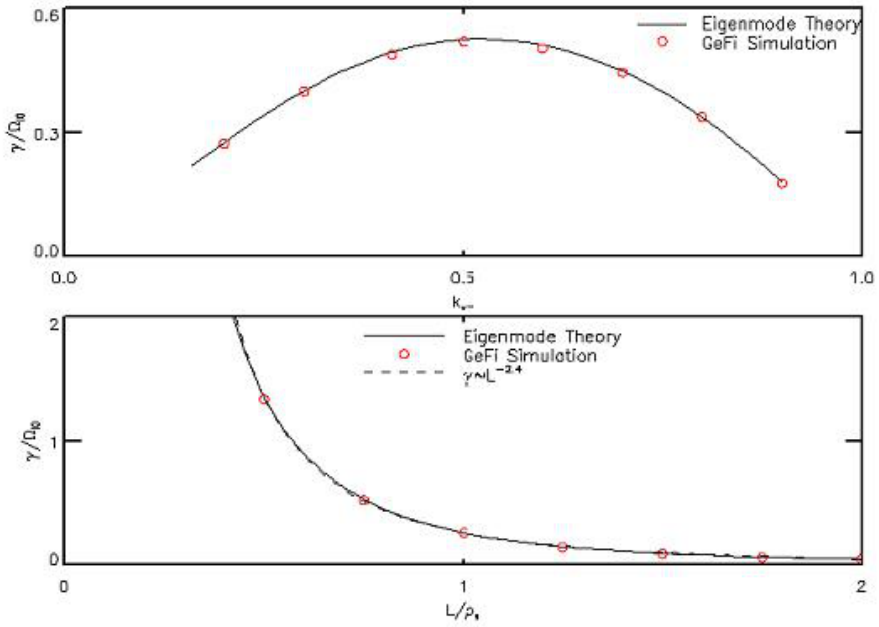


Figure 3.4: The linear growth rate as a function of $k_xL$ (top) and $L/\rho_s$ (bottom) with $B_{x0}/B_{y0} = 0.075$, $T_i/T_e = 0.01$, $L/\rho_s = 0.75$ (top), and $k_xL = 0.41$ (bottom).

The contours of the magnetic field perturbations $B_x$, $B_y$, $B_z$ from the eigenmode theory and the GeFi simulation are shown in the left Fig.3.5 with $B_{x0}/B_{y0} = 0.075$, $T_i/T_e = 0.01$, $L/\rho_s = 0.75$, $k_xL = 0.5$, while the corresponding eigenfunctions are shown on the right. Little difference exists between the simulations and the eigenmode analysis. The $B_x$, $B_y$ perturbations are symmetric, while $B_z$ shifts in the opposite directions on each side of the current sheet.

As discussed in the chapter2, the nonuniform terms associated with the magnetic field direction $\mathbf{b}$ and the electron density $n_e$ have been added into the improved GeFi

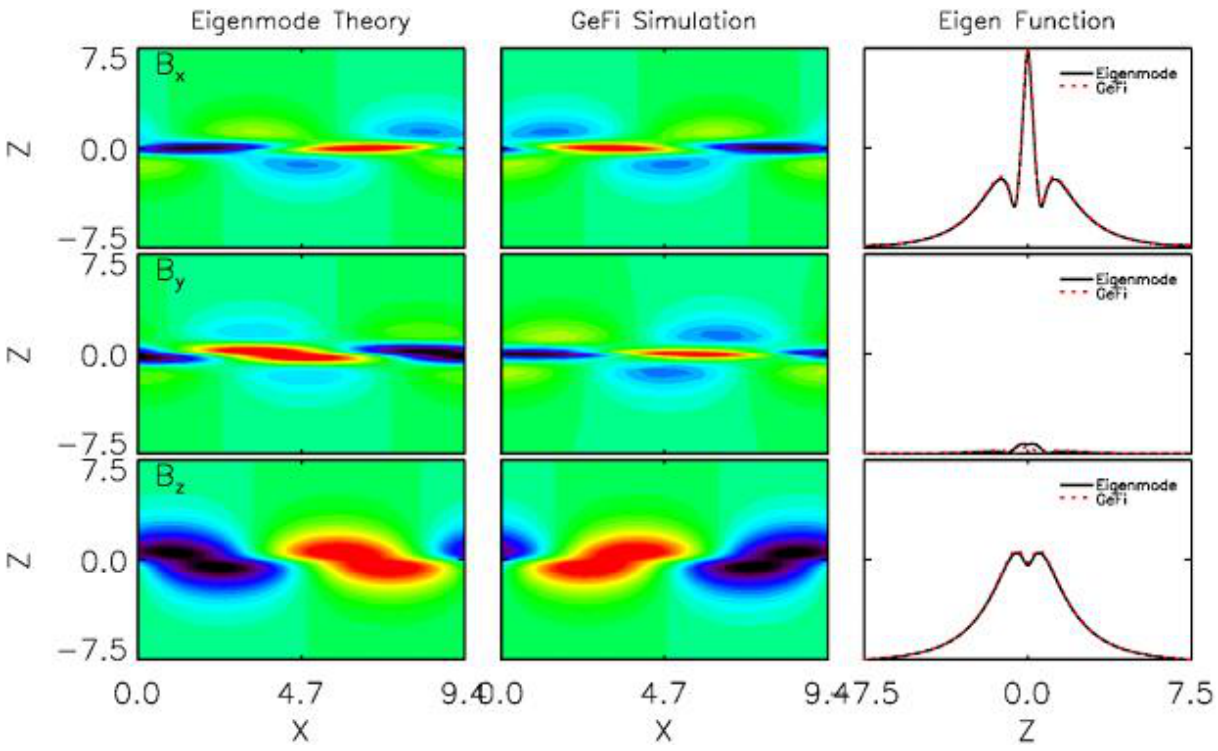


Figure 3.5: The contours of perturbations magnetic field and the corresponding eigenfunctions with $B_{x0}/B_{y0} = 0.075$, $T_i/T_e = 0.01$, $L/\rho_s = 0.75$ $k_x L = 0.5$.

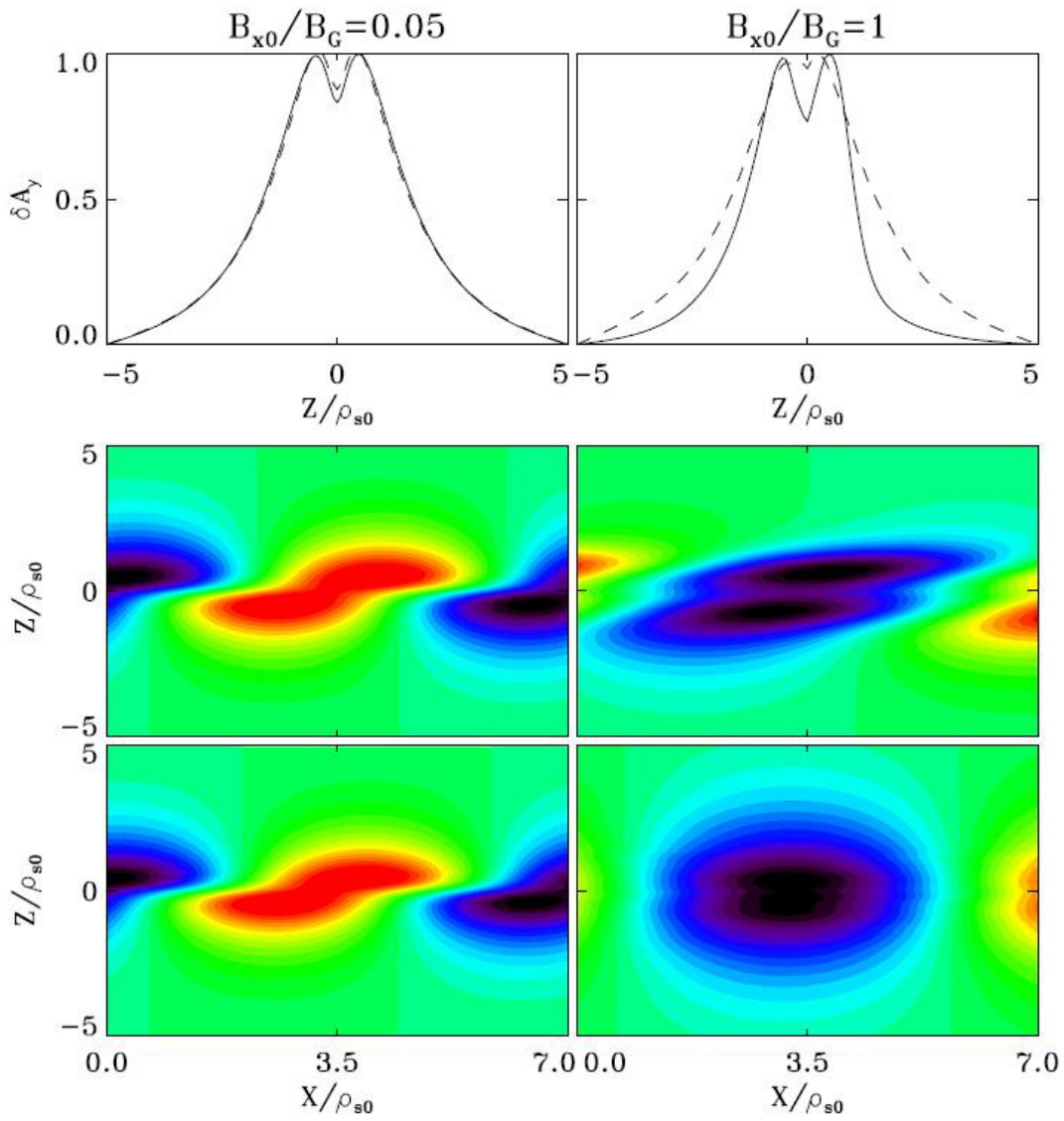


Figure 3.6: The effect of inhomogeneity with cases $B_{x0}/B_{y0} = 0.05$ (left column) and $B_{x0}/B_{y0} = 1$ (right column), for $T_i/T_e = 0.01$ and $L = 0.5\rho_s$. The top row : eigenfunctions $\delta A_y$ (solid lines from GeFi simulation, dashed lines from eigenmode calculation; the middle row : the contour of $\delta A_y$ from simulations; the bottom row : the contour of $\delta A_y$ with $\delta H_B^*$ turned off.

model. As is seen in Fig.2.2, such an effect becomes more profound as $B_{y0}$ gets smaller. The top row of Fig.3.6 shows the absolute values of eigenfunctions of $\delta A_y$ obtained from simulations with $B_{x0}/B_{y0} = 0.05$ and $B_{x0}/B_{y0} = 1$, for $T_i/T_e = 0.01$ and $L = 0.5\rho_s$. The solid line in each plot shows the simulation results based on the

improved GeFi scheme, while the dashed line corresponding to the run in which $\delta H_B^*$ is turned off. The corresponding contours of the eigenfunctions of $\delta A_y$ obtained from the GeFi simulation are shown in the middle row of Fig.3.6, while the runs with $\delta H_B^*$ turned off are plotted in the bottom row. Clearly, while the difference between the results with and without the $\delta H_B^*$ is negligible for $B_{x0}/B_{y0} = 0.05$, the corresponding eigenmode structures of $\delta A_y$ are, however, significantly different in the case with $B_{x0}/B_{y0} = 1.0$. With $\delta H_B^*$ terms included, the tearing mode shows finer structure in the current sheet. The growth rates of tearing modes for cases $B_{x0}/B_{y0} = 1.0$ with and without the $\delta H_B^*$ term are, respectively, 0.098 and 0.128. Further simulation indicates that the $\delta H_B^*$ term in general cannot be ignored for linear tearing modes when $B_{y0} \sim or < B_{x0}$.

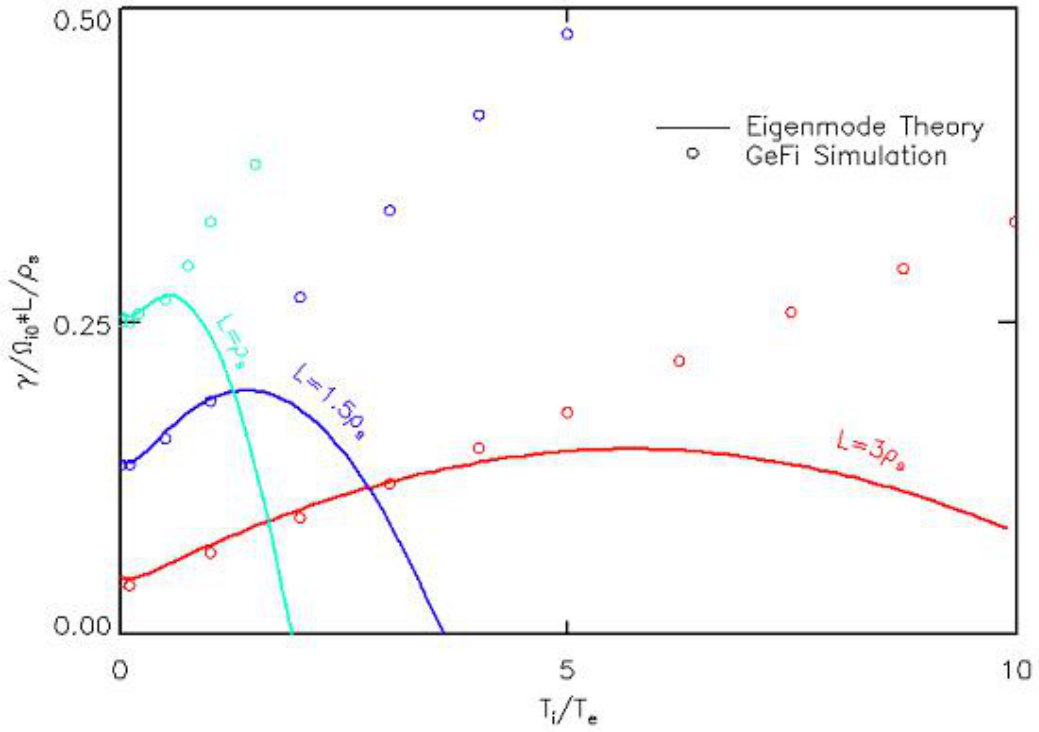


Figure 3.7: The growth rate as a function of $T_i/T_e$ for three cases $L = \rho_s, 1.5\rho_s, 3.0\rho_s$ with $B_{x0}/B_{y0} = 0.05$, $k_x L = 0.5$.

The above benchmark work has been limited to the extremely small temperature ratio between ions and electrons $T_i/T_e = 0.01$ in order to satisfy the drift kinetic ion approximation requirement $k_\perp \rho_i << 1$. Since $k_\perp \sim L^{-1}$ ($L \sim \rho_S$ for our applications) and $\rho_i = \rho_s\sqrt{T_i/T_e}$, the parameters $k_\perp\rho_i$ are evaluated as $\sim 0.1$ and $\sim 1$, respectively, for cases with $T_i/T_e = 0.01$ and for cases with the more realistic temperature ratio $T_i/T_e = 1.0$. It is expected that as the ratio $T_i/T_e$ increases, the drift kinetic ion approximation is not valid any more, and therefore the agreement between the eigenmode theory and the GeFi simulation cannot hold. The growth rate as a function of $T_i/T_e$ is plotted in Fig.3.7, where three cases with $L = \rho_s, 1.5\rho_s, 3.0\rho_s$ for $B_{x0}/B_{y0} = 0.05$ and $k_xL = 0.5$ are presented. The difference between the eigenmode theory and the GeFi simulation becomes obvious after the value $T_i/T_e$ exceeds $0.5, 1.2, 3.0$, corresponding to $k_\perp\rho_i \sim 0.7, 0.73, 0.67$, repectively, for cases with $L = \rho_s, 1.5\rho_s, 3.0\rho_s$. Our simulation results here are qualitatively consistent with the previous study by Ricci et al. [2005], in which it is pointed out both the finite electron Larmor radius effect and the ion Larmor radius effect are potentially significant in the calculation of the growth rate of tearing modes.

To explore the tearing mode properties, the realistic temperature ratio $T_i/T_e \sim 1$ should be adopted in the simulations. Fig.3.8 displays the linear growth rate as a function of $k_xL$ with $T_i/T_e = 1.0$, $L = 0.5\rho_s$ for three different guide fields $B_{x0}/B_{y0} =$ 5.0, 3.0, 1.0. The linear growth rate is rapidly reduced as the guide field deceases and $k_xL$ corresponding to the peak growth rate shifts to the short wavelength a bit. It seems not to make sense that the linear growth rate is bigger for larger guide fields. Nevertheless, we find such difference comes from the way of our normalization. Based on the Drake-Lee kinetic theory, Karimabadi et al. [2005] deduced an asymptotic formulation of the growth rate of tearing modes in the Harris current sheet as

$$\gamma/\Omega_i = 2\sqrt{2}\frac{m_i}{m_e}(1 + \frac{T_i}{T_e})\frac{1 - k_x^2L^2}{\sqrt{\pi}}\frac{B_{x0}}{B_{y0}}(\frac{\rho_e}{L})^3. \tag{3.22}$$

In the above equation the magnetic field is normalized to the antiparallel magnetic field $B_{x0}$, different from our normalization to the asymptotic total magnetic field $B_0$. Transforming it to our units, we have

$$\gamma/\Omega_i = 2\sqrt{2}\frac{m_i}{m_e}(1+\frac{T_i}{T_e})\frac{1-k_x^2L^2}{\sqrt{\pi}}(\frac{B_{x0}}{B_{y0}}+\frac{B_{y0}}{B_{x0}})(\frac{\rho_e}{L})^3. \tag{3.23}$$

$\gamma \propto (\frac{B_{x0}}{B_{y0}}+\frac{B_{y0}}{B_{x0}})$, which is increasing with $\frac{B_{y0}}{B_{x0}}$ when $\frac{B_{y0}}{B_{x0}} > 1$.

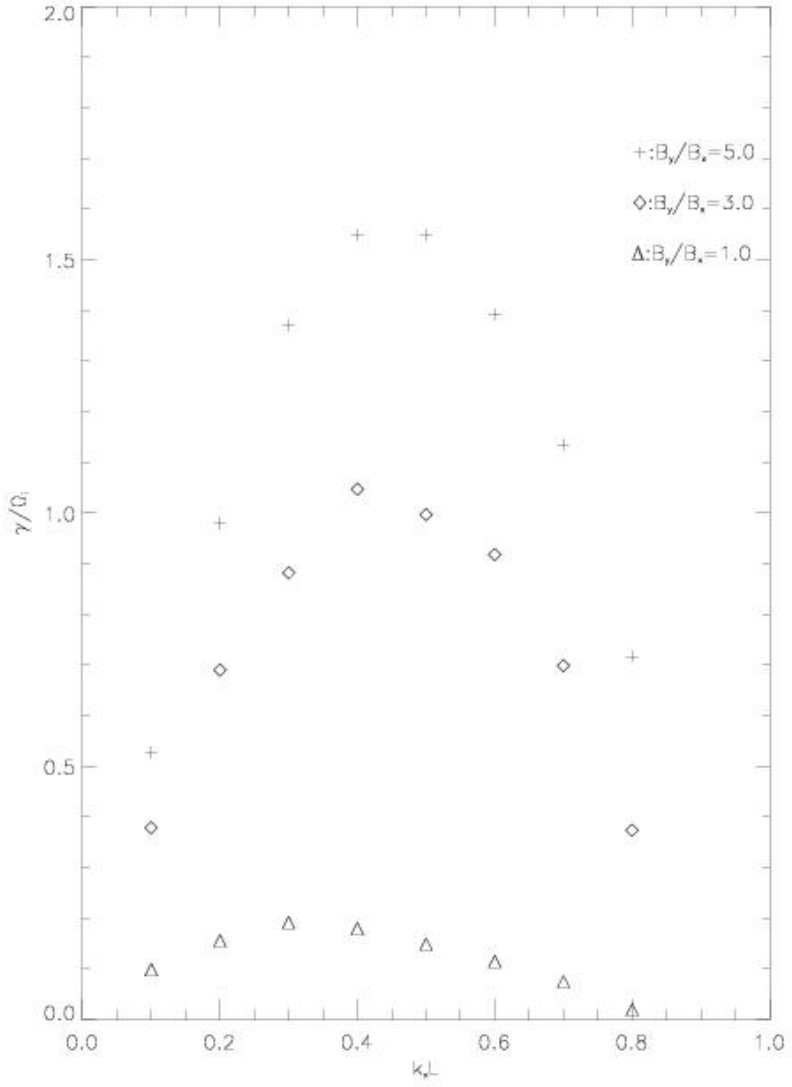


Figure 3.8: The growth rate as a function of $k_xL$ for three different guiding fields $B_{x0}/B_{y0} = 5.0,\ 3.0,\ 1.0$ with $T_i/T_e = 1.0$, $L = 0.5\rho_s$.

The ion kinetic effect in the tearing mode is examined in Fig.3.9 with $T_i/T_e = 1.0$, $B_{x0}/B_{y0} = 5.0$, $k_x L = 0.41$ for different current widthes. $\triangle$ represents cases of "with ions", while $\diamondsuit$ represents cases of "without ions" that has the same meaning of "fixed ions" we discussed above, and the line stands for the ratio of growth rate between them. Two conclusions can be reached immediately. One is that the growth rate decreases rapidly as the current sheet gets wider. The other is that ions play a significant role in the tearing mode, raising the growth rate almost by 50%. Daughton et al. [2005] has demonstrated ions can directly resonant with tearing modes and contribute to around 30% influence in the growth rate of tearing modes for thin current sheets. The compressibility of ions can also contribute to the tearing mode. Our simulations show that this term $v_{di}\delta n_i$ contributes to 10% of the total perturbed current $\delta j$. Finite ion Larmor radius effect is another potentially important factor for cases with $k_\perp \rho_i \sim 1$. One may have noticed that in the previous section our simulations have shown that the ion effect is negligible in the Drake-Lee current sheet. Such inconsistency is due to that in the Drake-Lee current sheet the current is totally carried by electrons, while in the Harris current sheet the ratio between the ion current and the electron current is determined by $j_i/j_e = T_i/T_e$.

Because of the low frequency property of tearing modes, the electrostatic effect was not considered in the kinetic theory by Drake and Lee [1977a]. Nevertheless, Hoshino [1988] pointed out that the electrostatic field influences the induced current, and modifies the linear growth rate. His analysis shows that in the presence of a guide field, the electrostatic field generated by the compressibility of electrons will increase the growth rate, but the ion effect is ignored due to its large Larmor radius. However, previous studies and our simulations have shown that the finite ion Larmor radius effect and the compressibility of ions are potentially important in the calculation of the growth rate, so it is necessary to investigate the electrostatic effect using the GeFi simulation. Fig.3.10 displays the growth rate as a function of $T_i/T_e$ with $L = 0.5\rho_s$,

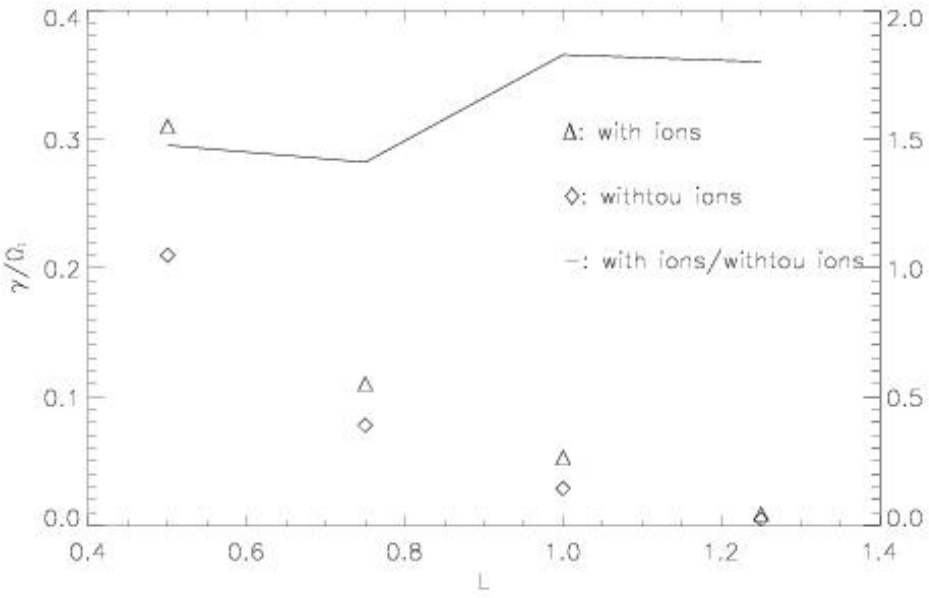


Figure 3.9: The growth rate as a function of L with $T_i/T_e = 1.0$, $B_{x0}/B_{y0} = 5.0$, $k_xL = 0.41$. $\triangle$ : cases with ions; $\diamondsuit$ : cases without ions; solid lines: the growth rate ratio between cases with ions and cases without ions.

$B_{x0}/B_{y0} = 3.0$, $k_xL = 0.41$. $\triangle$ represents cases of "with electrostatic effect", $\diamondsuit$ represents cases of "without electrostatic effect", and the line stands for the growth rate ratio between them. We see that the growth rate is increasing with $T_i/T_e$ and the influence of electrostatic effect depends on the value of $T_i/T_e$. Electrostatic effect reduces the growth rate when $T_i/T_e < 4$, but raises the growth rate when $T_i/T_e > 4$. The ion Larmor radius becomes larger as $T_i/T_e$ increases, and then Hoshino's assumption is satisfied.

In Fig.3.11, the contours of typical perturbation structures are plotted with $L = 0.5\rho_s$, $B_{x0}/B_{y0} = 3.0$, $k_xL = 0.41$, $T_i/T_e = 2.0$, where $B_x$, $B_y$, $B_z$, $n_i$,, $n_e$, $\phi$, $A_\parallel$, $U_{ix}$, $U_{iy}$, $U_{iz}$, $U_{ex}$, $U_{ey}$, $U_{ez}$, and $j_{e\parallel}$ are repectively three components of the magnetic fields, the ion density, the electron density, the electrostatic potential, the parallel component of the vector potential, three components of the ion fluid velocity, three components of the electron fluid velocity, and the parallel component of the electron

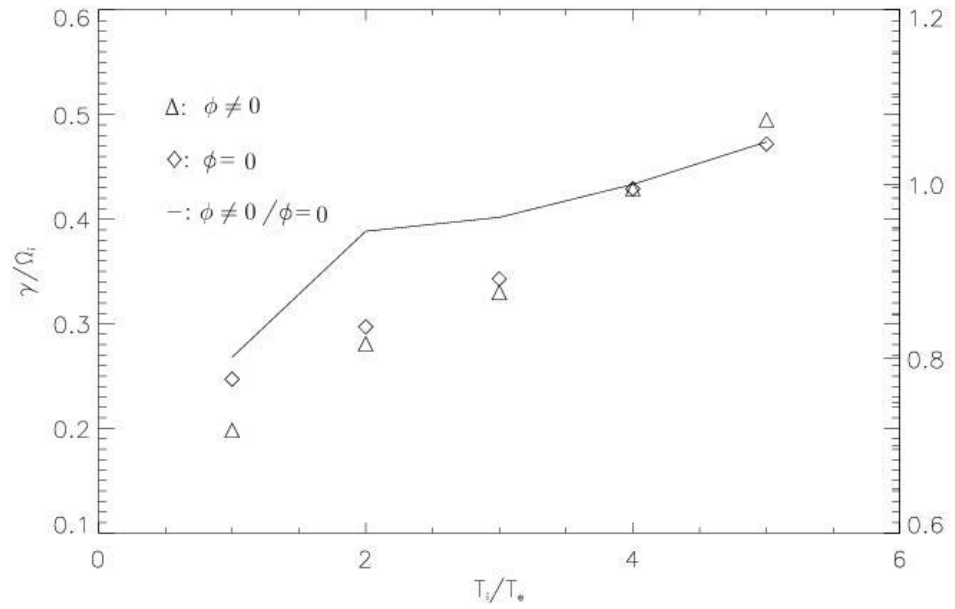


Figure 3.10: The growth rate as a function of $T_i/T_e$ with $L = 0.5\rho_s$, $B_{x0}/B_{y0} = 3.0$, $k_xL = 0.41$. $\triangle$ : with electrostatic effect; $\diamondsuit$ : without electrostatic effect; the solid line : the growth rate ratio between them.

current. An important quantity in the study of the tearing instability is the singular layer width $\triangle$, which is defined as the region where electrons can free stream along the direction of the perturbed electric field and Landau resonate with the wave. From the contour of $U_{ey}$, we can see that the singular layer $\triangle$ extends to the current sheet width $L$ with the scale of $\rho_i$, and therefore the Drake and Lee kinetic theory assumption $\triangle << L$ is clearly violated for our parameters. Considering the current parameters $\beta_e = 0.01$ and $\beta_i = 0.02$, we have $d_e/\rho_e = 1/\sqrt{\beta_e} = 10$, and $d_i/\rho_i = 1/\sqrt{\beta_e} = 7$. Since the characteristic thickness of the current sheet is comparable to $d_e$ and $\rho_i$, two factors can contribute to broaden the singular layer: one is the finite electron skin depth effect, and the other is the finite ion Larmor radius effect.

The linear stage of collisionless tearing modes contains important information of the out-of-plane perturbation $B_y$. In the limit of a weak guide field, the perturbation has a quadrupole structure, which has been identified as a key signature of the Hall

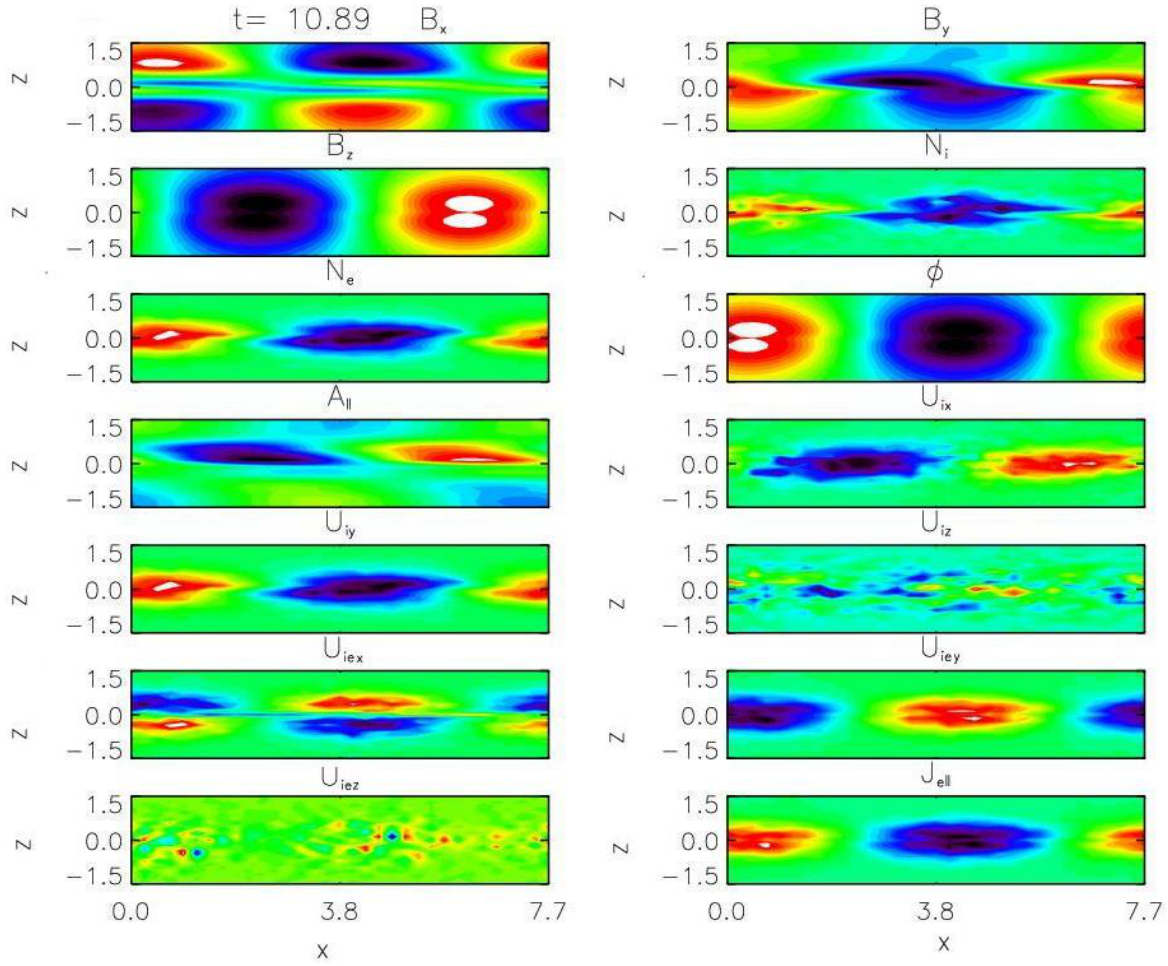


Figure 3.11: The contours of typical perturbation structure with $L = 0.5\rho_s$, $B_{x0}/B_{y0} = 3.0$, $k_x L = 0.41$, $T_i/T_e = 2.0$.

effect in fully nonlinear fast reconnection [*Sonnerup*, 1974; *Terasawa*, 1983; *Karamabadi* et al., 2004;]. Simulations by Daughton et al. [2005] show that the addition of a guide field complicates the out-of-plane perturbation and compresses the spatial width from the ion inertial scale down to the electron kinetic scale. Our simulation shows that the perturbation of $B_y$ in Fig.3.11 is not of a quadrupole structure but is located in the center of the current sheet with a certain asymmetry. Since $d_i >> \rho_i \sim L$ for our parameters, the Hall effect is excluded form the formation of the perturbation of $B_y$. Examinations on the contours of $U_{ix}$ and $U_{ex}$ indicate that the ion and electron motions follow different spatial scales and thus cause the perturbation of $B_y$. Since electrons are strongly magnetized, the electron motion is mainly guided along the magnetic field. Due to the different directions of magnetic field below and above the center of current sheet, $U_{ex}$, the projection of the electron fluid velocity on the x axis, shows a quadrupole structure and has a peak value around the O-type neutral point. Since the ion Larmor radius is comparable to the current sheet width, ions are able to move across the field lines and be accelerated directly by magnetic tension forces. The structure of $U_{ix}$ is symmetric with respect to the X-type neutral point with a $\pi/2$ phase difference compared with $U_{ex}$. The separation between $U_{ex}$ and $U_{ix}$ forms an in-plane current, and consequently generates the out-of-plane perturbation $B_y$. Nonlinear simulations by Ricci et al. [2005] show the asymmetry of $U_{ex}$ results in the compression of electron flowing along the parallel direction, and leads to a density asymmetry across the dissipation region. Our conclusions here are consistent with the discussion by Drake and Shay [edited by *Birn and Priest*, 2007].

The comparison among the growth rate of tearing modes as a function of $B_{x0}/B_{y0}$ obtained from the GeFi simulation (open circles), the eigenmode calculation (solid line) and the Drake and Lee analytical asymptotic matching [1977a] Eq.3.23 (dashed line) is plotted in Fig.3.12. Results based on the asymptotic matching Eq.3.23 deviate significantly from the eigenmode calculation and the GeFi simulation, although

the general trend of $\gamma$ versus $B_{y0}$ is consistent with them. This deviation can be understood, since in the cases shown in Fig.3.12 the thickness of current sheet L is comparable to $d_e$ at the sheet center and thus the conditions assumed in the asymptotic matching analysis break down. In addition, the ion effects are ignored in the matching theory.

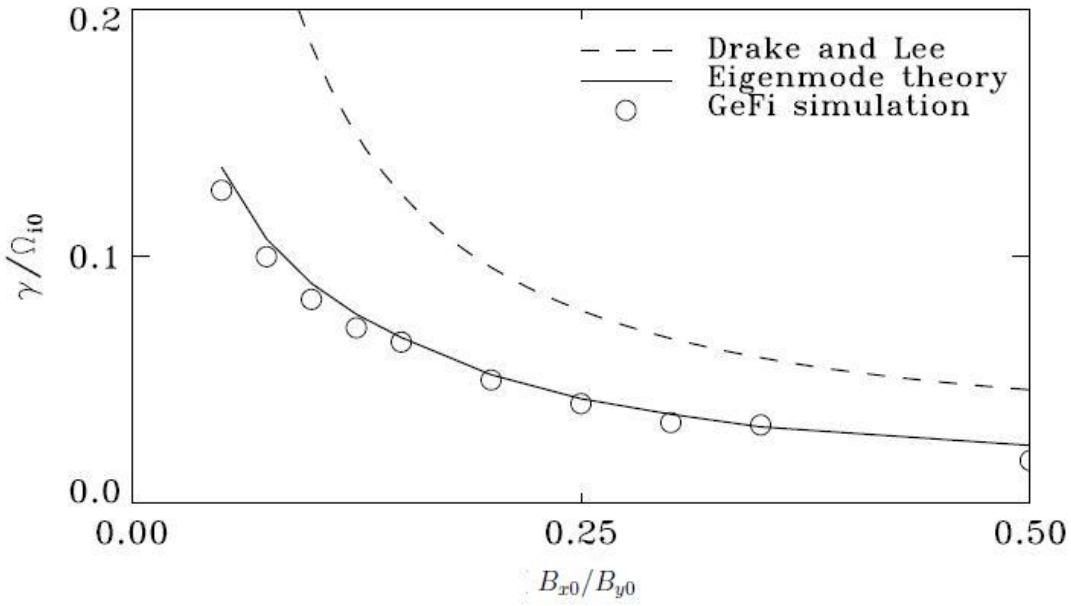


Figure 3.12: The comparison among tearing mode growth rate as a function of $B_{x0}/B_{y0}$ obtained from GeFi simulation (open circles), the eigenmode calculation (solid line) and Drake and Lee analytical asymptotic matching Eq.3.23 (dashed line).

## 3.5 Nonlinear Simulation of Tearing Modes in the Harris current Sheet

In this section, we perform nonlinear simulations to study the saturation of tearing modes. It has been suggested that when the magnetic island reaches the spatial order of the singular layer width, the electron orbits are altered. This results in the saturation of tearing modes. Two cases, one without ions and the other with ions, are shown first. In these two cases, only parallel component of the vector potential (i.e., $A_\perp$ is dropped due to weak magnetic compression) is kept in the simulation model,

which is consistent with the previous theoretical analysis. In the end, the coalescence of multiple tearing modes is studied.

Fig.3.13 shows the time evolution of the magnitude of eigenfunction $A_\parallel$ (left) and the contour plot of $A_y$ at time $t = 20.0$ (right). The parameters here are $L = 0.5\rho_s$, $B_{x0}/B_{y0} = 10.0$, $T_i/T_e = 1.0$, and $k_xL = 0.41$. This implies that only the corresponding fastest growing mode is kept in the system. The tearing mode is in the linear growing stage before $t = 9\Omega_i^{-1}$ with the growth rate $\gamma = 0.83$, which is almost the same as $\gamma = 0.812$ obtained from the linear simulation. After $t = 9\Omega_i^{-1}$, the tearing mode saturates and oscillates with a frequency $\omega = 2\pi/8 = 0.785\Omega_i$. Wan et al. [2005] deduced a relationship between the growth rate $\gamma$ and the oscillation frequency $\omega$ as $\omega/\gamma = 1.22$. Clearly our result $\omega/\gamma = 0.94$ is different from their prediction, for their analysis still relies on $d_e << L$. At $t = 20\Omega_i^{-1}$, the width of the saturation island is $w = 0.44\rho_s$, smaller than $2L = 1.0$. Considering $\beta = 0.005$, we have $d_e/\rho_e = 14.14$ and $d_e/\rho_i = 0.33$, so the saturation width of the magnetic island is on the order of $d_e$. Based on the Drake and Lee theory, the singular layer thickness in the Harris current sheet can be approximated as [*Karamabadi et al.*, 2005]

$$\Delta = \frac{1}{\sqrt{\pi}} \frac{1-(k_xL)^2}{k_xL} \frac{\rho_e^2}{L} \frac{B_0}{B_{x0}} (1 + T_i/T_e). \tag{3.24}$$

For our parameters, the above equation gives $\Delta = 1.1\rho_e$, which is much smaller than the saturation island width $w$ obtained from the simulation. Clearly the finite electron skin length effect that is neglected in the Drake and Lee theory can broaden the singular layer and yield a larger saturation amplitude.

The results of simulation with the same parameters above but including the ion motion are depicted in Fig.3.14. It shows the time evolutions of the magnitude of eigenfunctions $n_e$ (top left), $n_i$ (top right), $A_\parallel$ (bottom left), and the contour plot of $A_y$ at time $t = 20\Omega_i^{-1}$ (bottom right). Two main differences can be observed

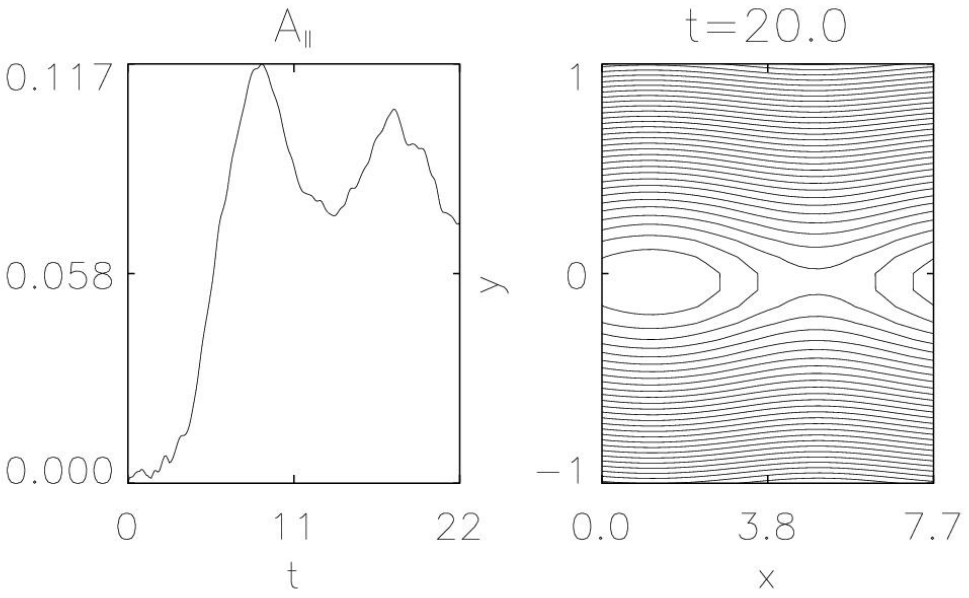


Figure 3.13: The time evolution of the magnitude of eigenfunction $A_\parallel$ (left) and the contour plot of $A_y$ at time $t = 20\Omega_i^{-1}$ (right) with $L = 0.5\rho_s$, $B_{x0}/B_{y0} = 10.0$, $T_i/T_e = 1.0$, and $k_xL = 0.41$.

by comparing with the case without ions: one is the faster oscillation frequency $\omega = 1.1\Omega_i$; the other is the wider saturation island $w = 1.05\rho_i \approx 2L$. By including the ion influence that was neglected in the work of Drake and Lee, it has been suggested that much larger saturation amplitudes comparable to the ion gyroradius could be obtained [*Galeev*, 1988; *Kuznetstova and Zelenyi*, 1990]. The strong correlations between the time evolution of $\delta A_\parallel$ and $n_i$ in Fig.3.14 proves that ions play a significant role in the saturation mechanism.

The nonlinear evolution of multiple tearing modes is shown in Fig.3.15. Four unstable modes are kept in the domain, with the wave number $k_xL = 0.11$ (mode1), $k_xL = 0.22$ (mode2), $k_xL = 0.33$ (mode3), and $k_xL = 0.44$ (mode4) respectively. Note that the wavelength of mode1 is the same as the system length in the x direction. Since mode4 corresponds to the wavelength with roughly the largest growth rate, four magnetic islands are formed at the initial stage. After $t = 8.72\Omega_i^{-1}$ , the islands start

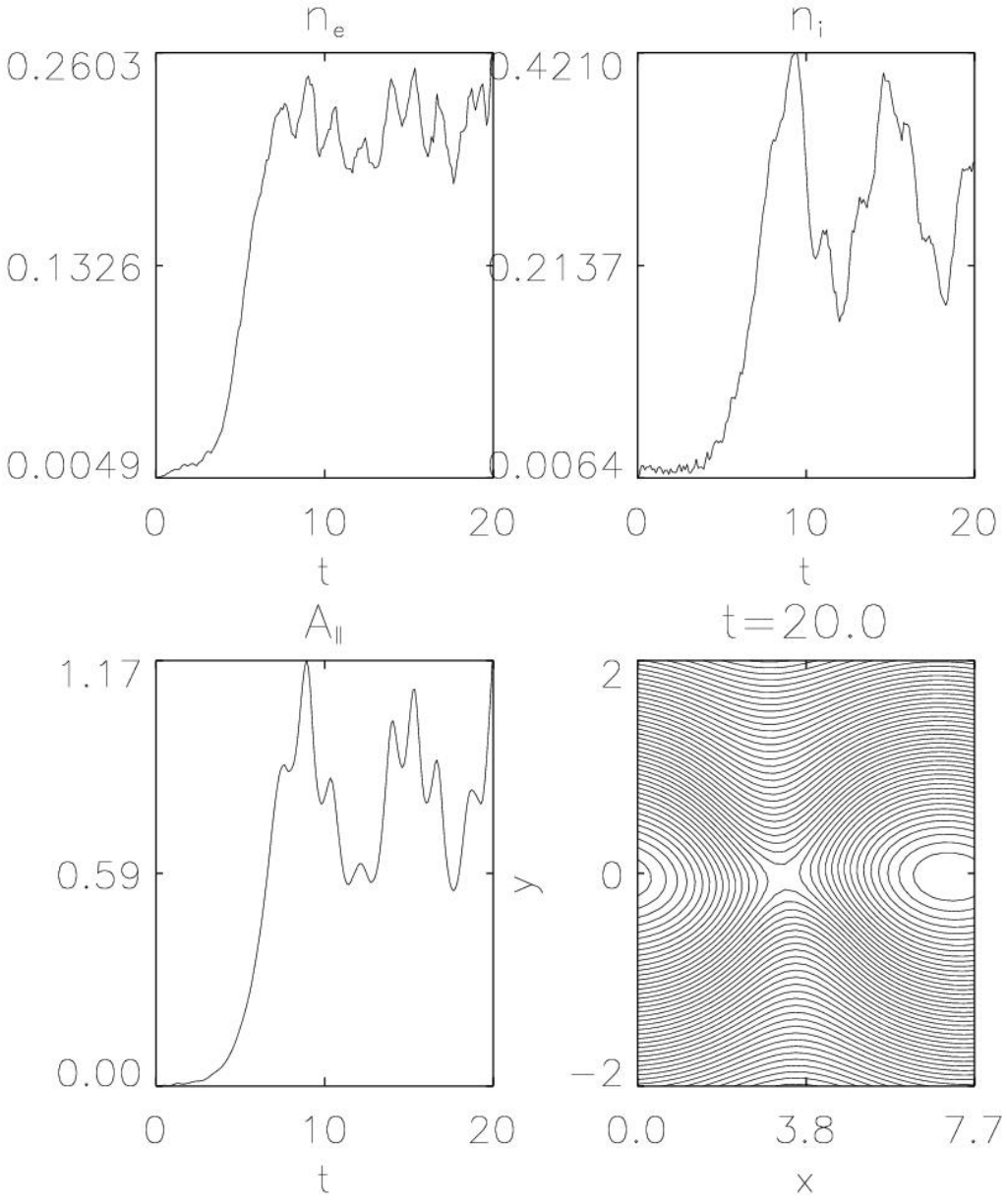


Figure 3.14: The time evolutions of the magnitude of eigenfunction $n_e$ (top left), $n_i$ (top right), $A_\parallel$ (bottom left), and the contour plot of $A_y$ at time $t = 20\Omega_i^{-1}$ (bottom right) including ions.

to coalesce due to the attraction between currents, and two wider islands become dominated at $t = 13.08\Omega_i^{-1}$. Two much smaller plasmoids become evident at $t = 15.26\Omega_i^{-1}$. The formation of such secondary island may be due to the thin current near the x-point [*Daughton et al.*, 2005; *Karamababidi et al.*, 2005]. The coalescence of two big islands continues to compress the smaller plasmoid and triggers a forced reconnection. At $t = 17.44\Omega_i^{-1}$, a very narrow reconnection layer can be seen between two large islands. At $t = 19.62\Omega_i^{-1}$, the system relaxes back to the state that two islands are dominated.

Fig.3.16 shows the time evolution of the magnitude of eigenfunction $A_\parallel$ for the four modes. Initially only the magnitude of mode4 corresponding to the fastest growing tearing mode is increasing. Around $t = 9\Omega_i^{-1}$, the coalescence of the islands transfer the energy from mode4 to mode2. At $t = 14\Omega_i^{-1}$, all modes except for mode2 start to increase rapidly. This is due to the generation of small islands near the X-lines as shown in Fig.3.16 at $t = 15.26\Omega_i^{-1}$. The magnitude of all modes are deceasing dramatically after $t = 17\Omega_i^{-1}$, because the energy is released by the forced reconnection as discussed above.

### 3.6 Summary

In this chapter, the GeFi simulation model with the realistic electron/ion mass ratio is employed to study tearing mode instabilities under a finite guide field. The results are summarized below:

1. The GeFi simulation model is benchmarked with tearing mode instabilities in a simple current sheet. Our results agree with the eigenmode analysis and the previous studies.

2. With the drift kinetic approximation, the eigenmode theory for the Harris current sheet is deduced. For cases with $T_i << T_e$ when the drift kinetic approximation is valid, the GeFi simulation results agree with the eigenmode analysis.

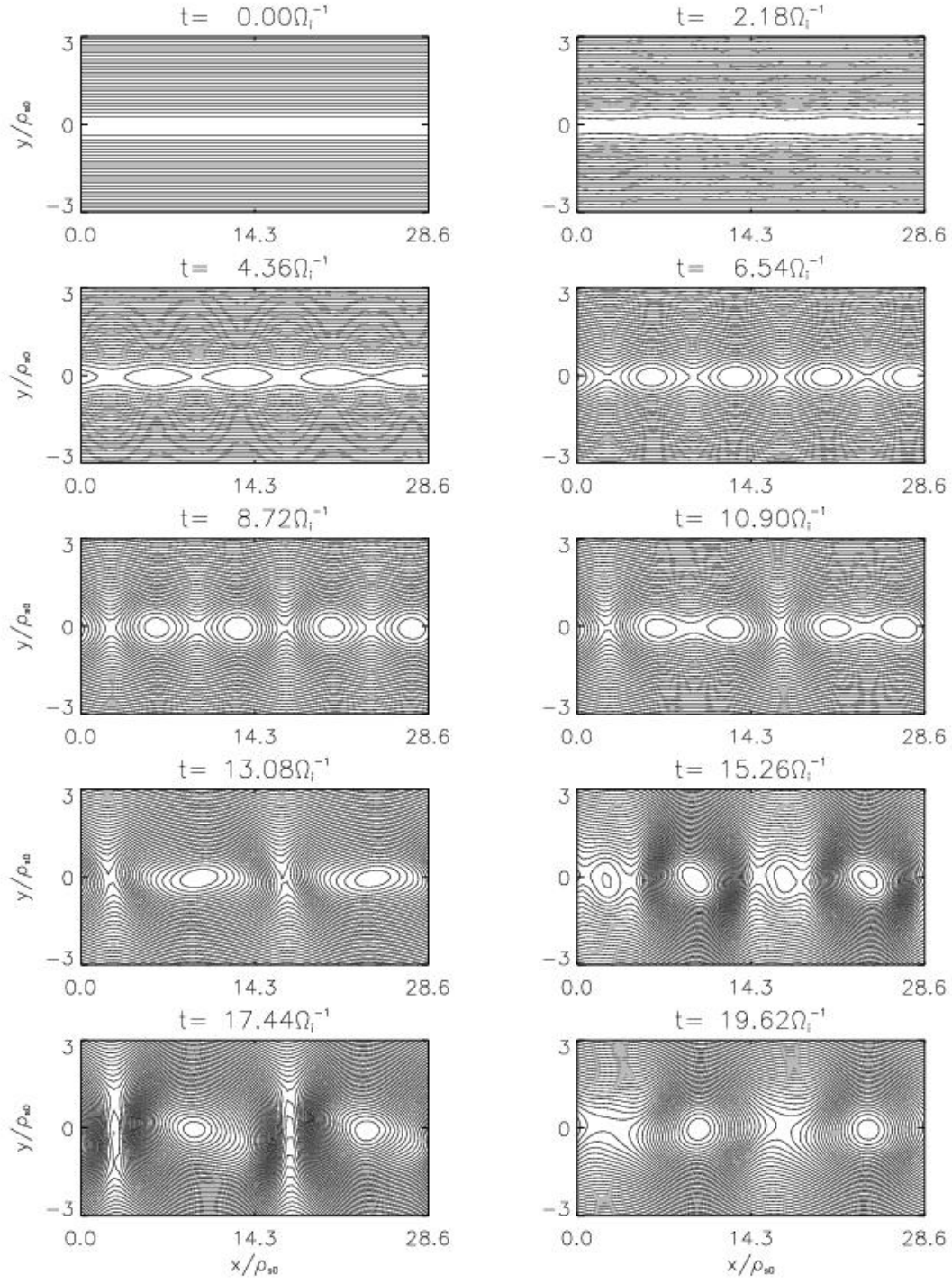


Figure 3.15: Contours of vector potential $A_y$ at different times for the case with four unstable modes.

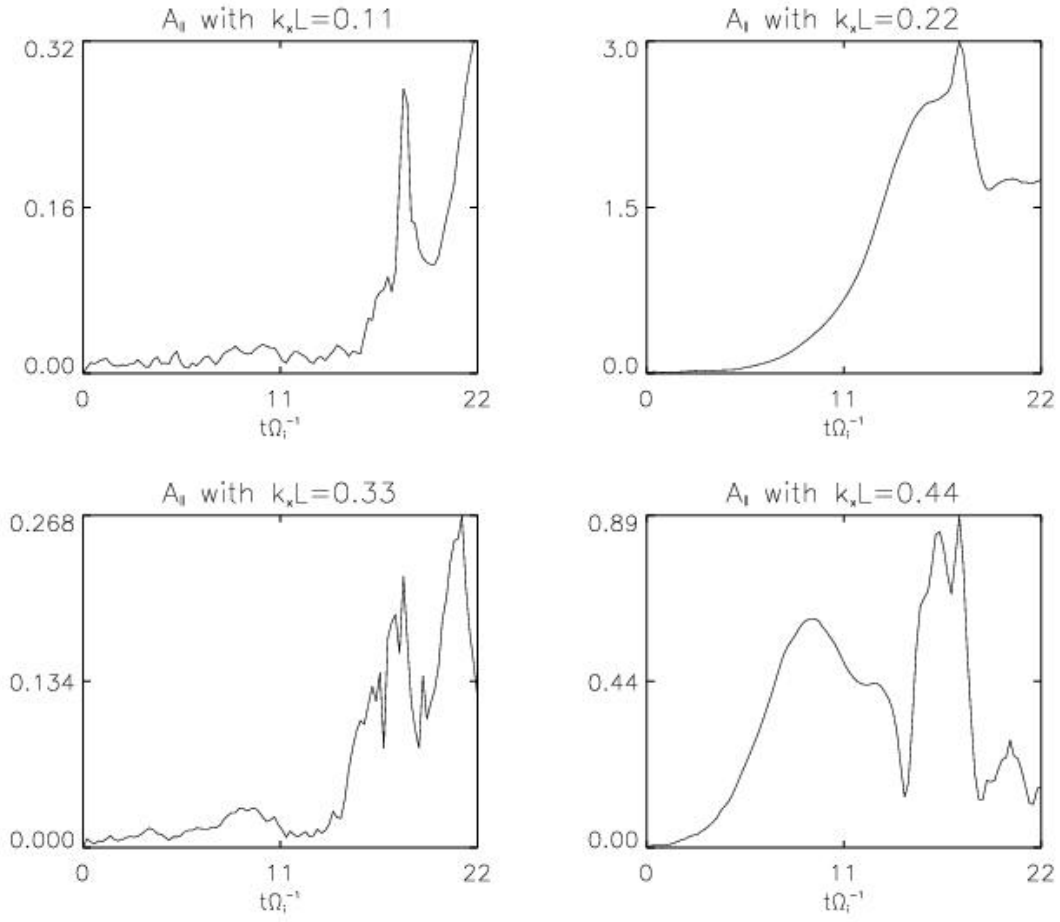


Figure 3.16: The time evolution of the magnitude $A_{\parallel}$ for the four modes.

3. The inhomogeneity terms affect the structure of tearing modes, and cannot be neglected when $B_{y0} \sim B_{x0}$.

4. For the temperature ratio $T_i/T_e \sim 1$, the simulation studies reveal the relationship between the growth rate of tearing modes and $k_x L$, $B_{x0}/B_{y0}$, $T_i/T_e$, and $L/\rho_s$.

5. The electrostatic effect is negligible on the calculation of the growth rate of tearing modes.

6. In the general cases in which the ion gyroradius is comparable to the current sheet width, the ion effects are found to play a significant role on the calculation of the growth rate of tearing modes. In such cases, the Drake and Lee theory [1977a] and the eignemode analysis based on the drift kinetic assumption are not invalid.

7. The nonlinear GeFi simulation shows that the ion effect can broaden the width of saturated magnetic islands from the electron dynamic spatial scale to the ion gyroradius.

8. The case with multiple tearing modes shows that the coalescence of magnetic islands can form a larger saturation island than the case of a single tearing mode. During the process of coalescence, small magnetic islands are formed around the X point. The small-scale magnetic reconnection can occur when the small magnetic islands are compressed by the large magnetic islands. This process results in fast energy release.

# Chapter 4

# Generation of Low Frequency Electromagnetic Waves by Magnetic Reconnection under a Finite Guide Field

In the collisionless plasma, magnetic reconnection is usually triggered by micro instabilities. The change of topology of the magnetic field lines and and the perturbations in the diffusion region will lead to the generation of low frequency electromagnetic waves. Previous 2D simulations of steady-state reconnection have found these waves to be present in the form of MHD discontinuities, as also observed in the magnetosphere as well as the interplanetary space [*Sonnerup et al.*, 1981; *Phan et al.*, 2006]. In this Chapter, we investigate the 3D structure of the reconnection layer. The parameters chosen will be suitable for the Earth's magnetosphere. It is found that kinetic Alfvén waves are present in the 3D reconnection. First the simulation model is introduced. Then a brief review of the kinetic Alfvén wave is given. Our results show the kinetic effects play an important role in the 3D reconnection geometry. The simulation results will be presented in the third section.

## 4.1 3D Hybrid Simulation Model

In the hybrid code, ions are treated as discrete particles and electrons are treated as a massless fluid. The code was developed by Swift[1995], which has been used in a general curvilinear coordinate system to model the Earth's magnetosphere. In this study we use a Cartesian coordinate system to model the generation of low frequency electromagnetic waves.

In the hybrid code, quasi charge neutrality is assumed. The equation for the ion motion is given by

$$\frac{m_i}{q_i}\frac{d\mathbf{v}_i}{dt} = \mathbf{E} + \mathbf{v}_i \times \mathbf{B} - \mu(\mathbf{V}_i - \mathbf{V}_e) \tag{4.1}$$

where $\mathbf{v}_i$ is the ion particle velocity, $\mathbf{E}$ is the electric field in units of ion acceleration, $\mathbf{B}$ is the magnetic field in units of the ion gyrofrequency, $\mu$ is the collision frequency which is used to model the resistivity at the X-line, and $\mathbf{v}_i$ and $\mathbf{V}_e$ are the bulk of flow velocities of ions and electrons, repectively. The electron momentum equation is written in the form

$$\mathbf{E} = -\mathbf{V}_e \times \mathbf{B} - \mu(\mathbf{V}_e - \mathbf{V}_i) + \nabla \mathbf{P}_e, \tag{4.2}$$

where $\mathbf{P}_e$ is the electron pressure. The electron flow speed is evaluated from Ampere's law,

$$\mathbf{V}_e = \mathbf{V}_i - \frac{\nabla \times \mathbf{B}}{\alpha N}, \tag{4.3}$$

where $\alpha = 4\pi e^2/m_i c^2$, $e$ is the electron charge, $m_i$ is the ion mass, and $N$ is the particle number density. The magnetic field is advanced in time using Faraday's law

$$\frac{\partial \mathbf{B}}{\partial t} = -\nabla \times \mathbf{E}, \tag{4.4}$$

where the electric field is calculated from Eq.4.2.

In the simulation the ion particle velocity is updated at half time steps with a second-order accuracy. The magnetic field and the particle positions are advanced at the integer time step. The time step is chosen to satisfy the Courant condition with respect to the whistler mode. In the simulation, the magnetic field is advanced 10 time steps for every time step the ion velocities are advanced.

Here, the magnetosphere plasmas are considered, in particular for the symmetric reconnection as usually occurring in the magnetostail. The simulation domain is a cube with x being normal to the current sheet and z being the antiparallel magnetic

field direction. Different with the previous chapters, we choose the z direction as the antiparallel direction, which is generally used in the magnetospause research. The initial profile of the z component magnetic field is given by

$$B_z(x) = B_{z0}(x)\tanh(x/\delta) \tag{4.5}$$

where $B_{z0}$ is the z-component magnetic field in the lobes and $\delta$ is the half-width of initial current sheet. The profile of the y-component magnetic field, i.e., the guide field in the lobes, is assumed to be

$$B_y = B_{y0}. \tag{4.6}$$

The initial x-component magnetic field is $B_x = 0$. The profile of ion thermal pressure is determined from the total pressure balance across the current sheet. A constant, isotropic temperature with $T_i = T_e$ is assumed, where $T_i$ is the ion temperature and $T_e$ the electron temperature. The ion number density is thus given by

$$N(x) = N_0(1 + \frac{1}{\beta_0}[1 - B_{z0}^2/B_0^2 tanh^2(x/\delta) - B_{y0}^2/B_0^2]) \tag{4.7}$$

where $B_0 = (B_{z0}^2 + B_{y0}^2)^{\frac{1}{2}}$ is the total magnetic field in each lobe.

We study the evolution of a spontaneous reconnection [*Scholer*, 1989]. The dynamics are not driven. A constant resistivity in time is imposed in the system to trigger the reconnection. The resistivity is modeled through a collisional term in the ion equation of motion and the electron momentum equation. The collision frequency is assumed to be

$$\nu = \nu_0 exp(-(x^2 + z^2)/\lambda_0^2) exp(-y^2/\eta_0^2) \tag{4.8}$$

where $\nu_0 \sim 0.1 - 2\Omega_i$ and $\Omega_i$ is the ion gyrofrequency in the lobes. We define $\eta_0$ as the half-length of X-line.

In our simulation, the time is in units of $\Omega_i^{-1}$. For the results shown in this thesis the magnetic field is expressed in units of $B_0$, the ion number density in units of $N_0$, and the temperature in units of the lobe temperature $T_0$, where the subscript "0" represents the quantities in the lobes. The velocity is normalized to the lobe Alfvén speed $V_{A0}$, and the spatial coordinate is normalized to $d_i$ the lobe ion inertial length.

The conductor boundary is used in the x direction, , while the periodic boundaries are used in both the z and the y directions. To limit the boundary effect, the simulation stops when the waves propagate near the boundaries. The domain size $X \times Y \times Z$ is $128d_i \times 128d_i \times 256d_i$ with the grid size $\Delta x = 0.5d_i$, $\Delta y = 2.0d_i$, and $\Delta z = 1.0d_i$. Almost 100 particles per cell are placed in the lobe region.

## 4.2 Properties of Kinetic Alfvén Waves

The Alfvén wave is one of the most important wave modes in magnetized plasmas. It exists due to the balance between the magnetic field tension and ion inertia. These waves were first theoretically predicted by H.Alfvén and are now called shear Alfvén waves because the perturbations of the magnetic field are perpendicular to the ambient field and wave vector. When the perpendicular wavelengths are comparable to the ion gyroradius $\rho_i$, the properties of shear Alfvén waves need to be modified. In a plasma with intermediate beta values ($m_e/m_i < \beta_e << 1$)), the modified waves are usually refereed as kinetic Alfvén waves.

Starting from the two fluid-MHD equations, one can deduce the dispersion relationship of kinetic Alfvén waves as [*Stix*, 1992]

$$\omega^2 = k_\parallel^2 V_A^2 (1 + (1 + \frac{T_i}{T_e}) k_\perp^2 \rho_i^2). \tag{4.9}$$

Obviously the kinetic Alfvén wave is dispersive, while the shear Alfvén wave is non-dispersive.

Another important difference between the shear Alfvén wave and the kinetic Alfvén wave is that the kinetic Alfvén wave is compressible and generates an electric field parallel to the ambient magnetic field by

$$E_{\parallel} = -\frac{T_e}{en_e}\nabla_{\parallel} n_e. \tag{4.10}$$

It is suggested that such electric field plays an important role in the energy transport processes and particle heating/acceleration of space plasmas.

## 4.3 Simulation Results

Two typical cases with $B_{y0} = 0.5B_{z0}$ are presented in this section. One possesses an infinitely long X-line, and the other possesses with a finite X-line. The cases with an infinite X-line corresponds to $k_y \sim 0$. Since the propagation of waves is almost limited in the x-z plane, results similar to the 2D simulations are expected although some differences are found to exist. For the case with a finite X-line, the spatial effects along the y direction are found to lead to $k_y \neq 0$, which results in the propagation of waves very different from those in 2D simulations.

### 4.3.1 Case with an Infinite X-line: $2\eta_0 = \infty$

Fig.4.1 shows the contour plots of the magnetic field $B_x$, $B_y$, $B_z$, the ion fluid velocity $V_x$, $V_y$, $V_z$, the temperature $T$, the particle number density $N$, and the configuration of magnetic field lines in the x-z plane located at $y = 0$ when $t = 150\Omega_i^{-1}$. A plasma bulge and a trailing quasi-steady reconnection layer are formed in the outflow region of magnetic reconnection, as shown in the magnetic field and plasma plots in Fig.4.1. The magnetic field decreases and the plasma temperature increases from the lobe to the center of the reconnection layer. Since $k_y \sim 0$, the field and

plasma properties in the x-z planes of other y positions resemble the results shown here.

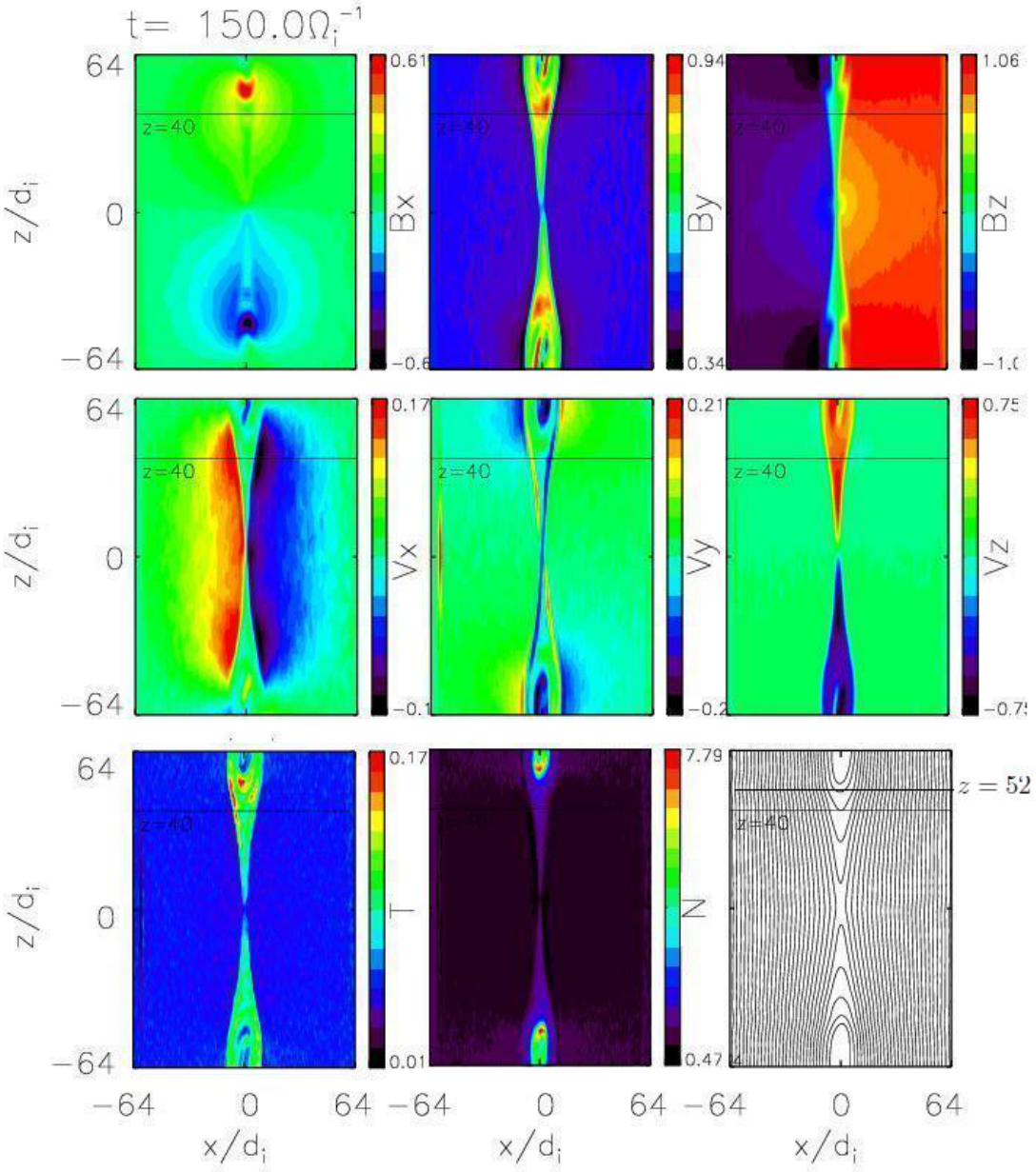


Figure 4.1: The contour plots of $B_x$, $B_y$, $B_z$, $V_x$, $V_y$, $V_z$, $T$, $N$, and configuration of magnetic field lines. The solid line corresponds to the position at $z = 40d_i$, along which there appears a quasi-steady structure. The solid line at $z = 40d_i$ indicates the boundary of the leading bugle. The solid line $z = 40d_i$ shows the transit boundary between the plasma bugle and the steady state layer.

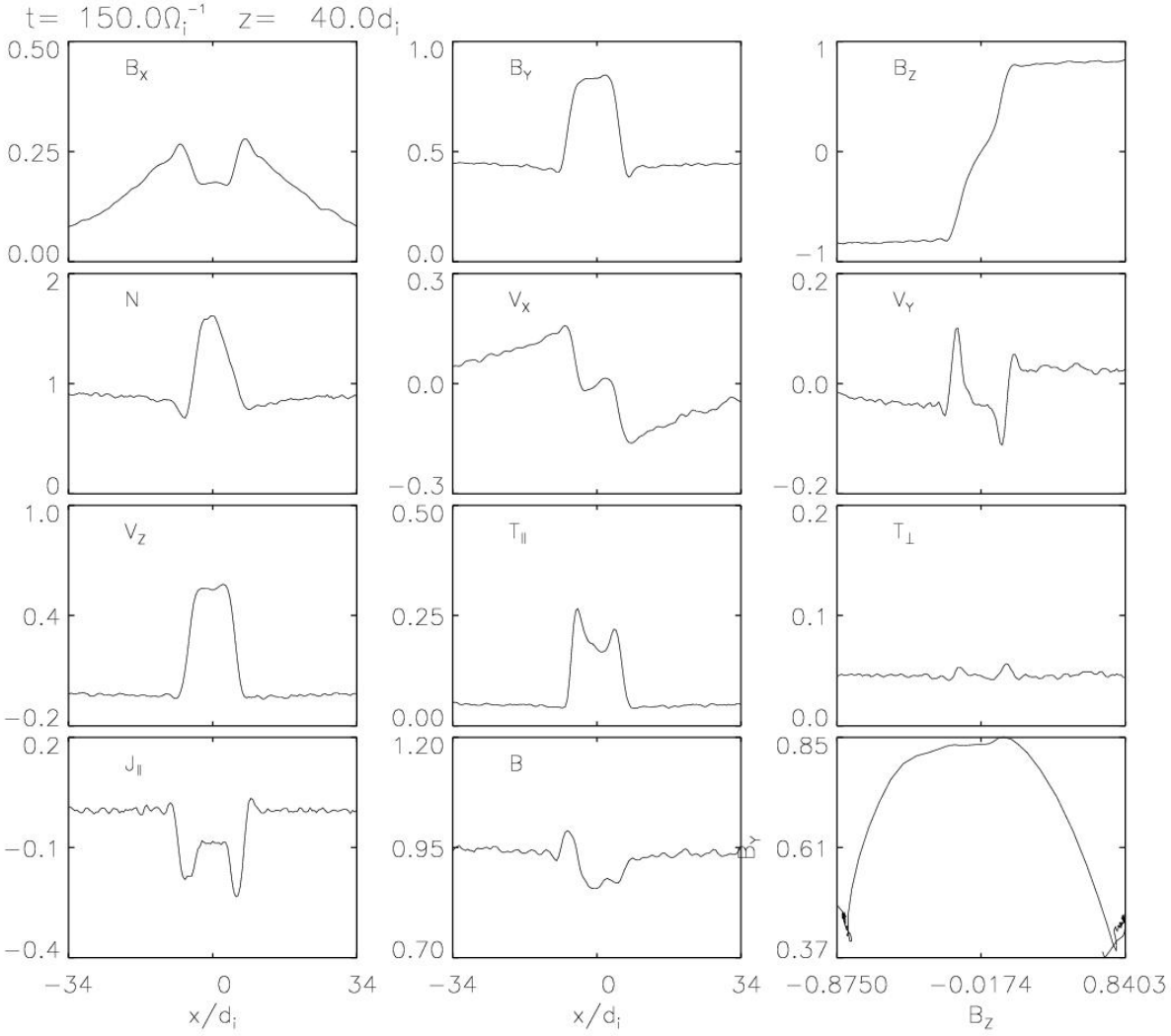


Figure 4.2: The spatial profiles of $B_x$, $B_y$, $B_z$, $N$, $V_x$, $V_y$, $V_z$, $T_\parallel$, $T_\perp$, $J_\parallel$, and $B$ at $z = 40d_i$ and hodograms of the tangential magnetic field ($B_z$-$B_y$).

Fig.4.2 depicts the spatial profiles of the magnetic field $B_x$, $B_y$, $B_z$, density $N$, the ion flow velocity $V_x$, $V_y$, $V_z$, the parallel temperature $T_\parallel$, the perpendicular temperature $T_\perp$, the parallel current density $J_\parallel$, and the magnitude of magnetic field $B$ at $z = 40d_i$, and the hodograms of the tangential magnetic field ($B_z$-$B_y$). Note that $z = 40d_i$ is located in the steady reconnection layer as indicated in Fig.4.1. We can see that two discontinuities bound the steady reconnection layer with the wave front at $x = \pm 8.5d_i$ and the width of $\sim 2.3d_i$. Across the discontinuities, the plasma is accelerated so that $V_z$ is changed from $\sim 0$ in the upstream to $\sim 0.75V_{A0}$ in the downstream corresponding to the change of the Alfvén speed $\sim 0.7V_{A0}$. The hodogram shows that the tangential field rotates by an angle of around $\sim \pi/2$ through each discontinuity. These pair of discontinuities are roughly rotational discontinuities. Notice that the magnetic field strength slightly decreases and the ion density increases across the rotational discontinuity. The changes in the magnetic field and ion density at the rotational discontinuity are due to the increase of the parallel temperature $T_\parallel > T_\perp$ because of the streaming ions along the magnetic field lines. The slow shock, however, is too weak to be identified in the simulation because of $T_\parallel > T_\perp$. All results shown here are consistent with the previous 2D simulations.

To study the 3D effect, we examine the variations along the y direction. The variation of a certain quantity $f$ is calculated as $f(x, y, z) - \bar{f}(x, z)$, where $\bar{f}(x, z)$ is the average along the y direction at fixed positions (x,z). The top two figures in Fig.4.3 present the contour plots of variations of $B_x$ and $N$ along the y direction in the x-z plane at $y = 0$, and the bottom two figures present the contour plots of the corresponding variations in the y-z plane at $x = 4d_i$ as indicated by the solid line in the top figures. At time $t = 150\Omega_i^{-1}$, one can see that the variations are significant in the transition region between the leading bulge and the quasi-steady structure. In the y-z plane at $x = 4d_i$ the structure of the variation of $B_x$ stretches out along the initial local magnetic direction $\mathbf{b}$. Since the x direction is perpendicular to the initial

magnetic field, the variation of $B_x$ represents the shear waves, while the variation of $N$ represents the compressible waves.

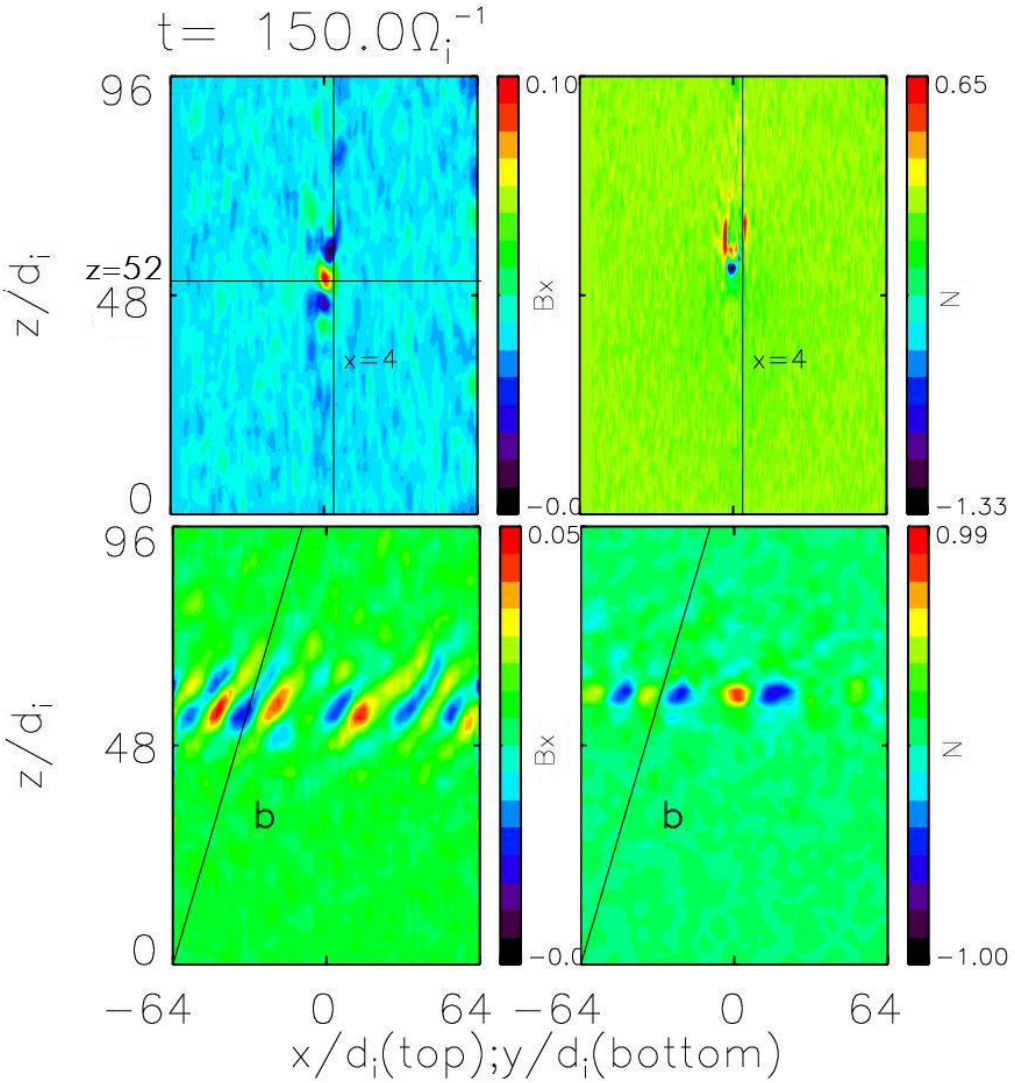


Figure 4.3: Top figures: the contours of variations of $B_x$ and $N$ along the y direction in the x-z plane at $y = 0$; bottom figures: the contours of variations of $B_x$ and $N$ along the y direction in the y-z plane at $x = 4d_i$. The solid line along $z = 52d_i$ in the top left figure indicates the boundary of the leading bugle. The solid lines in the top figures indicate the y-z plane at $x = 4d_i$; the solid lines in the bottom figures show the local initial magnetic field direction.

Fig.4.4 shows the contours of variations along the y direction of $B_x$, $B_y$, $B_z$, $N$, $V_x$, $V_y$, $V_z$, $E_x$, $E_y$, $E_y$, $J_\parallel$, $E_\parallel$ in the y-z plane at $x = 3d_i$ when $t = 150\Omega_i^{-1}$. In these

structures, the shear components $B_x$ and $V_x$, $E_y$, and the parallel current density $J_\parallel$ are well correlated. In Fig.4.3, one may have noticed that the spatial scale of the variation of $B_x$ is $\sim 3d_i$ or $\sim 10\rho_i$, considering to $\beta_i = 0.1$. Since $k_x\rho_i \sim \frac{2\pi}{10\rho_i}\rho_i \approx 0.62$, certain kinetic effect are expected, which is justified by the strong correlation between the parallel electric field $E_\parallel$ and $B_x$.

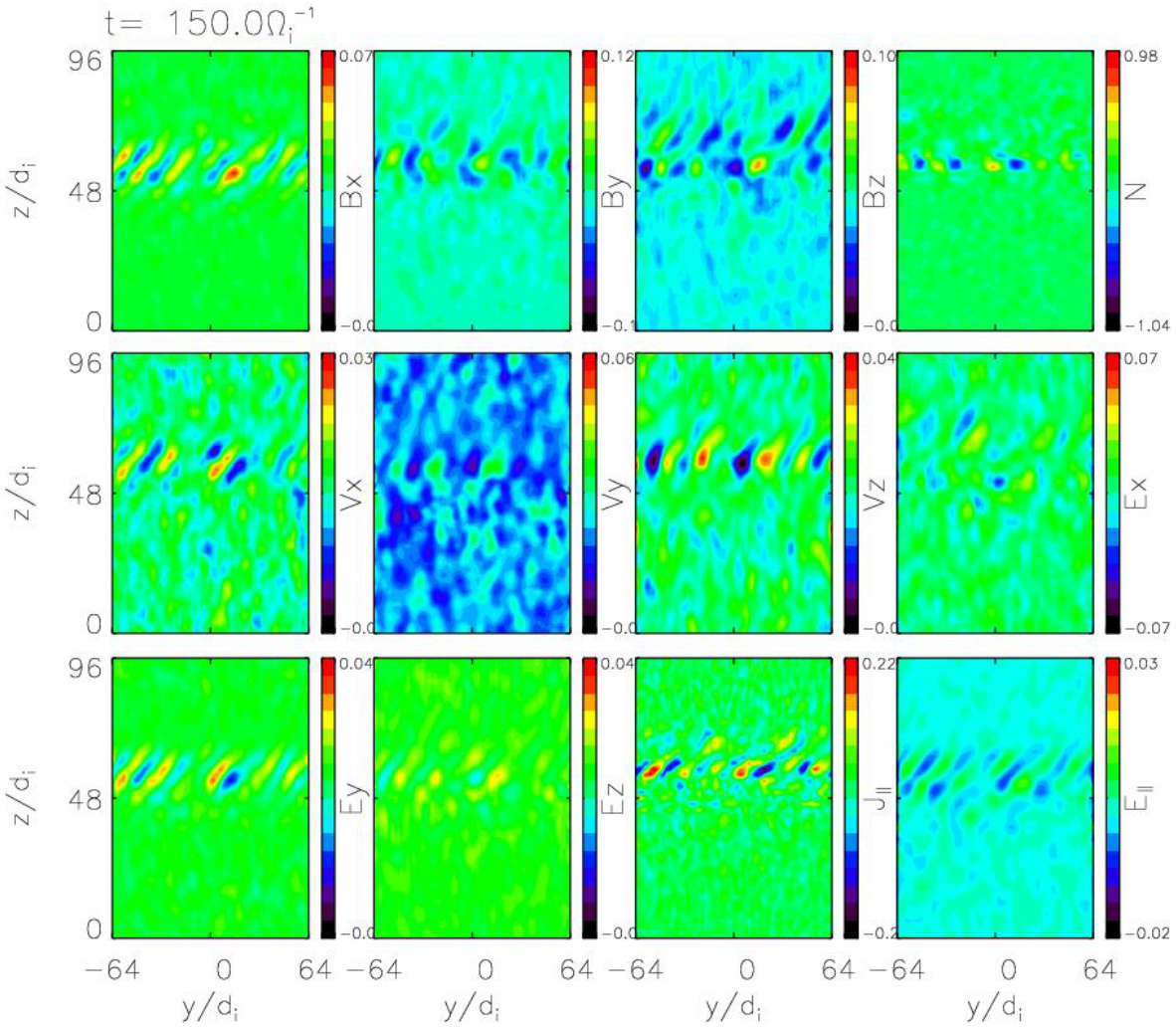


Figure 4.4: The contours of variations along the y direction of $B_x$, $B_y$, $B_z$, $N$, $V_x$, $V_y$, $V_z$, $E_x$, $E_y$, $E_y$, $J_\parallel$, $E_\parallel$ in the y-z plane at $x = 3d_i$ when $t = 150\Omega_i^{-1}$.

### 4.3.2 Case with a Finite X-line: $2\eta_0 = 8d_i$

In reality, the length of X-line cannot be infinite. Shay et al. [2010] have shown that 3D structures develop in a spontaneous reconnection, corresponding to spatially isolated sites of reconnection with scale lengths around $10d_i$. In the following, we show a case in which the length of the X-line is set as $2\eta_0 = 8d_i$ to study the finite length X-line effect.

The top two figures in Fig.4.5 show the configurations of magnetic field lines near the current sheet at $t = 50\Omega_i^{-1}$ (left) and $t = 80\Omega_i^{-1}$ (right). At $t = 50\Omega_i^{-1}$, some magnetic field lines have been reconnected. Since the length of the X-line is finite, the process of reconnection is limited in a finite region. At $t = 80\Omega_i^{-1}$, the reconnected field lines are dragged towards $\pm z$ directions by the accelerated plasmas and are twisted at the same time. It is due to that the large-amplitude perturbations generated by the reconnection and their consequent propagations change the local topology of magnetic field lines. The contour plots of $B_x$ (left) and $V_x$ (right) in the x-z plane at $y = 25d_i$ of $t = 80\Omega_i^{-1}$ are presented in the bottom two plots. We can see that the shear perturbations of $B_x$ and $V_x$ are evident in the plane far from the reconnection region, and they are well correlated. The perturbation regions are associated with the reconnected field lines, while the field lines outside of the perturbations stay unreconnected. It indicates that the perturbations caused by the reconnection propagate into the sites far from the diffusion region along the magnetic field lines. We also notice that the perturbations in the x-z plane of $y = 25d_i$ are just located at one side of the current sheet. Crossing the current sheet along the red line indicated in the top left plot, we observe that the field lines are connected on the side of current sheet and unconnected on the other side. Such asymmetry is simply due to the field line geometry geometry of this "component reconnection", i.e., the reconnection with a finite guide field.

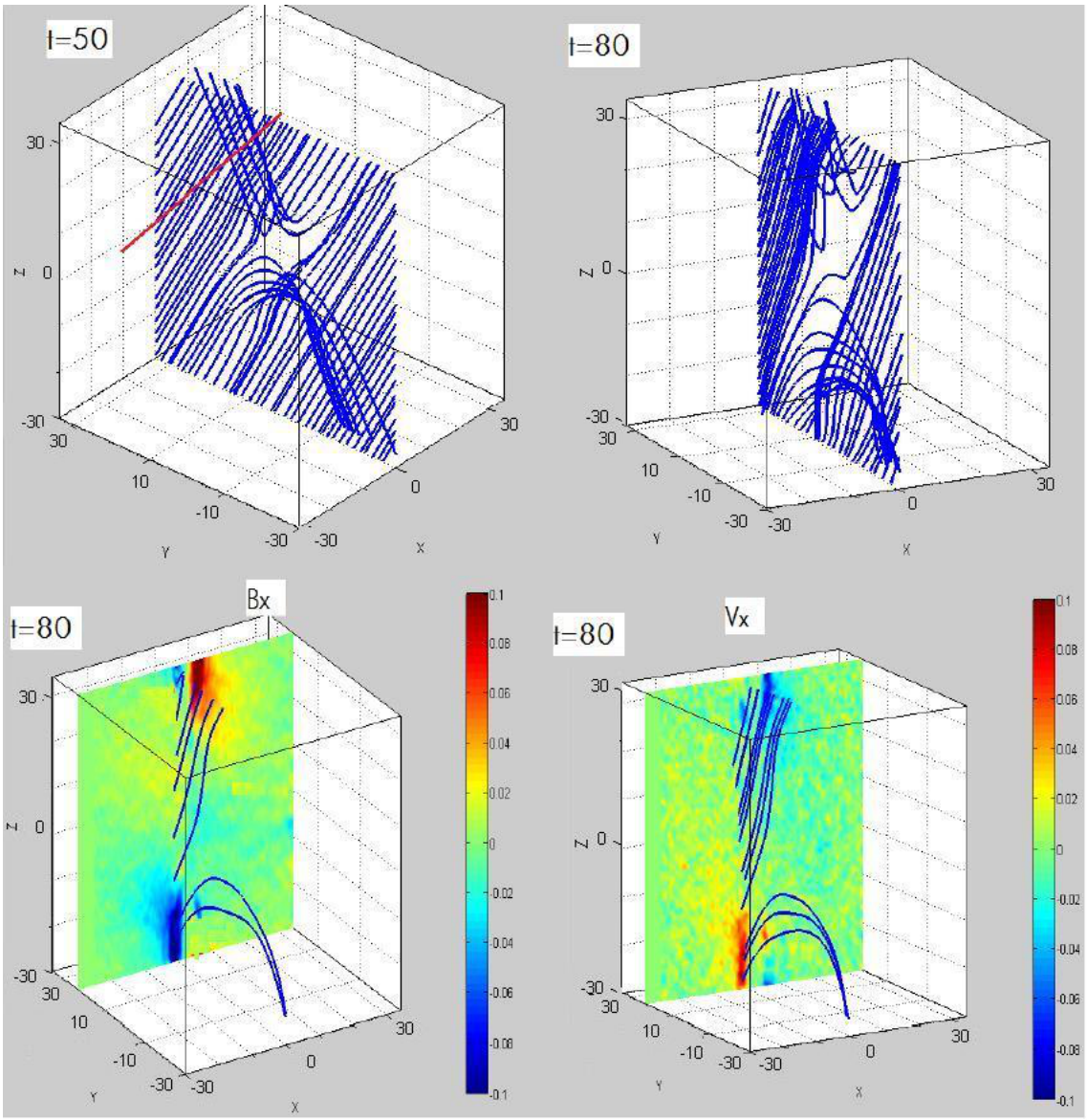


Figure 4.5: The configuration of magnetic field lines near the current sheet at $t = 50\Omega_i^{-1}$ (the top left) and $t = 50\Omega_i^{-1}$ (the top right), and the contour plots of $B_x$ (the bottom left) and $V_x$ (the bottom right) in the xz plane of $y = 25d_i$ at $t = 50\Omega_i$.

To investigate the properties of propagating waves, we now examine the propagation speed of the wave front. Fig.4.6 shows the relationship between the time $t$ and the distance $L$ from the center of the diffusion region (0,0,0) to the position of the wave front. Obviously $t$ and $L$ are linearly correlated with a linear fit of $L = 0.89t - 11.99$. Therefore the propagation speed is $0.89V_{A0}$ that is close to the lobe Alfvén speed $V_{A0}$. Note that the propagation is mainly located outside the edge of the current sheet, where the Alfvén speed is slight smaller than the lobe Alfvén speed.

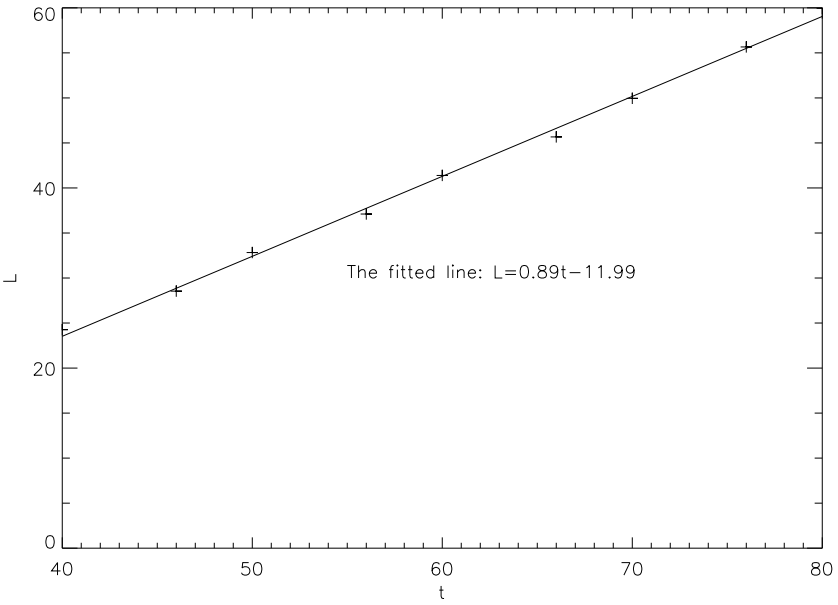


Figure 4.6: The relationship between time $t$ and the distance $L$ from the center of the diffusion region (0,0,0) to the position of wave front.

In Fig.4.7, the contour plots of $B_x$ and $N$ in the x-z plane of $y = 16d_i$ at $t = 80\Omega_i$ are presented. The contours of $B_x$ exhibit clear structure of perturbations, while the density perturbations are also observed at the same position. Since the perturbations propagate from the diffusion region that has the characteristic scale length $\sim \rho_i$, it makes sense that the spacial scale length of the perturbation $B_x$ is $\sim 3d_i$, corresponding to $k_x\rho_i \approx 0.62$. We expect the waves to have certain kinetic effects.

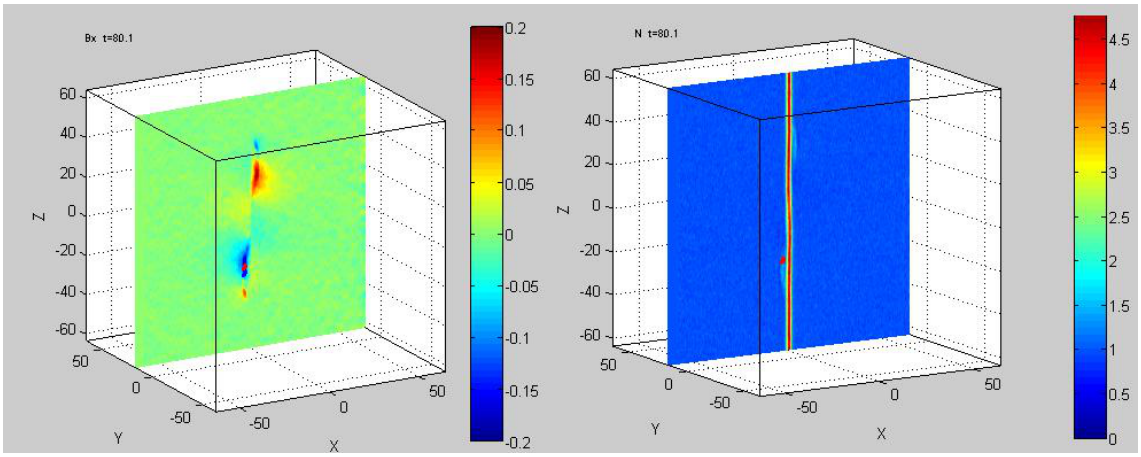


Figure 4.7: The contour plots of $B_x$ and density $N$ in the x-z plane of $y = 16d_i$ at $t = 80\Omega_i$. The red dot stands for the position (4, 16, -20).

Fig.4.8 shows the time evolutions of $B_x$, $B_y$, $B_z$, $N$, $V_x$, $V_y$, $V_z$, $E_x$, $E_y$, $E_z$, $E_\parallel$, $B$, $E_{x\times\mathbf{b}}$, $B_\parallel$, and the hodogram of $B_x - B_{x\times\mathbf{b}}$ at the position $(x, y, z) = (4, 16, -20)$, as indicated by the red dot in Fig.4.7. Among them, $B_\parallel$ is calculated by $\mathbf{B}\cdot\mathbf{b}$, where $\mathbf{b}$ is the initial magnetic field direction, and the subscript $x\times\mathbf{b}$ stands for the direction perpendicular to $\mathbf{x}$ and $\mathbf{b}$. We see that the transverse components $B_x$, $V_x$, and $E_y$, $E_z$ are well correlated. The ratio $E_{x\times\mathbf{b}}/B_x$ is $\sim 0.8V_{A0}$ close to the lobe Alfvén speed. During the whole time, the magnitude of the magnetic field $B$ stays almost constant, as well as the parallel component of the magnetic field $B_\parallel$. The wave appears an Alfvén mode. Moreover, the spatial scale length of perturbations along the x direction is comparable to $\rho_i$, and $E_\parallel$ is correlated with the perturbation of the local density that develops after the arrival of these perturbations. The slight increase of density is also due to the ion kinetic effect. Recall that due to the ion kinetic effect, the Alfvén wave becomes compressible and generates an electric field parallel to the local magnetic field. Since $\mathbf{b}$ points into the paper in the hodogram of $B_x - B_{x\times\mathbf{b}}$, the waves rotate along the counterclockwise direction and have a lefthand polarization.

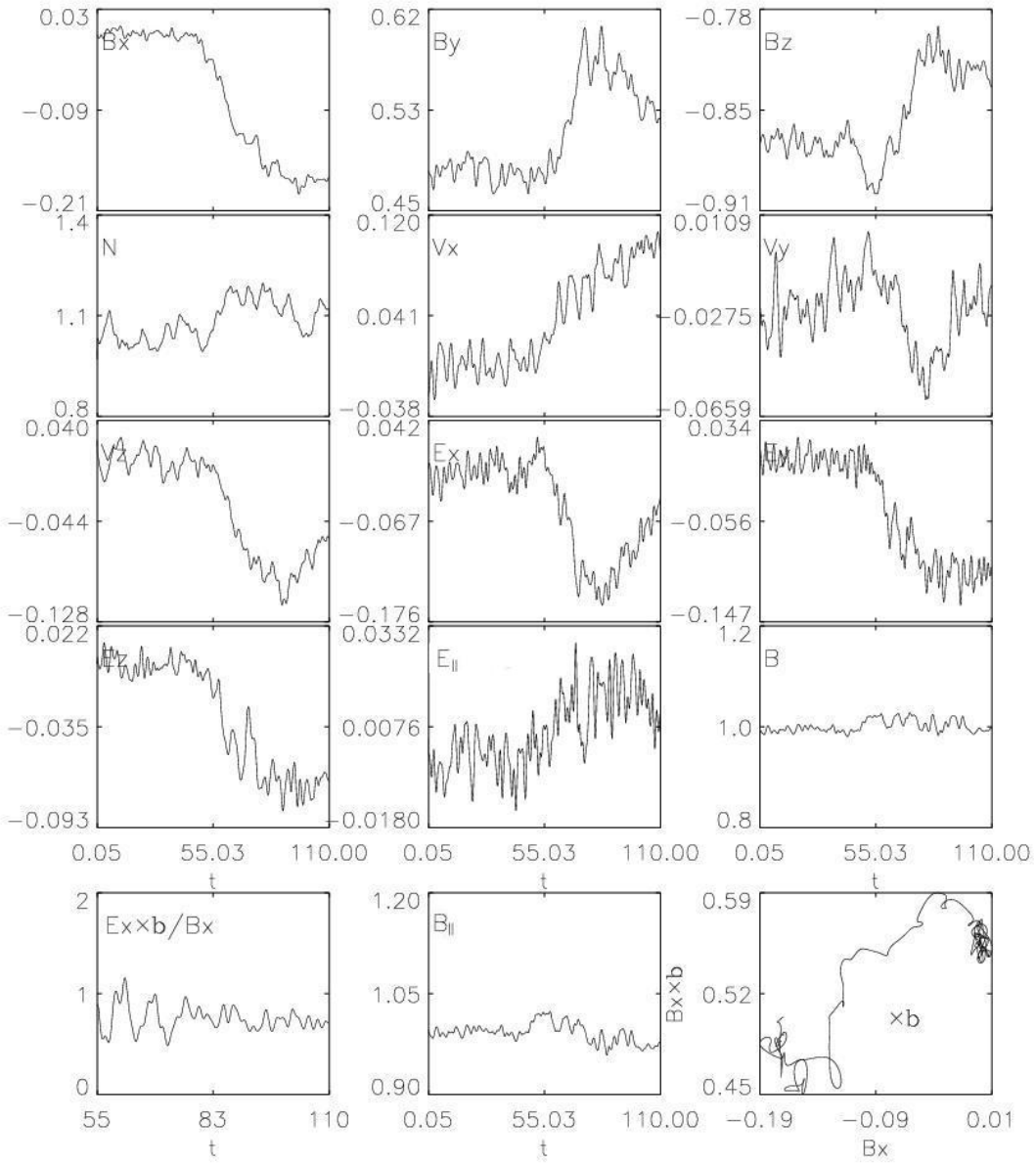


Figure 4.8: The time evolution of $B_x$, $B_y$, $B_z$, $N$, $V_x$, $V_y$, $V_z$, $E_x$, $E_y$, $E_z$, $E_\parallel$, $B$, $E_{x\times\mathbf{b}}$, $B_\parallel$, and the hodogram of $B_x - B_{x\times\mathbf{b}}$ at the position (4, 16, -20) as indicated by the red dot in Fig.4.7.

The contour plots of $V_z$ at $x = 0$ (left) and $x = 2d_i$ (right) are shown in Fig.4.9. In the center of the current sheet, the plasma is accelerated by the tension fore caused the reconnected field lines, and the accelerated plasma is mainly towards $\pm z$ directions. Outside the current sheet, the Alfvén wave propagates along the field lines, and the plasma is accelerated through the wave during its propagation. Therefore the accelerated plasma is mainly along the field lines as shown in Fig.4.8.

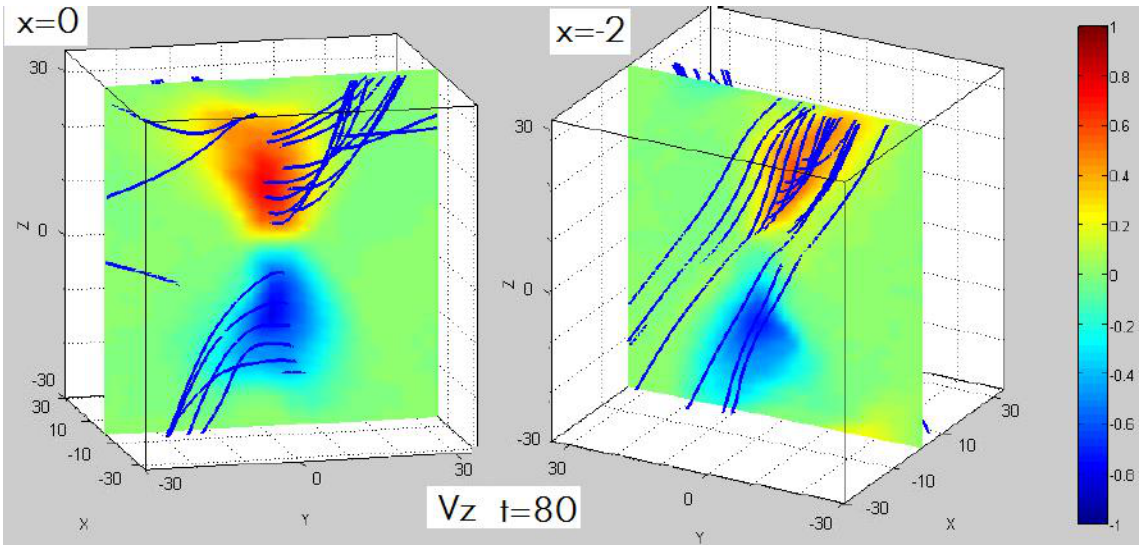


Figure 4.9: The contour plots of $V_z$ at $x = 0$ (left) and $x = 2d_i$ (right) at $t = 80\Omega_i^{-1}$.

Fig.4.10 shows the contour plots of $B_x$, $B_y$, $B_z$, $V_x$, $V_y$, $V_z$, $N$, $T_\parallel$ and $T_\perp$ in the x-z plane of $y = 0$. Note the x-z plane of $y = 0d_i$ is in the center of X-line. We can see that the resulting structures here are very different from the 3D run with an infinitely long X-line. No clear leading bulge exists during the reconnection, although an accelerated plasma layer is formed near the center of current sheet where the parallel heating is observed. Moreover, we do not find the discontinuity fronts on the edges of the reconnection layer, as in 2D simulations and 3D simulations for cases with an infinite X-line. In 3D simulation with the limited X-line, the component $B_x$ is a shear perturbation to the local magnetic field. In such case with $k_y \neq 0$, such

3D perturbations propagate with a group velocity along the field lines. Therefore, no steady discontinuities or shocks are formed.

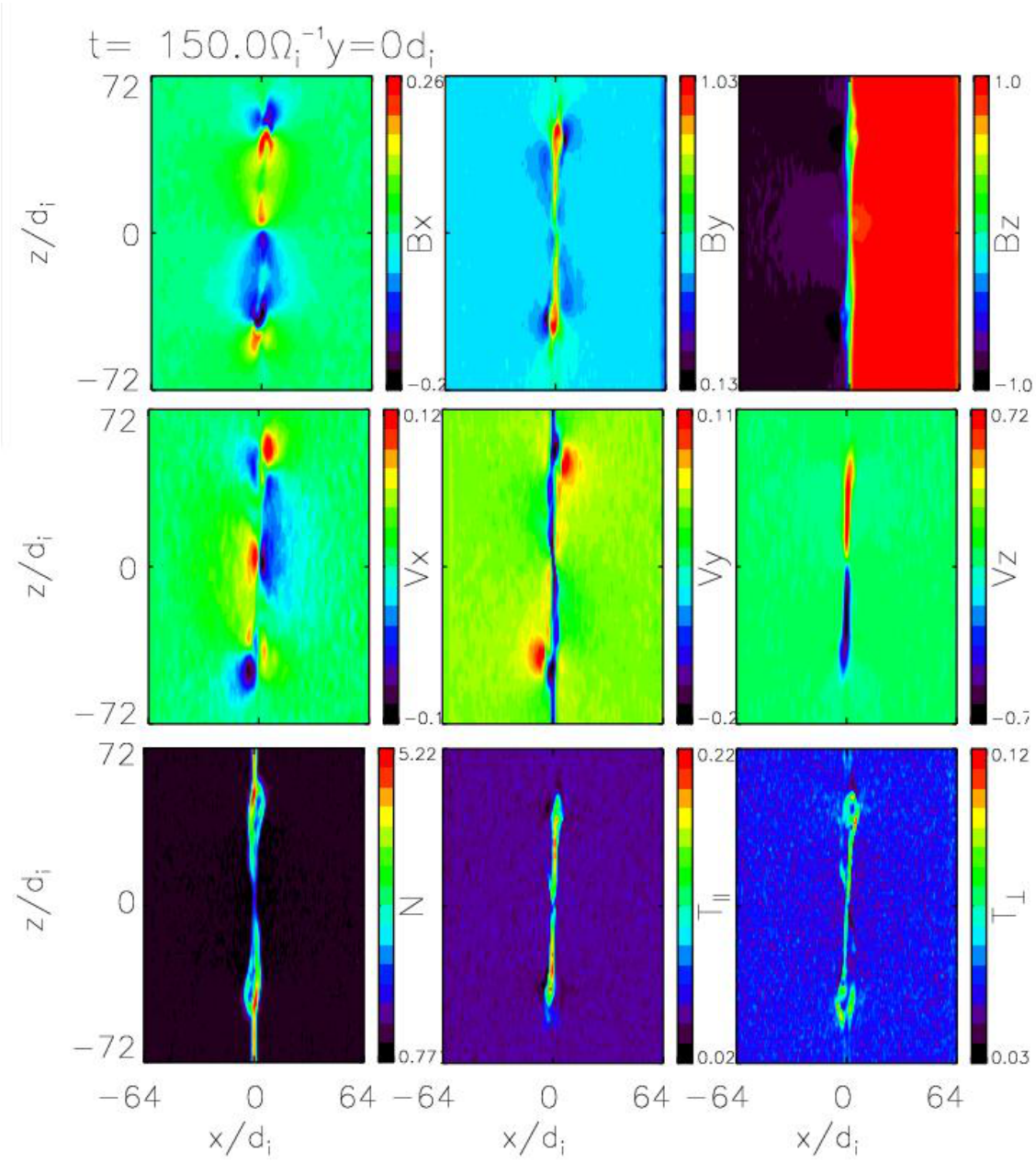


Figure 4.10: The contour plots of $B_x$, $B_y$, $B_z$, $V_x$, $V_y$, $V_z$, $N$, $T_\parallel$ and $T_\perp$ in the x-z plane of $y = 0$ when $t = 150\Omega_i^{-1}$.

Fig.4.11 shows the contour plots of $B_x$, $B_y$, $B_z$, $V_x$, $V_y$, $V_z$, $N$, $T_\parallel$ and $T_\perp$ in the x-z plane of $y = 20d_i$. The propagations of perturbations generated by the reconnection

accelerate the local plasma and form a structure similar to that in the x-z plane of $y = 0d_i$, although no reconnection actually occurs in this x-z plane. Across the current sheet, the layers are asymmetric due to the reason discussed already. Again, the parallel heating occurs in the layers. The enhancement of density is found in the layers because of the acceleration of the plasma.

Cases with various lengths of X-line are also simulated. It is found that the critical X-line length for the existence of steady-discontinuities is $\sim 30d_i$.

## 4.4 Summary

We have used the 3D hybrid simulation model to study the generation of low frequency waves by the reconnection under a finite guide field. The simulation results are summarized below.

For the case with an infinite X-line:

1. 3D simulation results are similar to those of 2D cases. Two quasi-steady rotational discontinuities are formed behind a plasma bulge. The plasmas are accelerated across the rotational discontinuities.

2. The contour plots show that there are perturbation structures in the transition region between the leading bulge and the steady discontinuities. The transverse perturbations lead to the presence of short-wavelength field-aligned structures, in which $E_\parallel \neq 0$ due to the ion kinetic effects.

For the cases with a finite X-line:

3. It is found that the perturbations caused by the reconnection propagate along the local magnetic field lines.

4. The wavefront of perturbations propagates with the local Alfvén speed. The shear components dominate the wavefront of perturbation which are seen as locations far from the reconnection region, and the ratio between the corresponding transverse electric field and magnetic field components is almost equal to the local Alfvén speed.

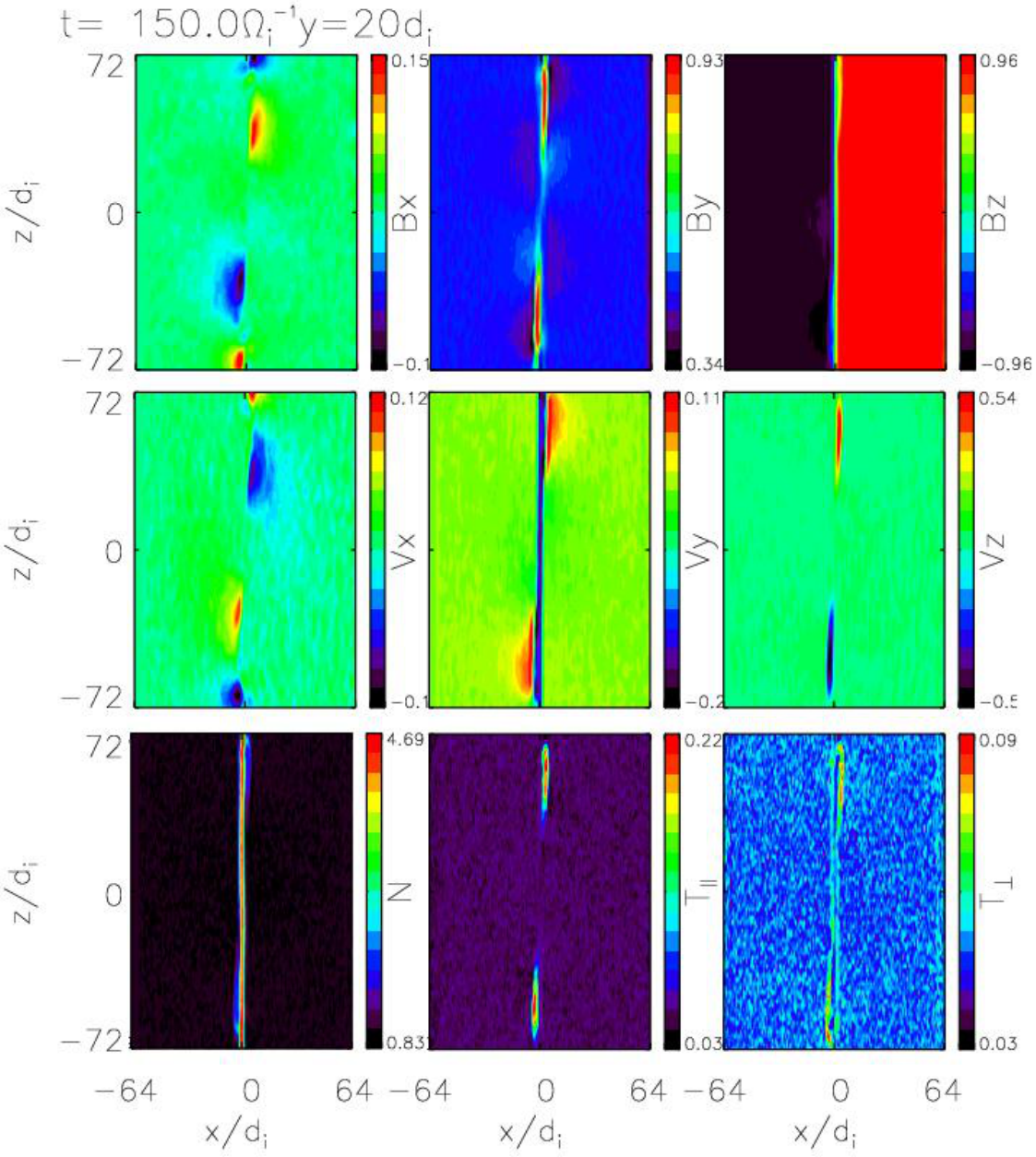


Figure 4.11: The contour plots of $B_x$, $B_y$, $B_z$, $V_x$, $V_y$, $V_z$, $N$, $T_{\parallel}$ and $T_{\perp}$ in the x-z plane of $y = 20d_i$ when $t = 150\Omega_i^{-1}$

These waves are identified as kinetic Alfvén waves, in which the wave number $k_x\rho_i \sim 1$. Our simulation indicates that the finite X-line length leads to a structure of the reconnection layer that is very different from the cases with an infinite X-line, in which steady discontinuity fronts are dominant.

5. Parallel electric field $E_\parallel$ is generated in the kinetic Alfvén waves, and the structure of $E_\parallel$ has a strong correlation with the structures of the shear components.

6. The critical length of X-line that leads to the Petschek-type steady shocks or discontinuities is found to be $\sim 30di$. Our study indicates that a finite extent of X-line alters the wave structure of the reconnection layer.

The generation of kinetic Alfvén waves in the general cases of reconnection may provide an important mechanism for the particle heating and acceleration as these waves propagate along field lines to the ionosphere.

# Chapter 5

## Summary

Magnetic field reconnection provides an efficient mechanism for the transfer of magnetic energy to plasma heat and kinetic energy. The kinetic physics of the fast reconnection in collisionless plasmas, however, is still poorly understood due to the complex plasma dynamics that is largely caused by the disparate spatial and temporal scales between the electron and ions. The 2D Petschek reconnection model is the first fast reconnection model, which provides a mechanism of reconnection that is fast enough to explain the phenomena caused by the reconnection. In order to fully understand the validity of the Petschek model, two basic questions should be answered. One is how the fast reconnection is triggered by micro instabilities, and the other is how the reconnection layer will be modified or altered in the general 3D geometries in reality.

To tackle the problem due to the vast difference between the electron and ion scales and investigate the physics of reconnection from the micro to macro scales, we use the newly developed GeFi particle scheme to simulate the reconnection in a 2D current sheet with a finite guide field and a realistic mass ratio. In this thesis, the GeFi model of Lin et al. [2005] has been improved for the nonuniform current sheets.

Tearing mode instabilities are believed to play a fundamental role to trigger the fast reconnection. As a first step to apply the GeFi model to the reconnection research, we have developed a linear eigenmode theory of the tearing instability to benchmark the improved GeFi scheme. The GeFi results have also been compared with the asymptotic matching theory of Drake and Lee [1977a]. Furthermore, the kinetic effects that are missing in previous theoretical studies of the tearing mode

have been examined through the GeFi simulations. After the code benchmark, we have then carried out linear and nonlinear GeFi simulations of the tearing instability in magnetic reconnection.

While the application of the GeFi model to magnetic reconnection has produced interesting initial results, the complete investigation of 3D nonlinear magnetic reconnection using the GeFi model is still beyond the capability of the current GeFi scheme. To explore the properties of low-frequency waves generated by magnetic reconnection, a hybrid code has been used to simulate the 3D structure of reconnection layer under a finite guide field.

The main results of this thesis are summarized:

The improved GeFi model:

1. Our GeFi particle simulation model, in which the electrons are treated as gyrokinetic particles and ions are treated as fully kinetic particles, has been improved and modified to allow the the existence of modes with wavelengths on the same scale of the background nonuniformity.

2. The linearized GeFi scheme is benchmarked for uniform plasmas, and the simulation results using the $\delta f$ method show that the model can accurately resolve the physics ranging from Alfvén waves to lower-hybrid/whister waves, for $k_{\|} << k_{\perp}$ and $\omega << \Omega_e$.

The tearing mode instability under a finite guide field:

1. The GeFi simulation model is benchmarked with tearing mode instabilities in a simple current sheet and the Harris current sheet. Our results agree with the eigenmode analysis and the previous studies under simplified conditions of these theoretical models. The inhomogeneity terms affect the structure of tearing modes, and cannot be neglected when $B_y \sim B_x$.

2. In the general cases in which the ion gyroradius is comparable to the current sheet width, the ion kinetic effects are found to play a significant role on the growth

rate of tearing modes. In such cases, the Drake and Lee theory [1977a] and the eignemode analysis based on the drift kinetic assumption are invalid.

3. The nonlinear GeFi simulation shows that the ion effect can broaden the width of saturated magnetic islands from the electron dynamic spatial scale to the ion gyroradius. The case with multiple tearing modes shows that the coalescence of magnetic islands can form a larger saturation island than the case of a single tearing mode.

The generation of low frequency waves by reconnection under a finite guide field:

1. For the case with a infinitely long X-line, 3D simulation results are similar to those of 2D cases. In addition to the steady rotational discontinuities in the outflow region, wave perturbations are also found between between the leading plasma bulge and the steady discontinuities. The transverse perturbations lead to the presence of short-wavelength field-aligned structures, in which $E_{\parallel} \neq 0$ due to the ion kinetic effects.

2. For the case with a finite extent of X-line, it is found that the perturbations caused by the reconnection propagate along the local magnetic field lines. The wavefront of perturbations propagates with the local Alfvén speed. The shear components dominate the wavefront of perturbation which are seen at locations far from the reconnection region. These waves are identified as kinetic Alfvén waves, in which the wave number $k_{\perp}\rho_i \sim 1$. Parallel electric field $E_{\parallel}$ is generated in the kinetic Alfvén waves. Our simulation indicates that the finite X-line length leads to a structure of the reconnection layer that is very different from the cases with an infinite X-line as as in the Petschek model, in which steady discontinuity fronts are dominant.

Bibliography


[1] Biernat, H.K., Heyn, M.F., Semenov, V.S., Farrugia, C.J., The structure of reconnection layers: Application to the Earths Magnetopause, *J.Geophys.Res., 94*, 287, 1989

[2] Birn, J., et al., Geospace Environmental Modeling(GEM) magnetic reconnection challenge, *J.Geophys.Res., 106*, 3715, 2001

[3] Birn, J., E. R. Priest, Reconnection of Magnetic Fields: Magnetohydrodynamics and Collisionless Theory and Observations, Cambridge, NewYork, 2007

[4] Biskamp, D., Magnetic reconnection via current sheets, *Phys.Fluids, 29*, 1520, 1986

[5] Burden, R.L., Faires, J.D., *Numerical Analysis* , Brooks/Cole, 2005

[6] Chen, Y., Parker, S.E., A $\delta f$ particle method for gyrokinetic simulations with kinetic electrons and electromagnetic perturbations, *J.Comput.Phys, 189*, 463, 2003

[7] Drake, J.F. Lee, Y.C., Kinetic theory of tearing mode instabilities, *Phys.Fluids, 20*, 1341, 1977a

[8] Drake, J.F. Lee, Y.C., Nonlinear evolution of collisionless and semicllisional tearing modes, *Phys.Rev.Lett. 39*, 453, 1977b

[9] Daughton, W., Electromagnetic properties of the lower-hybrid drift instability in a thin current sheet, *Phys. Plasmas 10*, 3103, 2003

[10] Daughton, W., Karimabadi, H., Kinetic theurgy of collisionless tearing at the magnetopause, *J.Geophys.Res., 109*, A0317, 2005

[11] Fireman, E.A., Chen., L., Nonlinear gyrokinetic equations for low-frequency electromagnetic waves in general plasma equilibria, *Phys.Fluids, 25*, 502, 1982

[12] Furth, H.P., Killeen, J., Rosenbluth, M.N., Finite resistivity instabilities of a sheet pinch, *Phys.Fluid, 6*, 459, 1963

[13] Furth, H.P., Rutherford, P.H., Selberg,H., Tearing mode in the cylindrical tokamak, *Phys.Fluid, 16*, 1054, 1973

[14] Heyn, M.F., Biernat, H.K., Semenov, V.S., The structure of magnetic reconnection layer, *J.Geophys.Res., 90*, 1781, 1981

[15] Hans, J.P., Poedts, S. *Principles of Magnetohydrodynamics: With Applications to Laboratory and Astrophysical Plasmas*, Cambridge Press., 2004

[16] Harris, E.G., On a plasma sheath separating regions of one directional magnetic field, *Nuovo Cimento 23*, 115, 1961

[17] Hockney, R.W., Eastwood, J.W., *Computer Simulation Using Particles*, Mcgraw-Hill, New York, 1981

[18] Hoshino, M., The electrostatic effect for the collisionless tearing mode, *J.Geophys.Res., 92*, 7368, 1988

[19] Landau, L.D., Lifshitz, E.M., *Electrodynamics of Continuous Media*, Pergamon Press., 1960

[20] Katanuma, I., Kamimura, T., Simulation studies of the collisionless tearing instabilities *Phys.Fluid, 23*, 2500, 1980

[21] Karimabadi, H., Daughton, W., Quest, B.K., Physics of saturation collisionless tearing mode as a a function of guide field, *J.Geophys.Res., 110*, A010749, 2005

[22] Karimabadi, H., Huba, J., KraussVarban, D., On the generation and structure of the quadrupole magnetic field in the reconnection process, *Geophys.Rev.Lett. 31*, L070806, 2004

[23] KrasussVarban, D., Omidi, N., large-scale hybrid simulations of the magnetotail during reconnection, *Geophys.Res.Lett., 22*, 3271, 1995

[24] Karimabadi, H., Daughton, W., Quest, K.B., Antiparallel versus component merging at the magnetopause: Current bifurcation and intermittent reconnection, *J.Geophys.Res., 10*, A03213, 2005b

[25] Karimabadi, H., Daughton, W., Quest, K.B., Physics of saturation of collisionless tearing mode as a a function of guide field, *J.Geophys.Res., 110*, A03214, 2005c

[26] KrasussVarban, D., Omidi, N., large-scale hybrid simulations of the magnetotail during reconnection, *Geophys.Res.Lett., 22*, 3271, 1995

[27] Lee, W.W., Gyrokinectic approach in particle simulation, *Phys.Fluids, 26*, 556, 1983

[28] Lee, W.W., Gyrokinectic particle simulation model, *J.Comput.Phys., 72*, 243, 1987

[29] Lin, Y., Lee, L.C., Structure of reconnection layers in the magnetosphere, *Space.Sci.Rev., 65*, 59, 1994a

[30] Lin, Y., Lee, L.C., Reconnection layer at the flank mangetopause in the presence of shear flow, *Geophys.Res.Lett., 21*, 59, 1994b

[31] Lin, Y., Wang, X.Y., Chen, L., Lin, Z.H., A gyrokinetic electron and fully kinetic ion plasma simulation model, *Plasma Phys.Control.Fusion, 47*, 657, 2005

[32] Lin, Y., Wang, X.Y., Three-dimensional global hybrid simulation of dayside dynamics associated with the quasi-parallel bow shock, *J.Geophys.Res., 110*, A12216, 2005

[33] Lin, Y., Wang, X.Y., Three-dimensional global hybrid simulation of dayside dynamics associated with the quasi-parallel bow shock, *J.Geophys.Res., 115*, A04208, 2010

[34] Lin, Y., Lee, L.C., Chaos and ion heating in a slow shock, *Geophys.Res.Lett, 18*, 1615, 1991

[35] Lin, Y., Lee, L.C., Kennel, C.F., The role of intermediate shocks in magnetic reconnection, *Geophys.Res.Lett, 19*, 229, 1992

[36] Lin, Y., Lee, L.C., Simulation study of the Riemann problem associated with magnetotail reconnection, *J.Geophys.Res., 100*, 19,277, 1995

[37] Lin, Y., Swift, D.W., A two dimensional hybird simulation of the magnetotaill reconnection, *J.Geophys.Res., 101*, 19,859, 1996

[38] , Lin, Y., Wang, X.Y., Chen, L., Lu, X., and Kong, W., An improved gyrokinetic electron and fully kinetic ion particle simulation scheme: benchmark with a linear tearing mode, *Plasma Phys. Control. Fusion., 53*, 054013, 2011

[39] Lottermoser, R.F., Scholar, M., Undriven magnetic reconnection in magnetohydrodynamics and Hall magnetohydrodynamics, *J.Geophys.Res., 102*, A3, 4875, 1997

[40] Lottermoser, R.F., Scholar, M., Matthews, A.P.,Ion kinetic effects in magnetic reconnection, *J.Geophys.Res., 103*, 4547, 1998

[41] Masaaki, Y., Kulsrud, R., Ji, H.T., Magnetic Reconnection, *Rivews of Modern Physics, 82*, 603, 2010.

[42] Mandt, M.E., Denton, R.E., and Drake, J.F., Transition to whistler mediated magnetic reconnection, *Geophys.Res.Lett, 21*, 73, 1994

[43] Parker, E.N., Sweet's mechanism for merging magnetic field in conducting fluids, *J.Geophys.Res., 62*, 509, 1957

[44] Parker, S.E., Lee, W.W., A fully nonlinear characteristic method for gyrokinetic simulation, *Phys.Fluids B, 5*, 77, 1993

[45] Petschek, H.E., Magnetic field annihilation, in *AAS-NASA Symposium on the Physics of Solar Flares, NASA Spec. Publ., SP-50*, 425, 1964

[46] Priest, E., Forbes, T., *Magnetic Reconnection: MHD Theory And Applications*, Cambridge Press., 2006

[47] Prtchett, E., Collisionless magnetic reconnection in a three open system, *J.Geophys.Res., 106*, 3783, 2001

[48] Prtchett, E., Onset of saturation of guide-field magnetic reconnection, *Phys.Plasmas, 12*, 062301, 2005

[49] Richter, P., Sholer, M., on the stability of rotational discontinuities, *J.Geophys.Res., 16*, 1257, 1989

[50] Richter, P., Sholer, M., on the stability of rotational discontinuities with large phase angles, *Adv.Space.Res., 11*, 111, 1991

[51] Ricci, P., Brackbill, U. B., Doughton, W., and Lapenta, G., New role of the lower-hybrid drift instability in the magnetic reconnection, *Phys. Plasmas 12*, 5501, 2005

[52] Ricci, P., Brackbill, U. B., Doughton, W., and Lapenta, G., Collisionless magnetic reconnection in the presence of a guide field, *Phys. Plasmas 11*, 4102, 2008

[53] Rogers, B.N., Denton, R.E., Drake, J.F., Shay, M.A., The role of dispersive waves in collisionless magnetic reconnection, *Phys.Rev.Lett., 97*, 195004, 2001

[54] Rutherford, P.H., Frieman, E.A., Drift instabilities in general magnetic field configuration, *Phys.Fluids, 11*, 569, 1968

[55] Rutherford, P.H.,Nonlinear growth of tearing mode, *Phys.Fluids, 16*, 1903, 1973

[56] Sweet, P.A., The neutral point theory of solar flares, in *Electromagnetic Phenomena in Cosmic Physics*, 135, 1958.

[57] Swift, D.W., Lee, L.C., Rotational discontinuities and the structure of the magnetopause, *J.Geophys.Res., 88*, 111, 1983

[58] Swift, D.W., Use of hybrid code to model the Earth's magnetosphere, *Geophys.Res.Lett., 22*, 311, 1995

[59] Sato, T.,Strong plasma acceleration by slow shocks resulting from magnetic reconnection, *J.Geophys.Res., 84*, 7177, 1979

[60] Shi, Y., Lee, L.C., Structure of the reconnection layer at the dayside magnetopause, *Planet.Space.Sci., 38*, 437, 1990

[61] Scholer, M., Undriven magnetic reconnection in an isolated current sheet, *J.Geophys.Res., 94*, 15099, 1989

[62] Sonnerup, B., Magnetic filed reconnection, in *Solar System Plasma Physics, 46*, Elsevier, New York, 1974

[63] Taylor, J.B., Hastie, R.J., Stability of general plasma equilibria-I. Formal theory, *Phys.Fluids, 10*, 479, 1968

[64] Terasawa, T., Hall current effect on tearing mode stability, *Geophys.Res.Lett., 10*, 475, 1983

[65] Ugai, M., Self-consistent development of fast reconnection with anomalous plasma resistivity, *Plasmas.Phys.Control.Fusion, 26*, 1549, 1984

[66] Ugai, M., Shumizu, T., Computer studies on the fast reconnection mechanism in a sheared field geometry, *Phys.Plasmas, 1*, 296, 1993

[67] Wang, X.Y., Lin, Y., Chen, L., Lin, Z.H., A particle simulation of current sheet instabilities under finite guide field, *Phys.Plasmas 15*, 072103, 2008

[68] Wu, C.S., Zhou, Y.M., Tsai, S.T., and Gao, S.C., A kinetic cross field streaming instability, *Phys. Fluids 26*, 1259,1983

[69] Wesson, J.A., Finite resisitivity instability of a sheet pinch, *Nuclear Fusion, 18*, 130,1966

[70] Wan, W., Chen, Y., and Parker, S.E., Gyrokinetic $\delta f$ simulation of the collisionless and semi-collisional tearing mode instability, *Phys.Plasmas 12*, 012311,2005

[71] Yan, M., Lee, L.C., Priest, E.R., Fast magnetic reconnection with small shock angles, *J.Geophys.Res., 97*, 8277, 1992